



**HAL**  
open science

# Numerical and Experimental Approach for Bipolar Plates in PEM Fuel Cells: Novel Designs of Fluid Domain

Nima Abbaspour

► **To cite this version:**

Nima Abbaspour. Numerical and Experimental Approach for Bipolar Plates in PEM Fuel Cells: Novel Designs of Fluid Domain. Other. Université d'Avignon, 2020. English. NNT : 2020AVIG0507 . tel-03142675

**HAL Id: tel-03142675**

**<https://theses.hal.science/tel-03142675>**

Submitted on 16 Feb 2021

**HAL** is a multi-disciplinary open access archive for the deposit and dissemination of scientific research documents, whether they are published or not. The documents may come from teaching and research institutions in France or abroad, or from public or private research centers.

L'archive ouverte pluridisciplinaire **HAL**, est destinée au dépôt et à la diffusion de documents scientifiques de niveau recherche, publiés ou non, émanant des établissements d'enseignement et de recherche français ou étrangers, des laboratoires publics ou privés.



**Approche numérique et expérimentale des écoulements  
au sein des piles à combustible: innovations liées aux  
conditions aux limites**

**Numerical and Experimental Approach for Bipolar Plates  
in PEM Fuel Cells: Novel Designs of Fluid Domain**

A dissertation submitted in partial fulfillment of  
the requirements for the degree of:

DOCTOR OF PHILOSOPHY

by:

**MSc. Nima Abbaspour**

Dr. Habil. Philippe Beltrame	Avignon University, France	Supervisor
Prof. Mohammed El Ganaoui	UL, Nancy, France	Reviewer
Prof. Mohammad J. Kermani	AUT, Tehran, Iran	Reviewer
Prof. Gilles Micolau	Avignon University, France	Examiner
Prof. Marie-Christine Néel	Avignon University, France	Supervisor
Prof. Volker P. Schulz	DHBW, Mannheim, Germany	Supervisor

July 15, 2020

# Résumé

La présente thèse fait partie d'un projet destiné à améliorer l'efficacité et la stabilité des piles à combustible à membrane à échange de protons. Elle présente des expériences et des simulations visant à faire évoluer en ce sens la géométrie de canaux véhiculant des fluides à travers les plaques bipolaires à l'anode et à la cathode. En effet, l'électricité produite dépend en particulier d'écoulements diphasiques couplés avec divers phénomènes physiques et très impactés par les forces interfaciales sur les surfaces solides qui les limitent. Nous avons utilisé des codes industriels ainsi que la méthode des réseaux de Boltzmann pour simuler les systèmes complexes en jeu. Le chapitre 1 rappelle le principe de base des piles à combustible ainsi que le rôle des fluides s'écoulant dans les canaux des plaques bipolaires. En partant de piles standard, nous jetons les bases des modifications étudiées ici. Le chapitre 2 détaille un modèle classique du fonctionnement des piles à combustible en régime stationnaire, supposant des écoulements monophasiques dans les canaux. Une expérience réalisée sur une unique pile de ce type valide la formulation mathématique du modèle ainsi que l'outil numérique (Comsol). La simulation met en évidence l'hétérogénéité des flux dans les différents canaux, alors qu'on connaît l'influence négative de cette hétérogénéité. Cependant le modèle utilisé ne tient pas compte de la possibilité d'avoir de l'eau en phase liquide (et pas uniquement gazeuse) dans les écoulements. Pour y remédier, le chapitre 3 décrit un code LBM fondé sur le modèle du gradient de couleur pour les écoulements diphasiques. Ce code est validé à partir d'une expérience réalisée sur une jonction en T, un dispositif applicable bien au delà du contexte des piles à combustible. Le chapitre 4 reste dans le cadre d'écoulements stationnaires gazeux dans des canaux parallèles, mais cependant différents de ceux de piles standard. Un algorithme uniformise automatiquement les écoulements des différents canaux en modifiant leur géométrie, dans certaines limites cependant. Il fait pour cela varier des paramètres comme le nombre de canaux et leurs largeurs. Les dispositifs répartissant ou collectant le fluide entre les différents canaux à l'entrée ou à la sortie influencent aussi le résultat. Nous proposons des géométries uniformisant les écoulements des divers canaux. Hélas le résultat n'est pas satisfaisant en termes de production électrique. Le chapitre 5 décrit les déplacements dirigés et spontanés de gouttes d'eau sur des structures métalliques pourvues de canaux d'axes parallèles, mais dont la forme rappelle des nageoires: une expérience met en évidence une direction nettement privilégiée pour l'étalement des gouttes. Les simulations tri-dimensionnelles en LBM et par la méthode du volume de fluide corroborent la tendance observée tout en révélant à plus petite échelle des détails qui échappent aux visualisations mises en oeuvre: l'effet des forces capillaires est clairement dominant, et s'exerce dans des régions bien précises du dispositif, alors que dans d'autres régions l'inertie est essentielle aussi. Les simulations d'écoulements diphasiques décrits aux chapitres 3 et 5 représentent les résultats principaux.

# Abstract

This thesis is part of a wider project that aims at improving proton exchange membrane fuel cell (PEMFC) efficiency and stability. Our contribution aims at improving the geometry and structure of channels in anode and cathode bipolar plates (BPP) using experiments and simulations. The operation of a PEMFC involves multiphase flows and multiphysics phenomenon such as reactant concentration and electron exchange between the components. To simulate such a complex system employed industrial codes as well as Lattice Boltzmann Method. Chapter 1 reminds the basic principle of PEM fuel cell and the role of the fluids that flow through BPP channels. We describe a standard version of the latter and the modifications which we consider here. Chapter 2 details a classical model that describes PEM fuel cell operation in steady regime and assumes single phase flows in channels. The underlying equations and their simulation (using COMSOL) are validated by an experiment performed on standard single cell. The simulation evidences channels exhibiting unequal fluid fluxes while the literature points the negative effects of such heterogeneity. Since the used models disregards the possibility of having water in two phases, Chapter 3 describes a LBM color gradient code for two phase flows. We validate it against an experiment performed of a T-junction, a device that has applications beyond fuel cell. Chapter 4, differently, is devoted to steady gas flows in parallel channels that differ from standard fuel cell. An algorithm automatically homogenizes the fluid flow by modifying domain geometry within definite limits. It applies to diverse settings, and manages parallel channels by varying parameters as channel number and widths. However, the distributing channels that span the fluid between channels at BPP inlet and recollect it at outlet also matter. The author thus proposes designs that equalize channel flows. The author creates a new design to study the manufacturing feasibility of BPP. Chapter 5 describes water drop directional spreading on metallic structures decorated with fin shaped channels of parallel axis: experiments reveal almost total spreading only in one direction. Three dimensional LBM and Volume of Fluid simulations retrieve the observed trend and capture smaller scale details suggesting subsets of the fluid domain where capillary forces or inertia dominate. Most significant results are two phase flows simulations. They describe the different regimes of films or drops at the outlet of a T-junction whose other branches are fed with immiscible wetting and non-wetting fluids. Moreover, they describe how water drops spread on a microscopic relief which results into skewed capillary force.

# Acknowledgement

This dissertation is the result of my work as research assistant in DHBW Mannheim institute of mechanical engineering. This research was funded by the Federal Ministry for Economic Affairs and Energy in Germany as a part of ZIM (Zentrales Innovationsprogramm Mittelstand) for a year.

I would like to give thanks to my supervisor Prof. Schulz vice dean of mechanical engineering department in DHBW for supporting my work, acquiring external funding and supporting my participation in conferences and seminars. I would like to give special thanks to my supervisors, Prof. Marie-Christine Néel and Dr. Habil. Philippe Beltrame in University of Avignon for giving the encouragement and sharing insightful suggestions abundant support, knowledge, motivation and persistence which gave me more power and spirit to write this thesis. Besides my supervisor, I would like to thank the rest of my thesis committee: Prof. Kermani, Prof. Ganaoui, for their insightful comments and encouragement, but also for the questions which incited me to widen my research from various perspectives.

I would like to thank all the collaborators in projects in this thesis. Prof. Thorsten Röder, Tobias Baumeister from University of Mannheim and Mr Thomas Starke from 3D Micro-Print GmbH.

Thanks to Prof. Sven Schmitz head of mechatronics department in DHBW Eppelheim. My fellow Alexandra Weber for her support and kindness and everyone who did helped me to perform this work. I want to thank my students who attended my fluid mechanic course, my other classes and the students had their projects with me, all of you helped me to excel my competences.

I am grateful to my parent who supported me by all means (mentally and financially) to accomplish my personal goals in gaining knowledge and experience abroad. I want to thank for the courage given by my sister Nazli and my family specially my cousins Ali, Payam, Afsoon, Pantea, and Amir-reza.

I dedicate this thesis to people who accept and promote diversity and equity in their life or at work.

# Contents

<b>1</b>	<b>Objective of the thesis: fuel cell optimization</b>	<b>3</b>
1.1	Introduction . . . . .	3
1.2	Standard fuel cell and principle . . . . .	4
1.2.1	Classical fuel cell element . . . . .	4
1.2.2	Fuel cell stack . . . . .	4
1.2.3	The roles of the components of a fuel cell . . . . .	5
1.2.3.1	Proton exchange membrane . . . . .	6
1.2.3.2	Electrodes . . . . .	6
1.2.3.3	Gas diffusion layer . . . . .	6
1.2.3.4	Bipolar plate (BPP) . . . . .	7
1.3	The improvements which we want to study . . . . .	9
1.3.1	Integrating GDL into BPP . . . . .	9
1.3.2	Water management . . . . .	10
1.3.3	Power and efficiency . . . . .	11
1.4	Strategic two-phase fluid flows in GDL and BPP . . . . .	11
1.5	Solutions studied in this work . . . . .	12
1.6	Additional constraint: 3D printing manufacturing . . . . .	13
<b>2</b>	<b>Fuel cell physical model and methodology</b>	<b>14</b>
2.1	Introduction . . . . .	14
2.2	The physical model that governs fuel cell operation in steady conditions . . .	15
2.3	A new concept in fuel cell: integrating BPP channels and GDL . . . . .	17

2.3.1	Reference system . . . . .	19
2.3.2	Devices made of new BPP channels that do not need any porous GDL . . . . .	19
2.3.3	Additive manufacturing and channels with integrated GDL . . . . .	19
2.4	Simulation of steady fuel cell operation in the case of reference system . . . . .	20
2.4.1	Boundary conditions . . . . .	21
2.4.2	Reference FC simulation . . . . .	22
2.5	Refining thesis objectives and workplan . . . . .	26
<b>3</b>	<b>Numerical method for two phase flow</b>	<b>27</b>
3.1	Introduction . . . . .	27
3.2	Lattice Boltzmann method for two phase flow . . . . .	28
3.2.1	Basic principle and collision operator . . . . .	28
3.2.2	RK calculation process . . . . .	29
3.3	Implementation and validation in the 2D . . . . .	32
3.3.1	Laplace test . . . . .	32
3.3.2	Static contact angle . . . . .	32
3.3.3	Layered flow for immiscible two-phase flow . . . . .	33
3.4	Application of LBM RK to two phase flow in T-Junction . . . . .	34
3.4.1	T-junction as droplet generation system . . . . .	34
3.4.1.1	Geometry . . . . .	35
3.4.1.2	Contact angle . . . . .	35
3.4.1.3	Flow rate . . . . .	36
3.4.1.4	Viscosity . . . . .	36
3.4.1.5	Surface tension . . . . .	36
3.4.2	Simulation of two-phase flow in T-junction . . . . .	37
3.4.2.1	Model implementation and hardware requirements . . . . .	37
3.4.2.2	T-Junction simulation . . . . .	37
3.4.2.3	Velocity-pressure boundary conditions . . . . .	37
3.4.2.4	Periodic boundary conditions and volume force . . . . .	38

3.4.2.5	Flow conditions . . . . .	38
3.4.2.6	Computational efforts . . . . .	38
3.4.3	Experimental validation of the T-junction . . . . .	39
3.4.4	Droplet formation process . . . . .	40
3.4.5	Mesh properties . . . . .	42
3.4.6	Discussion . . . . .	42
3.5	Chapter 3 summary . . . . .	44
<b>4</b>	<b>From reference system to integrated BPP and GDL</b>	<b>45</b>
4.1	Introduction . . . . .	45
4.2	Anode side flow domain . . . . .	46
4.2.1	Pin typed flow field . . . . .	46
4.2.2	Parallel flow field . . . . .	47
4.3	Parallel flow field optimization . . . . .	50
4.3.1	2D LBM comparison with COMSOL . . . . .	53
4.3.2	2D and 3D comparison with COMSOL . . . . .	54
4.3.3	Three-dimensional flow field . . . . .	55
4.3.4	Parallel flow field CFD simulation . . . . .	56
4.4	Reference system comparison to first prototype . . . . .	59
4.5	Conclusion . . . . .	59
<b>5</b>	<b>Application of passive directional transport in PEMFC</b>	<b>61</b>
5.1	Introduction . . . . .	61
5.2	Problem and method . . . . .	62
5.2.1	Foreword . . . . .	62
5.2.2	Structure geometry . . . . .	63
5.2.3	Material constraints . . . . .	64
5.2.4	Method . . . . .	64
5.3	Experimental study of liquid wicking on fin-shaped patterns . . . . .	65
5.3.1	Substrates manufacturing and physical properties . . . . .	66

5.3.2	Experiment . . . . .	67
5.4	Physical model and Numerical methods . . . . .	68
5.4.1	Physical model and mathematical formulation . . . . .	68
5.4.2	Triple line modeling . . . . .	70
5.4.3	2D and 3D geometry for the Simulation . . . . .	70
5.5	Water wicking simulation . . . . .	71
5.5.1	2D simulation . . . . .	72
5.5.2	3D simulation at 50° contact angle . . . . .	72
5.5.3	Influence of the contact angle and geometry . . . . .	76
5.5.4	Continuous flow . . . . .	78
5.6	Conclusion . . . . .	81
<b>6</b>	<b>Conclusion</b>	<b>82</b>

# List of Figures

1	Increase in carbon dioxide in the world [3]. . . . .	1
2	Temperature rise on earth surface(right)[4]. . . . .	1
1.1	Structure of a fuel cell. . . . .	5
1.2	Fuel cell stack [6]. . . . .	5
1.3	Simplified diagram of the triple phase where the reaction take place [9]. . . . .	6
1.4	Rib and channel positions are shown in the anode side. . . . .	7
1.5	Process of GDL manufacturing. . . . .	7
1.6	Flow field layout configuration: a) single serpentine, b) multiple serpentine with two channels, c) pin typed flow field, d) straight parallel. [12]. . . . .	8
1.7	Biomimetic flow fields from left to right. Fractal design(e), tree-liked design(f,g), lung inspired design [13]. . . . .	9
1.8	Cathode flooding in current density above 0.55 lead to increase in pressure drop and decrease in the cell voltage (cell temperature 51°) [21]. . . . .	10
1.9	Efficiency and power density relation to current density [24]. . . . .	11
1.10	Manufacturing process using micro laser sintering [26]. . . . .	13
2.1	The fuel cells are highly multiscale systems. . . . .	15
2.2	The assembly of the fuel cell. Either the composite plate with milled insertion area or reference plate can be used in the assembly. . . . .	18
2.3	The standard assembly of the fuel cell (left), the reference fuel cell (right). The difference in these assembly is monopolar plate splits into milled composite plate which houses the monopolar plate. Moreover, removing the GDL is possible in new design. . . . .	20
2.4	Dimensions of the milled composite plate (left). Anode side composite plate with milled insertion area made from BMA5 (right). . . . .	21

2.5	Same flow field for anode side monopolar plate, SLM manufactured (left), common standard composite flow field (right). . . . .	21
2.6	Pressure distribution in anode (left) and cathode (right). . . . .	24
2.7	Velocity distribution in anode (left) and cathode (right). . . . .	24
2.8	Anode side, water and hydrogen concentration distribution, voltage of the cell 0.4V. . . . .	24
2.9	Cathode side, water and hydrogen concentration distribution, voltage of the cell 0.4V. . . . .	25
2.10	Current density distribution inside the membrane (left), polarization curve for simulation and experiment (right). . . . .	25
3.1	Change in pressure drop across the droplet surface with bubble radius, in simulation domain of 100x100 lattice unit (lu). . . . .	32
3.2	Force balance between the two fluids and the solid phase. In the LBM, the fluids are indicated as hydrophobic (index b) and hydrophilic (index r). Depending on the model parameters, the LBM can be used to simulate a contact angle between 0° and 180° (right). . . . .	33
3.3	Velocity profile in two phase layered flow. . . . .	34
3.4	Head-on device geometry. . . . .	35
3.5	a) Standard geometry of the T-junction, b) modified geometry for periodic boundary conditions. . . . .	37
3.6	Sensor positioning and the flow direction to adjust the flow rate. . . . .	38
3.7	Experimental set-up for the flow experiments (left), and the head-on-device made from poly (methyl methacrylate) (PMMA) by mechanical milling (right). . . . .	40
3.8	Five steps of droplet formation at the T- junction, the simulation is shown on the left (channel width 10 lu) and the experiment is shown on the right. . . . .	40
3.9	Simulation of squeezing regime for 40 lu. . . . .	41
3.10	Droplet generation process in middle flow for 40 lu. . . . .	41
3.11	Influence of the resolution in the flow rate of 0.26 ml/min. The channel resolution is 10, 20 and 40 lu which correspond to 42600, 170400, 681600 domain grid points. . . . .	42
3.12	Flow rate relation with droplet size in simulation and experiment. . . . .	43
4.1	Pin typed initial geometry (left), velocity map, white represents high mean velocity and dark represents low mean velocity inside a 20x20 cell (right). . . . .	46

4.2	Optimized geometry introduces more resistance in the shortest path of reactant.	47
4.3	CAD drawing of first prototype. Inlet and outlet are visible on top left and bottom right. Notice the support geometry near inlet/outlet. "Detail F" displays a single support structure and "Detail C" displays mesh on the channels.	48
4.4	Front and back as well as inlet and outlet of the first prototype. . . . .	49
4.5	First prototype for anode side manufactured on the platform (left), mesh like structure on the parallel channels (right top), deformation caused by the internal stresses inside the 1.4404 stainless steel part (right bottom). . . . .	49
4.6	First prototype contains two components: <i>A</i> side which is the material from the base platform and <i>B</i> powder sintered material which was added to the top layer (left), CAD design of the supporting structure (right). It present the support geometry prior its removal by sinker EDM. . . . .	50
4.7	Slice from the first prototype, flow field is yellow and solid walls are in blue (left), average velocity in each channel computed by LBM (right). . . . .	51
4.8	Algorithm to change individual channel width. . . . .	52
4.9	Channel width distribution in the channels. . . . .	53
4.10	The optimized channels (left), the algorithm has thickened the walls differently to reduce the flow rate locally. Volume flow rates in each channel (right). . .	53
4.11	2D simulation of initial geometry with COMSOL left and with LBM right. .	54
4.12	2D simulation of optimized geometry, COMSOL (left) and with LBM (right).	54
4.13	2D (left) comparison to 3D (right) simulation for optimized geometry with COMSOL. . . . .	55
4.14	Proposed 3D flow field geometries for AM, from left to right, first prototype, sloped parallel flow field, and cross-flow field. . . . .	56
4.15	channel grouping in the inlet area for sloped parallel flow field (left). Cross parallel flow field (right) this geometry has an small arcs inside the channels to create the support structure for the top layer of the channel. . . . .	56
4.16	Flow field inside the cross-flow field structures, bottom view (left), inlet/outlet supporting structure (right). . . . .	57
4.17	Velocity distribution in the first AM prototype (left), velocity distribution in the midsection of the channels (right). . . . .	57
4.18	Velocity distribution in sloped parallel flow field (left), velocity distribution in the midsection of the channels (right). . . . .	58
4.19	Pressure distribution in different flow field. . . . .	58

4.20	Velocity distribution in crossed flow field (left), velocity distribution in the midsection of the channels (right). . . . .	59
4.21	Polarisation curve of the first prototype and reference system in experiment (left), The fuel cell assembly in the DHBW test rig. Voltmeter shows the operating voltage of the PEMFC (right). . . . .	60
5.1	Top view of possible integration of fin-shaped geometry in single first channel from left (left), cutaway side view (right) the structure is removed for the visibility. . . . .	62
5.2	Fin shaped structures added to a flat surface. Top views of the fin-shaped structure studied here and manufactured by SLM in a picture from above (left), CAD in an isometric view (middle), and original PDMS part (right). Notice the different scales and compare the rough metallic structure manufactured by SLM (left) with the smooth surface considered in [91] made of resin (right). . . . .	63
5.3	The pictures represent the basic element of structure manufactured by SLM. [left] Structure A and [right] structure C of the experimental set-up (Figure 5.4) corresponding to the smallest and largest lengths specified in Figure 5.5. Colours indicate height measured from the steel platform. . . . .	65
5.4	Three adjacent structures exhibiting fin shaped channels added to the steel base by SLM. [left] Actual A, B and C structures. [right] CAD design documenting the total length and width of each structure, in millimeters. . . . .	65
5.5	The elementary pattern from which we deduce the channel wall basement called R region. The elementary wall basement with a thickness of $0.1mm$ ( $R_0$ in the text) is in blue. the channel elementary cell is in white. Both are included in the rectangle 'abcd'. Adding copies of this rectangle adjacent to its parallel to y sides defines one channel and its walls. Then, adding adjacent copies of the ensemble forms the channel walls basement for structure A,B or C. . . . .	67
5.6	Average velocity absolute values of water wicking in $x$ and $-x$ directions for the three different channels A, B and C. . . . .	68
5.7	Time evolution (time unit in seconds) of directional drop wicking on structure B (middle structure). The bottom of the structure appears as white and the top is dark. Water is colored for better visibility. The first picture shows the pipette that places a water drop on structure B at time $t_1$ . At time $t_2$ the drop has already begun to wick through the channels. At time $t_3$ , the structure has been completely flooded in the positive direction while wicking is slower in the negative direction. Transport in the negative direction is completed at time $t_4$ . . . . .	69

5.8	VOF two-dimensional simulation with $\theta = 50^\circ$ and the geometry of the horizontal section of channel A. . . . .	71
5.9	Snapshots of the asymmetric transport using the 2D VOF simulation. Parameters are as in Figure 5.8. . . . .	71
5.10	3D simulation of liquid wicking driven by capillary forces on channel A. Blue color represents liquid volume. Contact angle is $50^\circ$ . The simulation domain is eight elementary cells long. The parallelepiped size is $\ell_x = 0.7mm, \ell_y = 0.38mm$ , and $\ell_z = 0.4mm$ . . . . .	72
5.11	Simulated liquid velocity and free surface height during the wicking of a parallelepiped of liquid over a single fin shaped channel. The top of each sub-figure documents the velocity, and at the bottom we see liquid height distribution. Contact angle is $50^\circ$ . The simulation domain consists of 6 elementary cells. The initial liquid parallelepiped is one elementary cell long. . . . .	73
5.12	VOF simulation detailing fin filling in the $x$ direction. The continuous color represents the liquid free surface. Arrows display the velocity on the liquid free surface with a color code for the amplitude. However, instead of being started from an initial condition as for Figure 5.10 and Figure 5.11, the simulation is issued from the continuous fluid inlet condition described in Section 5.5.4. The time is set to zero when the liquid enters the fin region. . . . .	74
5.13	Spreading of water beyond the pinning point ( $t = 1.17ms$ ) and backflow ( $t = 1.70ms$ ) for a static contact angle $\theta = 30^\circ$ . Velocities and liquid height are documented at the top and bottom of each figure, respectively. The initial condition is a two elementary cells long liquid parallelepiped. The channel geometry corresponds to the pattern A. . . . .	76
5.14	Average velocity of the front as a function of the static contact angle $\theta$ . Blue crosses indicate front velocity in the $+x$ direction while orange dots indicate the front velocity $-x$ . Beyond $\theta \geq 30^\circ$ the front in the $-x$ direction is pinned and then velocity is not indicated. The geometry corresponds to the smallest pattern A of Figure 5.5. . . . .	76
5.15	Influence of the pattern geometry on the average velocity of the front in the positive $x$ direction. The contact angle is $\theta = 30^\circ$ . . . . .	77
5.16	5. VOF simulation with an inlet at the bottom of channel A. Inlet flux is $1.06mm^3/s$ and $\theta = 50^\circ$ , . . . . .	78
5.17	LBM simulation with an inlet (red arrows) at the bottom of channel A. Contact angle $\theta = 50^\circ$ . . . . .	79
5.18	(a) Diffusion at the water/air interface in VOF simulation with compressive scheme. Parameters are as in Figure 5.10. (b) LBM simulation performs clear phase separation without excess diffusion at the interface with an equal number of cell elements. Parameters are as in Figure 5.17. . . . .	80

5.19 Evolution of water transport in channel type  $B$  in the negative direction. Experimental conditions are the same as in Figure 5.7. In the first snapshot ( $t = 0ms$ ) the front is blocked at the  $E_r^i$  edge. At  $t = 12ms$ , the front is still pinned but a small amount of water can be observed in the tip of the fin. The fin volume is progressively filled up till  $t = 24ms$ . At  $t = 30ms$  the water continues into the next cell. . . . . 80

# List of Tables

2.1	List of components, materials and their properties for reference system. . . .	20
2.2	Boundary conditions for PEMFC simulation and experiment. . . . .	22
2.3	Table of variable names used in the simulation of the reference PEMFC. . .	23
3.1	T-Junction Boundary condition in simulation and experiment. The 1-mm channel was simulated using 10, 20, 40 lu channel sizes. . . . .	39

# General introduction

For the past century our demand for electricity has increased. The required energy in many factories and cities are Increasing, the fossil fuel resources are depleted. Moreover, the pollution causes many problems in large cities for example, the CO<sub>2</sub> as it is shown in Figure 2 has increased in the past years drastically. In addition, mean temperature on the earth surface has increased about 1 degree Celsius. Therefore, the demand for the renewable energy is increasing. 21th century will be the turning point from fossil fuels to electric vehicle. The drastic change on how the people travel depends on the development of the batteries. Batteries are the first factor limiting the use of electric vehicle. Batteries bound the user by their capacity which lead to limited range moreover, slow recharging process. Is another disadvantage of batteries. Larger batteries result in increase in total weight of the vehicle which then influences other parameters such as: increase in consumption costs of moving the additional mass, decrease in drive agility, drive dynamics and total efficiency. In contrasts, fuel cell is a type of battery with unlimited reactants. It will operate as long as the reactants exists. Refilling a hydrogen tank does take about three minutes compare to hours for electric vehicle. Generally hydrogen fuel cells have higher energy density compare to batteries [1], [2].

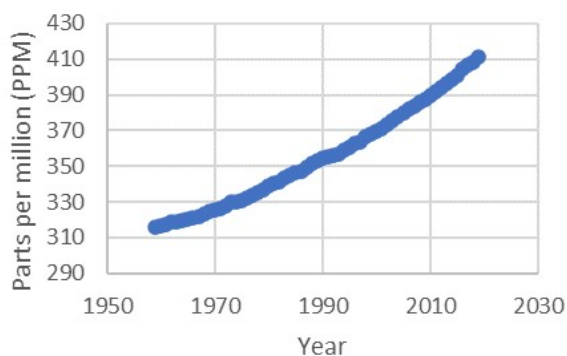


Figure 1: Increase in carbon dioxide in the world [3].

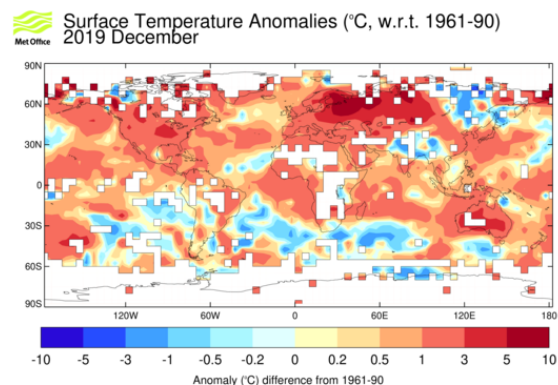


Figure 2: Temperature rise on earth surface(right)[4].

FCs are not new inventions, the principal of what became the first FC was demonstrated by Humphry Davy in 1801. In 1832 William Grove made the first gas voltaic battery. The proton exchange fuel cells are invented by general electric in 1950. Ten years after NASA used fuel cells in space missions. In 20th century with manufacturing methods improvements, sensors and electronic management systems the fuel cells became more efficient and reliable. An example is the first commercial fuel cell car Hyundai Tucson FCEV was introduced in 2013. FCs are very promising energy technology. They are very efficient compare to internal combustion engines. FCs combined with batteries as hybrid cars have high conversion efficiency. Theoretical maximum possible energy efficiency of a FC is 83% [5]. They are emission free solutions. Product of the hydrogen and oxygen reaction is water in moisture and fluid form. FCs have no moving parts and therefore, it promises longer lifetime compared to the mechanical components which needs more maintenance. The average lifetime of

a vehicle is 10 to 12 years, the FCs with the 3000 to 5000 operation hours meet the life time expectancy in the automotive industry. They are modular, they can be stack up to upscale the system. The hydrogen is non-toxic. Hydrogen has some properties which makes it safer compare to other fuels for example it has 3 times less energy density compares to natural gas in the case of a leakage it is less dangerous compared to natural gas. Moreover, due to its small molecules it dissipates much faster into the air than natural gas. These properties make hydrogen safer than other gas fuels. The product of hydrogen reaction is water which is harmless however, inhaling the fumes and soot of gasoline are hazardous. With a proper design the water generated in the system can be reused for drinking or other applications. FCs are quiet and can be made in various size and weights [5] These advantages make FCs distinctive devices to convert the energy, environmentally friendly. However, fuel cells are still less used as other kinds of batteries, especially in automotive industry. The present work contributes to general active research that tends to overcome some obstacles that make them more efficient than other solutions. To give a flavor of it, remind that fuel cells are based on an electrochemical reaction that returns electric current. Avoiding too large variations of the latter is highly desirable, and this depends on bipolar plate (BPP) carry reactants and products. The operation of the fuel cell is highly dependent on correct feeding of reactants and removing reaction products to harvest electric current in various conditions.

This thesis aims at improving the intensity and the stability of the electric current produced by fuel cells by optimizing the geometry of monopolar plate. Computational fluid dynamics is our basic tool. However, the link between current intensity and fluid flow involves a number of coupled quantities, and empirical equations. Various limitations restrict the validity of the solution of this system that assumes steady operation and purely gaseous flows. However, the solution agrees with experiments performed in steady conditions. It also points out the necessity of designing channels that distribute the reactants equally. Therefore, the author uses the above system to check the efficiency of fuel cells involving innovative geometries of fluid flow domain. He separately studies two phase flows that can occur in cathode. To this end, the author performs fluid simulation which he validates against available experimental data. In addition, to solve flooding in BPP a pattern to transport the liquid water out of the channels is proposed. The innovative structure applies a special pattern on the surface which enhances wicking effect in a privileged direction. This study uses the two phase fluid LBM, compares it with volume of fluid (VOF) method and corroborates it with experimental study.

Before completing this program, in Chapter 1 the author provides fundamental information about the fuel cells that are considered here, and specifies his approach. Chapter 2 enters deeper into the details of steady fuel cell operation, and the here considered modifications of fluid flow domain. Chapter 3 details the Lattice Boltzmann method (LBM) that simulates two phase flow, and its validation against experimental data. Chapter 4 documents discoveries regarding the electric current produced by fuel cells using different geometries. Section 5 opens new perspectives by combining numerical and experimental approach to passive directional transport on surfaces with bio-inspired patterns.

# Chapter 1

## Objective of the thesis: fuel cell optimization

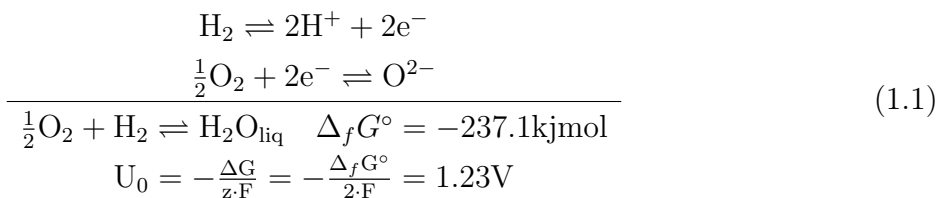
### 1.1 Introduction

PEM fuel cells have existed around two decades. However, there has been many challenges until now to make them more common and usable at large scale. All fuel cells are based on an electrochemical reaction that yields electric current when they are supplied with reactants. In the PEM fuel cells that we consider here the latter are hydrogen and oxygen in gaseous form, while reaction by product is water (liquid or gaseous). Moreover, electric current stability is absolutely necessary for automotive applications, and depends on flow of reactants and water inside the fuel cells. Here we concentrate our attention to PEM fuel cells designed to optimize the transport of reactants. The main flow field which transports the reactants is parallel flow field in BPPs. There have been various attempts to design and manufacture bipolar flow fields to improve the transport of reactants (hydrogen and air). This thesis aim is to enhance low temperature fuel cell performance and stability by improving BPP or here monopolar plate channel design. To this end the author starts from PEM fuel cells that resemble the commonly used ones, and then modifies the geometry of specific elements. This approach is part of a project driven by DHBW in view of improving fuel cell efficiency by modifying the internal geometry of selected elements. The numerical simulation of fuel cell operation and flow of reactants and products inside them is the main task in this project. In view of fuel cell complexity, the simulations are compared with experiments conducted by another researcher in DHBW. The present chapter recalls essential of PEM fuel cells and explains the global philosophy of these objectives. Since PEM fuel cells are very diverse, firstly the author describes the ones which he consider in this work. Chapter structure is as following: it starts with the general principle of current production (in section 1.2). On this basis, in section 1.4 the author explains which fuel cell elements will be improved, and specifies details of their manufacturing. There are specific material constraints in designing latter which is explained in section 1.5.

## 1.2 Standard fuel cell and principle

### 1.2.1 Classical fuel cell element

At the heart of a fuel cell is the electrolyte where the reaction occurs. The reaction takes place on catalyst layers. Therefore, it is a surface-based reaction. The electrolyte is located inside the proton exchange membrane (PEM), schematically represented on Figure 1.1. Low temperature PEMFC works between 60-80 C° [5]. The operating principle of PEM is relatively simple. However, it is a complex dynamic system. Hydrogen fuel cells are limited by either nature of chemical reaction (Equation 1.1) or by the supply of the reactants which take place in BPPs. The PEM separates oxidation (electron discharge in anode) and reduction (electron consumption in cathode). It is a polymer membrane which conducts protons but it is not electrically conductive and it is impermeable to gases. The membrane behaves as an electrolyte; it is packed between two porous electrically conductive electrodes. Between the membrane and each electrode there is a thin catalyst layer to accelerate the chemical reaction described below. During the reaction protons are conducted through PEM to cathode. Since the PEM is not electrically conductive the electrons travel through the external circuit and generate electrical current. The reaction releases -237.1 kJ/mol energy which leads to 1.23 V open cell potential under reversible operation.



$z$  is the number of electrons in reaction,  $F$  is the Faraday constant,  $\Delta G$  is Gibbs free energy and  $\Delta_f G^\circ$  corresponds to 298.15 K and 100 kPa temperature and pressure. The reactants are fed to the system inside BPPs. Hydrogen breaks into electrons and protons. Protons pass through the membrane and electrons travel through the external circuit including collectors. BPPs are conductive and transfer the current to current collectors. After the work is done in the external circuit, the electron joins to the hydrogen and oxygen which forms water near the cathode. Since water has less entropy than reactants, it can be pushed away from the cell by the excess amount of oxygen or air.

### 1.2.2 Fuel cell stack

In subsection 1.2.1, we mentioned the theoretical fuel cell voltage 1.23 V. However, in practice it is lower than 1 V. We increase the voltage of a single fuel cell by packing multiple of them together, each cathode being connected to next anode BPP in series. Such a pack is called a stack, and is shown in Figure 1.2.

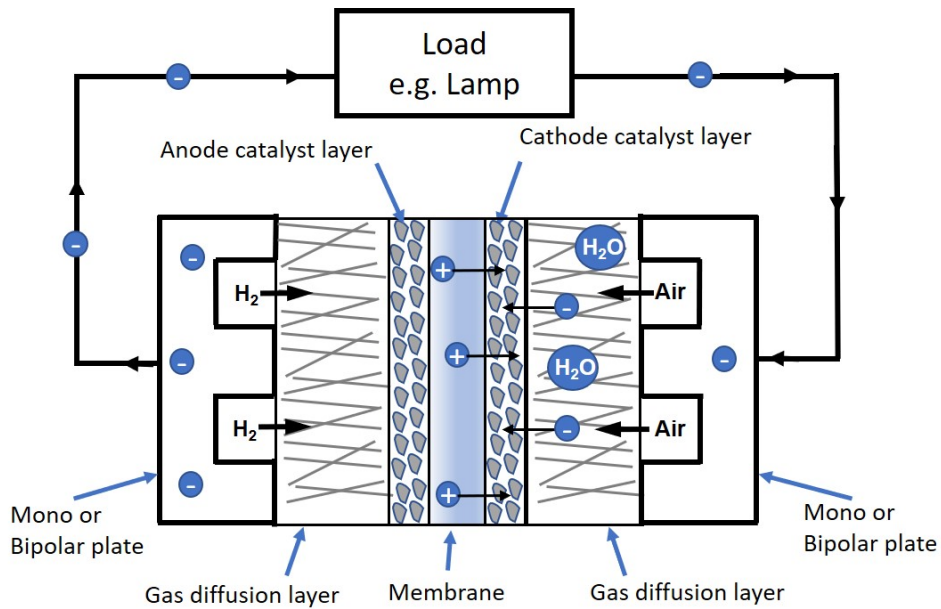


Figure 1.1: Structure of a fuel cell.

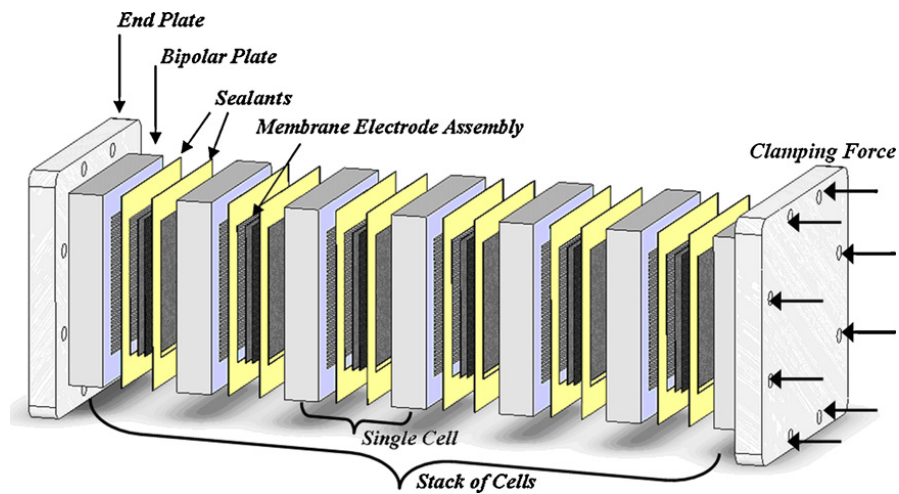


Figure 1.2: Fuel cell stack [6].

### 1.2.3 The roles of the components of a fuel cell

Each elementary fuel cell is composed of several elements that play different roles. They are a proton exchange membrane, two electrodes, two gas diffusion layers, two BPPs.

### 1.2.3.1 Proton exchange membrane

Polymer electrolyte membrane, proton exchange membrane (PEM) or ionomer membrane [7] is a non-conductive thin layer with thickness ranging between 50 and 175  $\mu m$  [8]. PEM is a solid polymer film made of a thin plastic film such as perfluorosulfonated acid polymer. It is permeable to protons even though the membrane could be fully saturated by liquid water. This forces the electrons to travel in the external circuit to generate power. Perfluorosulfonic acid (PFSA) membranes have a low cell resistance ( $0.05 \text{ Q cm}^2$ ) for a 100  $\mu m$  thick membrane with a voltage loss of 50 mV at  $1 \text{ A/cm}^2$  which is fairly low [8]. In many applications and here also the membrane is integrated in an assembly called membrane electrode assembly (MEA) with gas diffusion layers (GDLs) and catalyst layers (CLs).

### 1.2.3.2 Electrodes

Each electrode is made of a catalyst layer sandwiched between membrane and electrically conductive porous material. The reaction takes place on triple phase boundary where the catalytically active electrode particles electrolyte phase and gas pores intersect. The role of the electrodes is to provide local sites for the reaction where the proton, electron, and surface meet each other. The catalyst is often made of Platinum particles with 4 nm surface size or smaller and  $0.3\text{-}0.4 \text{ mg cm}^{-2}$  surface distribution. The porous material is typically made of carbon powder with about 40 nm surface size and high mesoporous area less than  $75 \text{ m}^2 \text{ g}^{-1}$  [5]. In order to accelerate gas transport, the electrode must be porous and as thin as possible, in contrast to the catalyst that must have large surface area to accelerate the reaction.

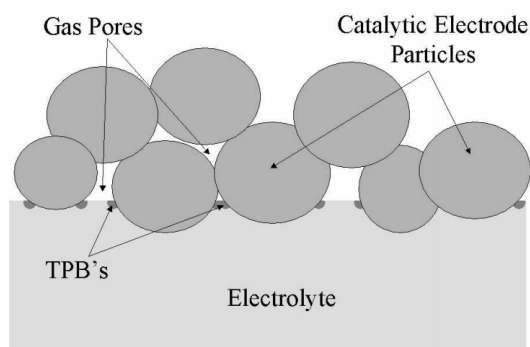


Figure 1.3: Simplified diagram of the triple phase where the reaction take place [9].

### 1.2.3.3 Gas diffusion layer

Gas diffusion layers (GDL) located between catalyst layer and BPPs consist of two parts. One is made of dense carbon fibers which build a porous material. The other one is a microporous layer (MPL) at the interface of GDL and catalyst layer. MPL is a coating that consists of composite layer of carbon particles with PTFE [7]. GDL provides mechanical

support, ease the transport of reactants and water. They are electrically and thermally conductive, and collect the current from the catalyst and pass it to the BPP. They create reaction zones not just in the channels but also in the contact zone (also known as rib, channel support, or land) between BPP and GDL presented in Figure 1.4.

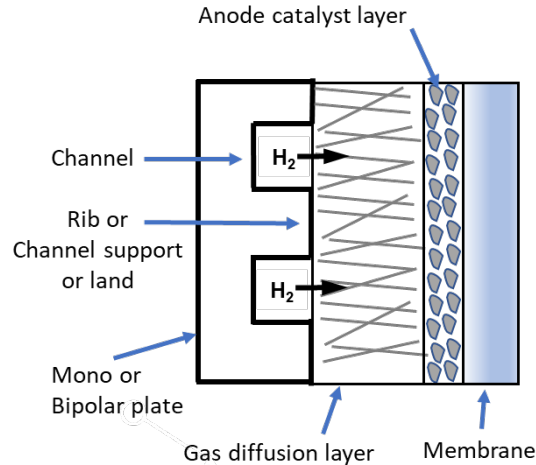


Figure 1.4: Rib and channel positions are shown in the anode side.

The manufacturing process [10] of the GDL consists of several steps shown in figure 1.5. The carbon fiber paper are manufactured similar to papermaking. The chopped carbon fiber which are in a solution of water and alcohol are placed wet on a web. Then, it get dried and wound on a spool. In the next step the porosity of the fabric is defined by amount of the resin and the graphite added to the paper. This fabric then oxidize and graphitize by heat. In the next step wetting condition can be adjusted by adding fluorinated ethylene propylene (FEP). In the last step an MPL is laid on the substrate and sintered to fabric to achieve required porosity.

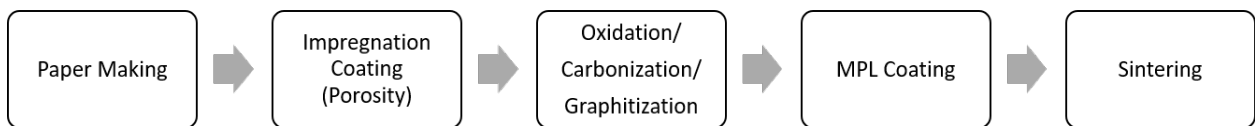


Figure 1.5: Process of GDL manufacturing.

#### 1.2.3.4 Bipolar plate (BPP)

Transporting water and reactants is the function of bipolar (or monopolar) plate. The difference between monopolar plate and BPP is that the first one has single flow field and is adapted to a single FC. BPP, differently, has flow field in both sides and is adapted to FC stacks. BPP has two sides in which the cathode of a cell is the anode of the neighbor cell,

which makes it more compact. For research focused on single FC, however, one commonly uses monopolar plate. The bipolar or monopolar plate must fulfill mechanical and material requirements. Moreover, from the fluid mechanic perspective the requirements are low pressure drop in gas flow, and continuous transport of liquid water and coolant distribution. The material must be electrically conductive, dissipate heat, resist corrosion, be mechanically stable and manufacturable. Therefore, our designed geometry must be compatible with these requirements for a stable performance.

Since BPP has direct influence on the transport of the reactants, its design strongly influences fuel cell efficiency. Hence, optimizing the BPP geometry was a subject of study of various researchers. We mention a number of these researches [11]–[15] and their outcomes are mentioned. In general, the flow domain in BPP should avoid head losses and enhance flow homogeneity. Wang et al. [16] studied pressure drop and volume flow rate inside the various geometries of BPPs. They highlighted four types of conventional BPPs depicted in Figure 1.6. The first type shown in Figure 1.6.a is a single serpentine, which has the best flow distribution. However, it implies high pressure drop in the channel. The pressure drop can be as large as thousand times the one observed on parallel configuration. Therefore, the FC with single serpentine requires a powerful pump. The second type shown in Figure 1.6.b is multiple serpentine configuration which has the lowest pressure drop. However, the flow field is non-uniform. The third configuration is pin typed flow field. It easily distributes the gases on membrane surface. However, the gases are unevenly distributed and the flow exhibits stagnation areas which lead to water blockage due to uneven flow distribution: liquid water cannot be removed from the flow field. The fourth configuration is straight parallel. This is one of the most interesting flow fields, it is easy to manufacture and has low pressure drop. However, it has some drawbacks such as inhomogeneous flow field and is prone to water blockage in channel. Wang et al. suggest that this configuration can be optimized by varying the structural parameters. Two years later Guo et al. [15] made a mathematical model to optimize this structure. They proved that varying the channel width homogenize the flow field.

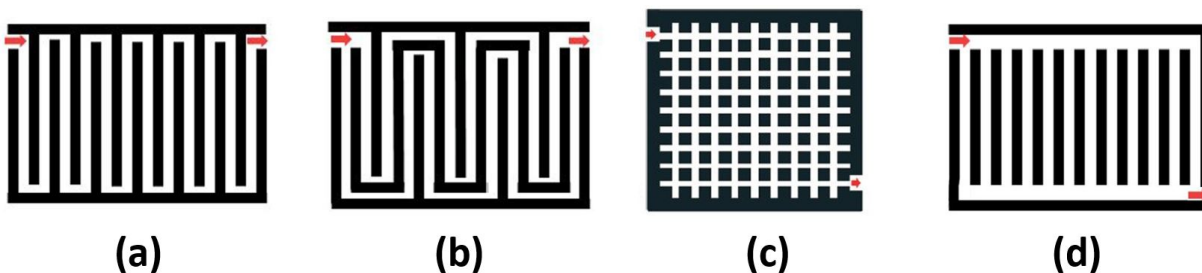


Figure 1.6: Flow field layout configuration: a) single serpentine, b) multiple serpentine with two channels, c) pin typed flow field, d) straight parallel. [12].

In addition to the above-mentioned flow fields some researchers find inspiration in Nature in view of optimizing the flow fields. This is called biomimetic (or bio-inspired, bionic) design. Example of such geometries are tree liked structure, fractal design and lung flow field.

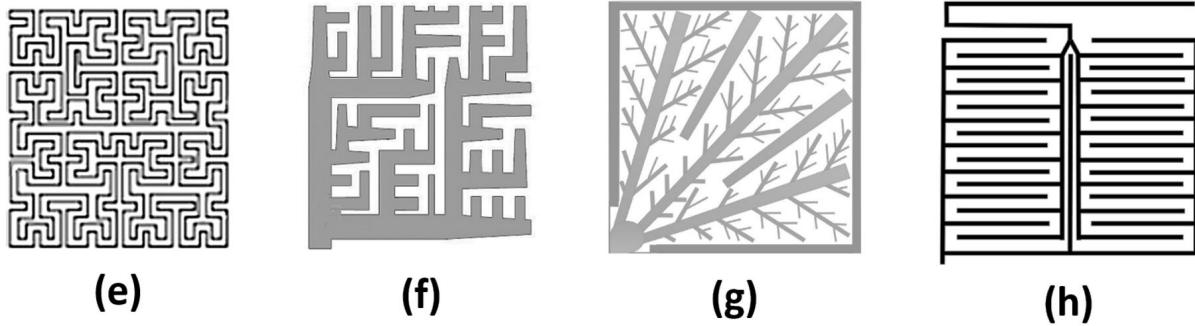


Figure 1.7: Biomimetic flow fields from left to right. Fractal design(e), tree-like design(f,g), lung inspired design [13].

After the flow distribution pattern, channel section in geometry plays an important role in the design of the channel geometry. As we have mentioned the two-phase flow appears in the cathode side: at least on this side the channel design should limit water blockage. Another important aspect of the flow field is the shape of the channel section. Salah et al. [14] studied the triangular, rectangular and trapezoidal shaped channel section using multiphase LBM and concluded that for water removal the rectangular shaped channel is optimum. Ahmed et al. [17] found rectangular channel cross-section produce higher cell voltage. However, the trapezoidal channel produces more uniform reactant and local current density distribution. They concluded optimum channel-to-land ratio for a fixed channel width of 0.8 mm and height of 1 mm. At high operating current density, an optimum channel-to-land ratio is 1.3 to 1.4. Another important parameter which influences the transport is surface wettability. It was studied by [14], [18]. Lu et al. found by experiment that hydrophilic channel surface has more stable performance than non-treated channels. Moreover, they found hydrophilic channel surface might be advantageous for transport of large droplet volume. Next section describes the problems which this work focused on to, and the solutions that the author proposes in this thesis.

### 1.3 The improvements which we want to study

This work has two aims. The first one is integrating GDL into BPP. Another one is managing the liquid water produced by electrochemical reaction. These two aims are pursued in view of increasing fuel cell power and efficiency.

#### 1.3.1 Integrating GDL into BPP

Integrating GDL into BPP is expected to reduce the number of components in the FC. It is a milestone if a new design can distribute the flow of reactants evenly in new BPP geometry. This work exploits the flexibility of design offered by the additive manufacturing (AM). This

technique may reduce manufacturing costs and become a competitive alternative for internal combustion engines. The use of AM in PEMFC was not studied before, more specifically using micro selective laser melting (SLM) and the material of stainless steel . In order to use this method, the author investigates the feasibility of such work and discover its potentials. During the manufacturing of integrated GDL in BPP, the author researched various flow fields in BPP. In the next step an algorithm for geometry optimization was developed to optimize the parallel channel geometry.

### 1.3.2 Water management

An electrochemical reaction resumes the very basic principle that allows fuel cells to yield electric current when they are fed with oxygen and hydrogen. However, current stability is absolutely necessary for any use of such devices, and more especially for FCs designed in view of automotive transportation. It turns out that stability depends on appropriate evacuation of reaction products, especially liquid water. This depends on fluid flow that occurs at microscopic scale in BPPs of FC stack. One of the products of the reaction in the cathode side of conventional fuel cells is liquid water. A minimum level of hydration is required to facilitate efficient ionic conductivity in the PEM. Fuel cell dehydration decreases the conductivity and the excessive amount of water disturbs the flow of reactants and leads to flooding in cathode side. The relation between cell voltage, current and pressure drop is depicted in Figure 1.8. Flooding causes various problems such as: voltage loss at high current density due to limitation in mass transport [16], and voltage instability at low current density [19]. Therefore, maintaining the adequate amount of water in PEM fuel cells is essential. There are various approaches to solve water management such as increasing the temperature of the reactants or changing the stoichiometry in the FC [20]. Here an innovative approach were taken to drain the liquid water using passive transport which is described in the Chapter 5.

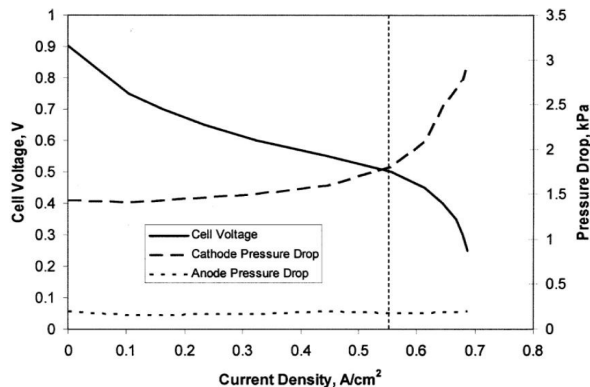


Figure 1.8: Cathode flooding in current density above 0.55 lead to increase in pressure drop and decrease in the cell voltage (cell temperature 51°) [21].

### 1.3.3 Power and efficiency

The efficiency of the fuel cell is defined by the ratio of produced power ( $P_{el}$ ) to theoretical power ( $P_0$ ).

$$\eta_{el} = \frac{P_{el}}{P_0} = \frac{UI}{U_0I} = \frac{U}{U_0} \quad (1.2)$$

$U$  and  $U_0$  are potential and theoretical rest potential.  $I$  is electric current. The efficiency of the fuel cell is related to the drawn current. Therefore, the potential-current density is important for the fuel cell assessment. The efficiency and power density relation to current density is shown in Figure 1.9. The potential loss appears in three main groups. (I) The kinetic region in which the drawn current is small and is related to reaction. (II) The electrolyte or ohmic losses region, in this region the conductivity of the electrolyte and the internal FC components are main limiting factor and (III) the mass transport region, this region present the concentration of the reactants limits the FC performance in the maximum current density [22], [23]. An important point is these regions are not separate, the I, II, III presents which losses are dominant in that region.

This diagram presents the importance of reducing the mass transport loss specially in peak current density. Minimizing the dominant transport losses increase the power and efficiency of the FC.

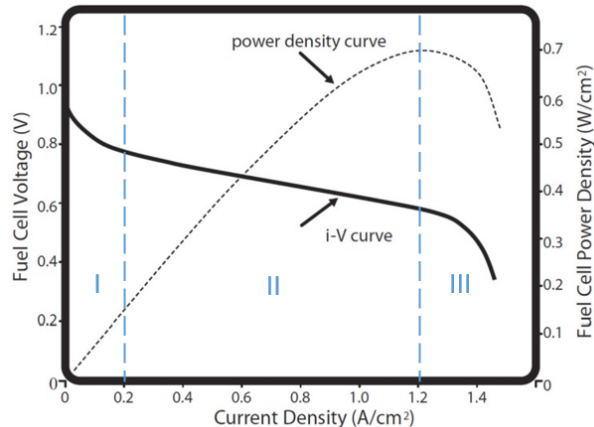


Figure 1.9: Efficiency and power density relation to current density [24].

## 1.4 Strategic two-phase fluid flows in GDL and BPP

Water management is the biggest challenge in the PEM fuel cells. Hence, new concepts of heat and water exchange in PEMFC must be investigated [2]. Water management influences significantly the catalyst and membrane's lifetime [7]. Water dissolves Pt from the catalyst layer and damages the supporting material in GDL. Flooding can block the pores of the

GDL and dramatically reduce the mass transfer into the catalyst layer. Moreover, reactant starvation damages the catalyst support. In flooding the water progressively dissolves and washes out the GDL and catalyst layer. This contaminates the PEM and modifies its mechanical properties. This causes other problems, such as interrupting proton transfer and fracturing the membrane. Flooding is mostly appearing in cathode. It is possible to see the excess water in anode side. However, it takes time for water to spread to anode side. Water blockage can be measured using the reactants pressure drop in the cell. High pressure-drop at current peak causes flooding. In order to solve flooding two solutions are used: immediately increase the hydrogen flow rate or increase cell temperature [7].

Dehydration can reduce the membrane mechanical stability by forming tearing and cracks. Anode is more prone to dehydration at high temperatures and currents because of electro-osmosis forces which take the water from anode with back diffusion to cathode. Dehydration increases the electric resistance inside the cell and reduces the generated voltage. Strong dehydration can cause permanent damages in short time as 100 seconds to PEM [25]. Dehydration can be diagnosed by monitoring the membrane resistance. The increase of the resistance reveals the membrane dehydration level.

## 1.5 Solutions studied in this work

Section 1.4 suggested preventing flooding and dehydration while distributing the flow uniformly provides a good chance of improving battery yield and electric current stability. Hence, the present thesis aims at discussing innovative designs that help progressing in this direction. To this end we study new geometries for the flow field. However, we account for limits imposed by manufacturing process and material properties. Our main tool is CFD simulation, but we already have seen that fuel cell behavior depends on several coupled quantities: checking simulation against experiment is mandatory, especially in view of industrial applications. Therefore, we perform our simulations in conditions that are those of an experimental device, of which we give an idea below.

In classical PEM fuel cell most of fluid flows through a domain composed of two different adjacent media: channels carved in BPPs at their interface with GDL, and GDL is a porous medium. In the above-mentioned experimental device, we form a new device that replaces the ensemble made of channels and GDL. In the new device there is no porous material. A new grid made of metal was designed to be placed on the parallel channels instead of GDL. In order to use the smaller monopolar replacement it must be put in another larger component with a cavity to hold the monopolar plate in place. We embedded it into a metallic parallelepiped. We excavate the necessary room in the classical BPP, so as to easily insert the metallic parallelepiped. In this work the BPP with the GDL is called reference system. Additive manufacturing(AM) offers new possibilities to create prototypes and test new ideas. Here a special AM method was used that manufactures fine parts with stainless steel material which outperforms the requirements in BPPs. In contrast, AM introduces specific constrains which we comment at the end of the chapter. This thesis proposes new designs for anode and cathode using AM method. These designs benefit from the advantages of AM and account for its limitations. In anode and cathode there are different parameters which

should be considered to improve the performance of the FC. Hydrogen and air have different viscosity, that means the resistance in the flow is higher for air compare to hydrogen. For example: to achieve same flow rate in a channel air needs higher inlet pressure compared to hydrogen. The flow field in anode side is optimized separately on the basis of gaseous hydrogen, this topic is explained in Chapter 4. Water management in monopolar plate will be studied in Chapter 5. The basic of discoveries in anode design can be applied to cathode flow field however, the focus in cathode was to manage the liquid water by innovative micro structure pattern.

## 1.6 Additional constraint: 3D printing manufacturing

Micro laser sintering is a powder bed-based AM technology, often called selective laser sintering or selective laser melting. A 3D-CAD model is used to print the product. The model is divided into various layers. In the manufacturing, a thin layer of powder is applied to build the platform (Figure 1.10). The powder is fused by a laser beam according to each layer. The platform is lowered and this process continues until all the layers are completed and the part is finished. Our project partner, 3D MicroPrint, can manufacture various materials such as stainless steel , molybdenum, and tungsten. One of the key issues is that 3D MicroPrint works with metal powders with a maximum grain size of  $5 \mu m$ . Therefore, the resolution of the final product is limited by the focus of the laser beam; which is approximately  $30 \mu m$ . Moreover, the maximum size of the printed component can be  $4 \times 4 \text{ cm}^2$ . Since the AM is a new method. The limits of using this method is not known for manufacturing the high precision parts of the fuel cell. More specifically, influence of the long flat thin surfaces and complex geometry in manufacturing and removing the residue powder. In this study first the feasibility of the AM will be discussed and then the author deploys this method to propose a new design which integrate the GDL with BPP in a single product.

Now the basic principles of fuel cell operation were explained the author can explain more details of the considered modifications for FC improvements. The author analysis FC on the basis of a classical model that allows us to simulate the fuel cell operation. Some of the proposed geometric modifications can partly be studied with the help of this model which is not sufficient for water management, and will be complemented by other approaches.

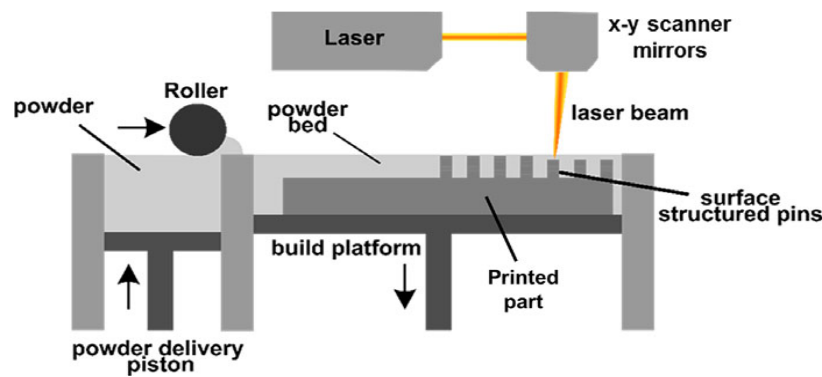


Figure 1.10: Manufacturing process using micro laser sintering [26].

# Chapter 2

## Fuel cell physical model and methodology

### 2.1 Introduction

Simulating fuel cell operation is a challenging CFD problem because it involves several coupled quantities that vary on different scales [27]. Moreover, the various couplings return a highly interdisciplinary problem. The actual FC operation is dynamic and responds to possible fast pressure and temperature changes. Moreover, hydrogen and oxygen are in gaseous phase while water may be in gaseous or liquid phase, especially near the cathode. Nevertheless, various simplifications are necessary to simulate all the quantities that are coupled with the delivered electric current. Here, the author starts from a model restricted to significant particular conditions of steady fuel cell operation, disregarding cathode flooding but conserving the symmetry between anode and cathode side. In this chapter the problem and the new adjustments are described in the thesis. Ferreira et al. [28] studied unsteady fuel cell operation and especially considered possible cathode flooding. However, their approach used a one-dimensional model for anode side, and a three-dimensional one for cathode side. In this chapter and in Chapter 4, we follow a symmetrical approach of steady fuel cell operation. In other chapters we will separately study non-steady aspects of two-phase fluid flows that may occur in strategic parts of the device. In this chapter we set the corresponding equations of our first approach of steady fuel cell operation in Section 2.2. In Section 2.3 we describe some innovative designs that we want to investigate in our simulation of working fuel cell. Then, in Section 2.4 we detail the fluid domain that will later host these innovations and its boundary conditions. We also demonstrate how solving the equations of Section 2.2 actually represents steady fuel cell operation. Solving these equations should clarify the fluid flow inside the fuel cell, and justifies deeper approach. In Section 2.5 the author mention detail and objectives on the basis of his findings, especially regarding the innovative designs in Section 2.3.

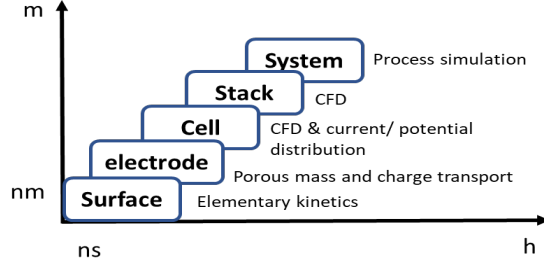


Figure 2.1: The fuel cells are highly multiscale systems.

## 2.2 The physical model that governs fuel cell operation in steady conditions

This section describes the equations that govern fluid velocity, reactant concentrations, and electric current density in steady conditions. For the latter quantity, different equations near anode and cathode were used. Moreover, the flow in the FC is considered as single phase gas in BPP channels.

In the channels, with the latter assumption we have free gaseous flows described by the steady compressible form of continuity and Navier-Stokes equation:[29]–[32]

$$\nabla \cdot (\rho \mathbf{u}) = 0 \quad (2.1)$$

$$\nabla \cdot (\rho \mathbf{u} \otimes \mathbf{u} - \mu \nabla \mathbf{u}) = -\nabla \left( p + \frac{2}{3} \mu \nabla \cdot \mathbf{u} \right) + \nabla \cdot [\mu (\nabla \mathbf{u})^T] \quad (2.2)$$

where  $\mathbf{u}$  is the gas velocity ( $\text{ms}^{-1}$ ),  $\rho$  is gas density ( $\text{kgm}^{-3}$ ),  $P$  is pressure (Pa), and  $\mu$  is the dynamic viscosity of gas mixture ( $\text{kgm}^{-1}\text{s}^{-1}$ ).

In standard fuel cells the gas flows through a porous domain that represents GDL and CL. The GDL is adjacent to the channels, and the CL is between GDL and membrane. In the porous medium, instead of Navier-Stokes equation we use the Brinkman equation. Moreover, the latter and the continuity equation exhibit  $Q$  that is mass source or sink ( $\text{kg m}^{-3}.\text{s}^{-1}$ )

$$\left( \frac{\mu}{\kappa} + Q \right) \mathbf{u} = \nabla \cdot \left[ -p \mathbf{I} + \frac{\mu}{\varepsilon} \left( \nabla \mathbf{u} + (\nabla \mathbf{u})^T - \frac{2}{3} (\nabla \cdot \mathbf{u}) \mathbf{I} \right) \right] \quad (2.3)$$

$$\nabla \cdot (\rho \mathbf{u}) = Q \quad (2.4)$$

and  $\varepsilon$  is the GDL porosity and  $\kappa$  is the GDL permeability ( $m^2$ ), and  $Q$  is mass source or sink ( $kg\ m^{-3}\cdot s^{-1}$ ).

Species mass transport in channels is described by Equation 2.5 Maxwell-Stefan equations. Species are hydrogen and water (vapor) on anode side: in this case  $k=2$ . On cathode side the reactant is oxygen, in fact inserted as a component of air that mixes several species. Only accounting for nitrogen returns  $k=3$  in Equation 2.5.

$$\nabla \cdot \left( \omega_i \rho \mathbf{u} - \rho \omega_i \sum_{j=1}^k \tilde{D}_{ij} \left( \frac{M}{M_j} \left( \nabla \omega_j + \omega_j \frac{\nabla M}{M} \right) + (x_j - \omega_j) \frac{\nabla p}{p} \right) \right) = R_i \quad (2.5)$$

$$\rho = \left( \sum_i x_i M \right) \frac{p}{RT} \quad (2.6)$$

In this equation  $\omega_i$ ,  $x_i$  and  $M_i$  are mass fraction, molar fraction and molecular mass ( $kg\ mol^{-1}$ ) for species  $i$ ,  $R$  is the universal gas constant ( $8.314\ J\ mol^{-1}\ k^{-1}$ ).  $\tilde{D}_{ij}$  is the binary diffusion coefficient of species and ( $m^2\ s^{-1}$ ), and  $T$  is the operating temperature of the cell. Moreover,  $M$  is the sum of the of the  $x_j M_j$ . Equation 2.5 is easily deduced from the system of equations that represent the Maxwell-Stefan equations in [33]. In Equation 2.5 the Equations 27 is solved from same reference for molar fluxes before inserting them in the usual transport equation. In general the  $\tilde{D}_{ij}$  that we have in Equation 2.5 are not the binary diffusion of species  $i$  and  $j$ . They are other parameters, the  $B_{ij}$  is given by Equation 26 in the latter reference: in general they depend on the molar fraction. Generally they consider binary diffusion in mixing of two chemical species in anode side. In contrast, on cathode side, three species (oxygen, nitrogen and water vapor) exists but Equation 2.5 remains valid. It provide two of them that have small mole fractions. This approximation is acceptable for air, and assumed in cathode side [29]–[32]. In porous GDL, the  $\tilde{D}_{ij}$  depend on the porosity and tortuosity of the medium. Apparently, all these elements are accounted by "batteries and fuel cells module" in COSMOL.

$R_i$  is the reaction rate of the species  $i$  in catalyst area. The reaction rate can be calculated using

$$\begin{aligned} R_{H_2} &= -\frac{M_{H_2}}{2F} i_a \\ R_{O_2} &= -\frac{M_{O_2}}{4F} i_c \\ R_{H_2O} &= \frac{M_{H_2O}}{2F} i_c \end{aligned} \quad (2.7)$$

$$\begin{aligned} \nabla (-\sigma_s \nabla \cdot \phi_s) &= S_s \\ \nabla (-\sigma_m \nabla \cdot \phi_m) &= S_m \end{aligned} \quad (2.8)$$

Where  $\sigma$  is the electric conductivity ( $\text{S m}^{-1}$ ),  $\phi$  is the phase potential and  $S$  is current source ( $\text{A m}^{-3}$ ) in which is define by:

$$\begin{aligned} \text{Anode: } S_m &= i_a \text{ and } S_s = -i_a \\ \text{Cathode: } S_m &= i_c \text{ and } S_s = -i_c \end{aligned} \quad (2.9)$$

Moreover, subscripts  $m$  and  $s$  denote membrane and solid, i.e. monopolar or BPP itself . To calculate current at the anode Butler-Volmer equation is used:

$$i_a = ai_{0,a}^{ref} \left( \frac{C_{H_2}}{C_{H_2,ref}} \right)^{0.5} \left( \frac{\alpha_a + \alpha_c}{RT} F \eta \right) \quad (2.10)$$

$$i_c = -ai_{0,c}^{ref} \left( \frac{C_{O_2}}{C_{O_2,ref}} \right) \exp \left( -\frac{\alpha_c}{RT} F \eta \right) \quad (2.11)$$

Where  $i$  is current density,  $\alpha$  is transfer coefficient,  $T$  is the operating temperature and  $\eta$  is the over potential. To calculate the current at the cathode Tafel equation would be used because the reaction kinetics is slower there than at the anode.

Here we describe how the simulation is performed and the order in which these equations are being solved. The simulation process iterates four successive steps. In the first step the current distribution is calculated by the Butler Volmer equation. In second step the flow parameters (such as velocities and pressure) are determined using Navier Stokes and Brinkman equations. In third step the concentration of the species is calculated using Equation 2.5 . In fourth step these results are coupled with the equations solved at first and second steps. Equations 2.1–2.11 describe the steady states of coupled gaseous flow (gaseous hydrogen and water on anode side, gaseous oxygen, nitrogen and water on cathode side), hydrogen and oxygen concentrations, electric current density and heat in cell compartments on anode and cathode sides. This thesis is part of a wider project that tends to improve intensity and stability of delivered electric current by adapting these compartments. The next section describes the initial standard fuel cell, then the adaptations are proposed for modified version. It describes how classical and modified version will be compared, and the constraints that limits the parameters of the latter in its optimization.

## 2.3 A new concept in fuel cell: integrating BPP channels and GDL

The aim of this work is to introduce innovative design to improve standard fuel cells. The manufacturing method is SLM that imposes constraints in dimensions. The constraints cause that instead of comparing with common standard we compare with a copy that satisfies them. This copy of the common standard will be our reference system.

The here planned improvements regard the fuel cell part that includes GDL and the BPP channels that supply the heart of the device with reactants and evacuate excess water produced by the electro chemical reaction. In standard fuel cell the GDL is a porous material sandwiched between channels carved in graphite BPP and rib on one side, and catalyst layer (another porous material) on the other side. Each classical fuel cell exhibits two samples of such element, on cathode and anode sides. Such classical fuel cell is schematically represented at the left of Figure 2.3. The plan in this work consists in replacing the set composed of channels and GDL by a single metallic element so as to decrease interfacial electric resistance. The replacement occurs on anode side only for the moment, and returns a fuel cell schematically represented at the right of Figure 2.3. In view of easily exchanging reference system and innovations, we managed it so that they all occupy the same volume that itself just fills a void created in a composite plate. Thus, the reference system is made of porous GDL and monopolar plate channels that are a rescaled copy of standard ones. Alternative devices will still have channels, and the porous GDL will be replaced by a metallic grid. Such alternative device will be called “integrated channel and GDL”. Integrated channels and GDL as well as reference system have exactly the same shape and dimensions, and occupy exactly the same position in the void created in the monopolar plate: the void is the insertion area milled in a composite plate which we see this position on Figure 2.2. More details will be given after essentials of the standard channels + GDL set are discussed.

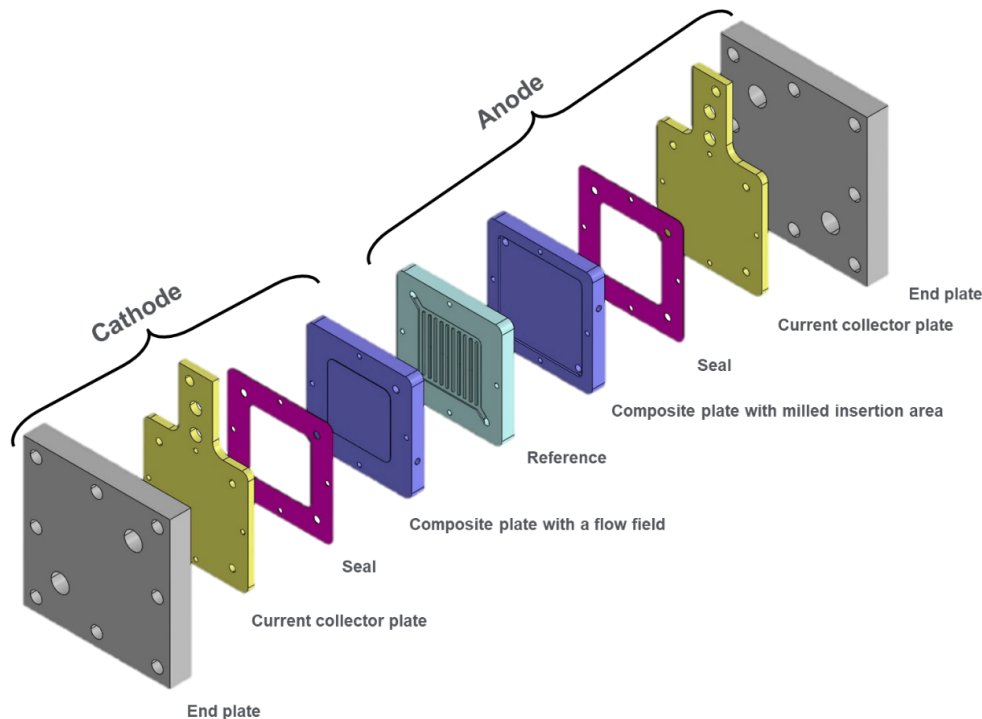


Figure 2.2: The assembly of the fuel cell. Either the composite plate with milled insertion area or reference plate can be used in the assembly.

### 2.3.1 Reference system

The reference system can be viewed as a part of the monopolar plate containing the parallel flow field channels which exchange the matter with outside. In the standard FC these channels are milled in a graphite composite plate adjacent to the GDL. This composition is illustrated in Figure 2.5 left. In the reference system the GDL is still a porous layer packed between monopolar plate and catalyst layer but the part (of the monopolar plate) that encloses the channels is made of metal. It is presented in Figure 2.5 right. It is manufactured by SLM and has size of 4x4 cm so as to fit into the insertion area milled in composite part. The milled composite plate and insertion area are depicted in Figure 2.4. This construction allows to replace reference and new prototype geometries without changing the other elements of the monopolar plates i.e. the composite plate. Moreover, the geometries which are being compared are made of same stainless steel material. Figure 2.2 one can see how the composite plate with insertion area is placed in the assembly, In addition a flow field made by SLM (demonstrated in 2.5 left) is necessary to make the FC operational. In Figure 2.5, the standard composite flow field (right) and the new replaceable flow field made of metal (left) are demonstrated. With this assembly new monopolar plates can be compared conveniently. In the Chapter 4 the author attempt to integrate the GDL by special structure in the monopolar plate using additive manufacturing and the results are compared to standard flow field made of metal.

### 2.3.2 Devices made of new BPP channels that do not need any porous GDL

The alternative devices are made of metal and include parallel channels, as the reference system. However, we vary the channel geometry, and remove the GDL. It is not longer the latter that serves as an interface with the catalyst layer, but a mesh made of stainless steel which will be described in Chapter 4. As the reference system, the new prototype just fits into the slot milled in the graphite structure and presented in Figure 2.4.

### 2.3.3 Additive manufacturing and channels with integrated GDL

In chapter 1 section 1.4 the AM is introduced. This method is used to manufacture as many channels as are needed. The manufactured part fits in the milled insertion area. Therefore, it is possible to compare new designs with old ones with same material. This is very important because different materials change the internal resistance of the FC. The new assembly is a versatile platform that houses old and new designs. However, AM technique imposes some constraints. Here the maximum manufacturable size by AM was considered, a system was selected. Since the materials are important for the performance of the cell Table 2.1 specifies the components of the reference system including GDL and their material properties. Experiment and simulation of reference system have the same boundary conditions.

	Material	Thickness
Membrane	Umicore pMembrain H300	25 $\mu\text{m}$
Electrode	Graphite with 0.4 $\text{mg}/\text{cm}^2$ platin	–
GDL	Carbon made from Freudenberg	206 $\mu\text{m}$
Sealing	PTFE	180 -200 $\mu\text{m}$
Milled composite plate	Composite (BMA5)	5.8 mm
Bipolar plate	BMA5 and stainless steel 1.4404	1mm
Current collector	Copper, gold plated	3 mm, 2 $\mu\text{m}$

Table 2.1: List of components, materials and their properties for reference system.

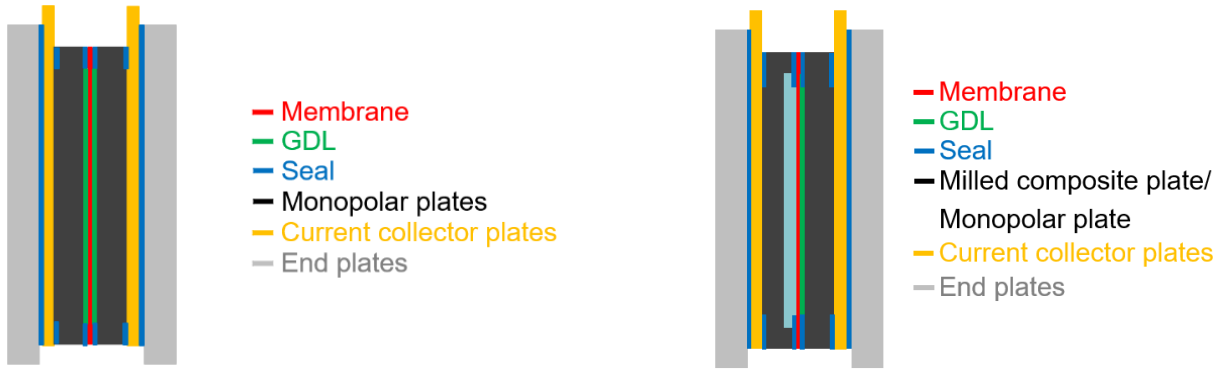


Figure 2.3: The standard assembly of the fuel cell (left), the reference fuel cell (right). The difference in these assembly is monopolar plate splits into milled composite plate which houses the monopolar plate. Moreover, removing the GDL is possible in new design.

In section 1.6 the maximum manufacturable size of the BPP with  $4 \times 4 \text{ cm}^2$  was mentioned the monopolar plate has the  $3 \times 3 \text{ cm}^2$  active surface area which comes to contact with membrane and the reaction happen in active surface area. The remaining 1 cm area is being used for sealing the active area from the surrounding by putting a sealing layer on it (Figure 2.4 right). Reference monopolar flow field which is commercially available consists of 11 parallel channels with 2 mm channel width.

## 2.4 Simulation of steady fuel cell operation in the case of reference system

Simulations approximate the steady fluid velocities, volume mass, concentrations, temperature and electric current densities satisfying the equations of section 2.2 . They will help us discussing in Chapter 4 fuel cell operation using various geometries of monopolar plate

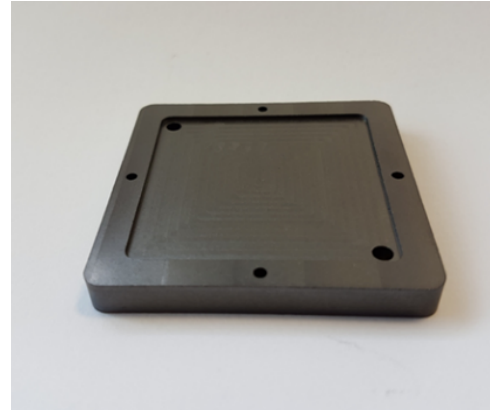
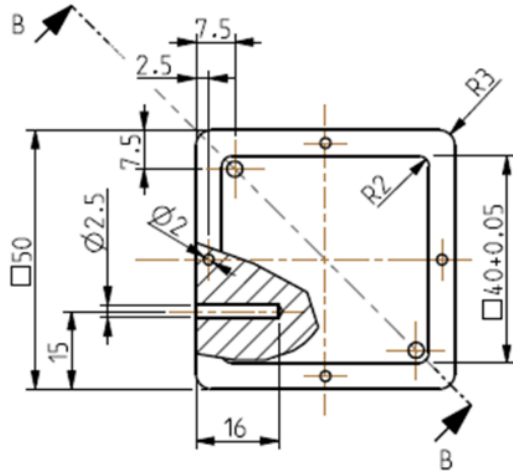


Figure 2.4: Dimensions of the milled composite plate (left). Anode side composite plate with milled insertion area made from BMA5 (right).

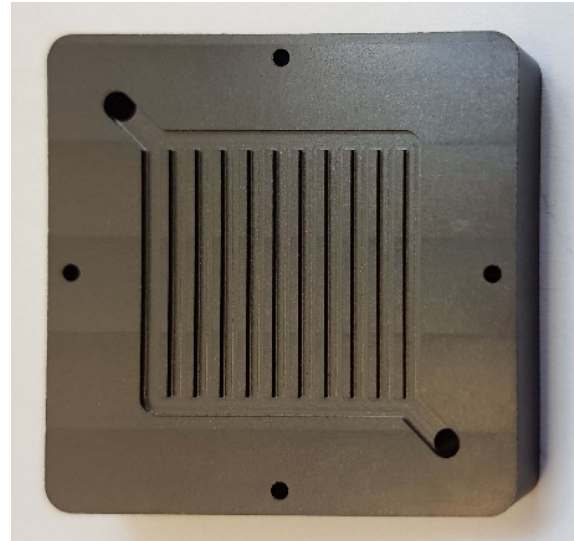


Figure 2.5: Same flow field for anode side monopolar plate, SLM manufactured (left), common standard composite flow field (right).

channels with integrated GDL. However, in the next section steady FC operation of reference system is the main focus.

### 2.4.1 Boundary conditions

In order to limit the system to study one must define boundary conditions. In order to be able to compare the simulation with experiment a set of parameters must be defined which are equal in both systems. In the section 4.4 the test rig in experiment is presented. Here are the boundary conditions provided which were used to perform the test in the test rig

Volume flow rate for 1.1 A cm <sup>-2</sup>	H <sub>2</sub>	1.7167e-06	m <sup>3</sup> s <sup>-1</sup>
	air	5.4667e-06	
Inlet/Outlet surface area		1.26e-05	m <sup>2</sup>
Membrane surface area		9e-04	
Velocity	anode	1.37e-01	m s <sup>-1</sup>
	cathode	4.35e-01	
Viscosity	anode	9.9e-6	kg m <sup>-1</sup> s <sup>-1</sup>
	cathode	2.08e-5	
Density	anode	0.706e-1	kg m <sup>-3</sup>
	cathode	1.029	
Temperature	anode	70.3	C°
	cathode	78	
Pressure	anode	1.6	bar
	cathode	1.5	

Table 2.2: Boundary conditions for PEMFC simulation and experiment.

using the composite part with insertion area in Figure 2.4. This test provides the polarization curve information, polarization curve provides key information about the fuel cell behavior in various conditions. In the test rig and the followed-up simulation. The boundary conditions for experiment and simulation are shown in Table 2.2.

### 2.4.2 Reference FC simulation

For simulation of the equations of Section 2.2 the author uses the finite volume method in COMSOL Multiphysics, the Batteries and Fuel Cells Module.

The flow field related variables such as pressure and velocity distribution in the parallel channels of the reference system are key components to predict the concentration distribution and the electric current delivered by the fuel cell. The uneven pressure distribution represented on Figure 2.6 results into the heterogeneous velocity profiles observed in the parallel channels according to Figure 2.7 on anode side as well as on cathode side.

The simulation uses finite volume method (FVM) to discretize the domain. The simulation predicts reactants concentration at various operating voltages. Figure 2.8 shows cathode water concentration maximum near the outlet, and hydrogen concentration maximum near the inlet.

Name	Value	Description
H_electrode	5e-5 m	Porous electrode thickness
H_membrane	1.8e-5 m	Membrane thickness
eps_gdl	0.4	GDL porosity
kappa_gdl	1.18e-11 $m^2$	GDL permeability
sigma_gdl	222 S/m	GDL electric conductivity
wH2_in	0.85	Inlet H2 mass fraction (anode)
wH2O_in	0.023	Inlet H2O mass fraction (cathode)
wO2_in	0.228	Inlet oxygen mass fraction (cathode)
U_in_anode	0.137 m/s	Anode inlet flow velocity
U_in_cathode	0.435 m/s	Cathode inlet flow velocity
mu_anode	9.9e-6 Pa·s	Anode viscosity
mu_cathode	2.08e-5 Pa·s	Cathode viscosity
MH2	0.002 kg/mol	Hydrogen molar mass
MN2	0.028 kg/mol	Nitrogen molar mass
MH2O	0.018 kg/mol	Water molar mass
MO2	0.032 kg/mol	Oxygen molar mass
T	343.15 K	Cell temperature
p_ref	1.01e5 Pa	Reference pressure
V_cell	0.935	Cell voltage
cO2_ref	40.88 $mol/m^3$	Oxygen reference concentration
cH2_ref	40.88 $mol/m^3$	Hydrogen reference concentration
kappa_cl	2.36e-12 $m^2$	Permeability (porous electrode)
sigma_m	6 S/m	Membrane conductivity

Table 2.3: Table of variable names used in the simulation of the reference PEMFC.

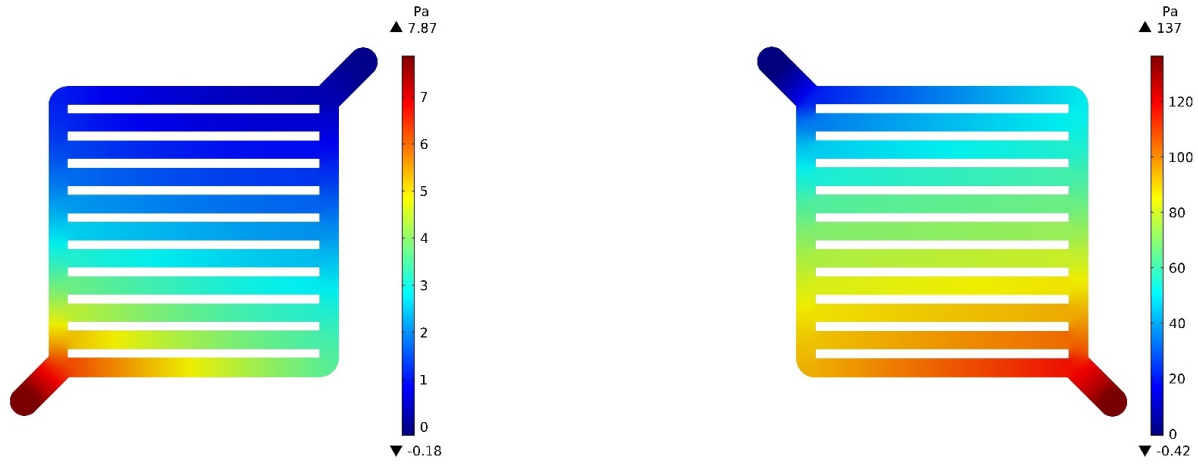


Figure 2.6: Pressure distribution in anode (left) and cathode (right).

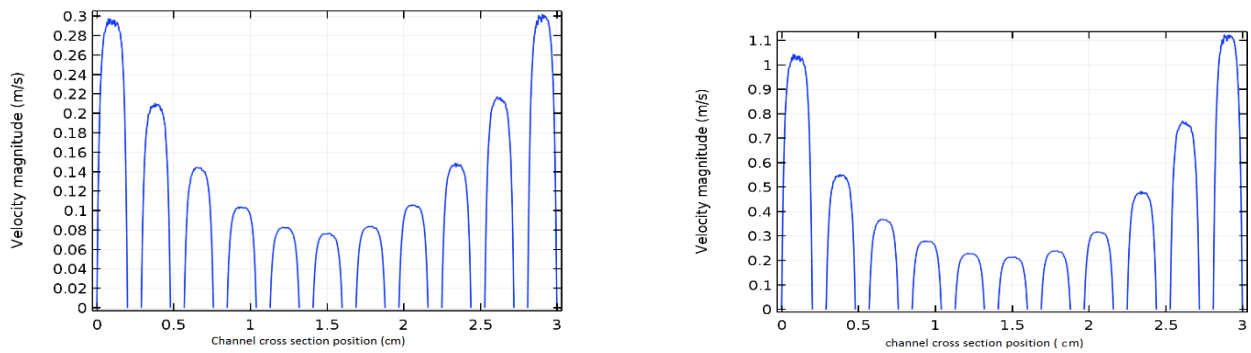


Figure 2.7: Velocity distribution in anode (left) and cathode (right).

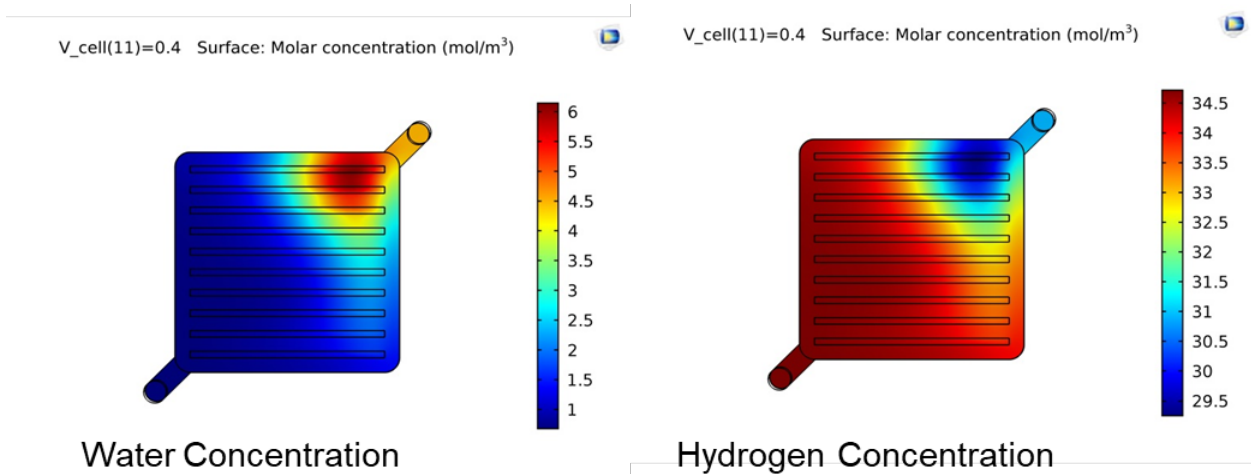


Figure 2.8: Anode side, water and hydrogen concentration distribution, voltage of the cell 0.4V.

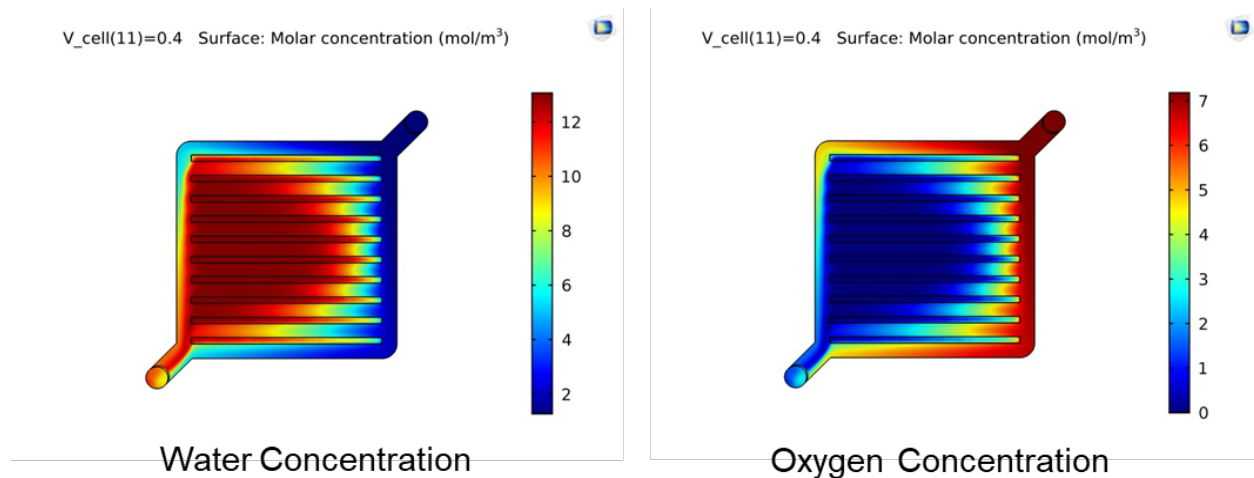


Figure 2.9: Cathode side, water and hydrogen concentration distribution, voltage of the cell 0.4V.

In addition, the simulation predicts the current distribution on the membrane. The Figure 2.10 specifies two points: 1) The model prediction in steady condition is reliable. 2) The concentration distribution influences directly the current density in the membrane. As it was described before inhomogeneous transport speeds up cell degradation and decreases lifetime performance. In specific subsets of the membrane the reaction starves due to low reactants concentration while water concentration peaks are observed elsewhere and can lead to channel blockage. Therefore, it is essential to improve the flow field for homogeneous flow distribution. Attempts to achieve more homogeneous flow are described in Chapter 4.

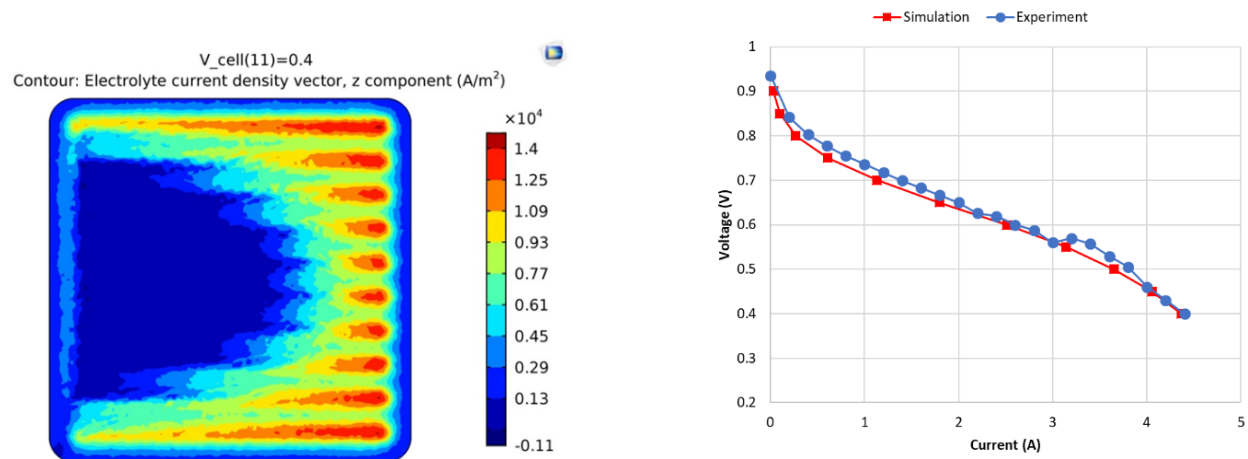


Figure 2.10: Current density distribution inside the membrane (left), polarization curve for simulation and experiment (right).

In the simulation the voltage is given. Then, for each given voltage, the current is calculated according to Equations 2.1–2.11 (last step of the simulation process). In the experiment, differently, the cell is attached to an adjustable load: increasing it decreases the voltage.

The experimental polarization curve exhibits a local voltage jump between 3 and 4 amps; it may be experimental error. The simulation returns slightly smaller voltage between 0 and 2, and is much closer to the experimental value above 2 amps. Note that the simulation does not only predict the flow field parameters, but also the concentration distribution in the channels and the current distribution in the membrane. Therefore, the author decided to use COMSOL to simulate fuel cell operation.

## 2.5 Refining thesis objectives and workplan

Equations 2.1–2.11 are implemented in COMSOL modules which describe fuel cell operation in steady conditions, assuming purely gaseous flows in BPP channels. Hence, we will use this model and this numerical tool to search for channel geometries that return pressure fields and velocities as uniform as possible in addition to checking that the electric production is sufficient. However, such approach does not help us preventing cathode water flooding or improving two phase fluid evolution. Therefore, an additional numerical approach of two-phase fluid flows evolution in channels is necessary, for water management, in addition to refined channel design. That approach is possible by a Lattice Boltzmann Method that separately studies two phase flows. We describe it and validate it in Chapter 3, using comparisons with experiment performed in collaboration with the University of Mannheim. Separately applying this method to two phase flows in parallel channels should help us detecting flooding or blockage. In Chapter 4 we investigate innovative designs of parallel channels, mainly using COMSOL and the model of Section 2.2. Chapter 5 is dedicated to two phase fluid flows in innovative channels, in this chapter the author studies the feasibility of integrating a special pattern to the parallel channels. Additionally, the LBM described and validated in Chapter 3, is compared with volume of fluid method (VOF). Lastly the numerical study is validated by comparing with an experiment performed by the author.

# Chapter 3

## Numerical method for two phase flow

### 3.1 Introduction

The fuel cell operation model described in sections 2.2 and 2.4 does not account for liquid water that may exist at the here considered operating temperatures. In this section we describe a tool that helped us studying the evolutionary two-phase flows that can occur in BPP channels. This tool is a Lattice Boltzmann method-based code which we used to solve three kinds of problems listed below.

1) Droplet generation In T-junction. Which is the topic of application of LBM code based on Rothman-Keller model for two phase flow in T-Junction section in this chapter. This is an extended version of published paper in journal of ChemEngineering which presents the simulation of droplet generation and influence of the flow rate for two immiscible fluids. This work focus on various flow forms in the T-junction, it compares qualitatively and experimentally the results with the LBM simulation.

2) Calculating the flow field in BPP. This application considers the homogeneous flow as the first priority in the design of the geometry. The application aim was to optimize the flow field inside the BPP. Hence, the author extended the 2D LBM code to couple the flow field with the structure. This code is an adjoint flow-structure coupling for LBM. The developed algorithm does change the geometry to achieve homogeneous distribution inside the domain. This application is the topic for the chapter 4.

3) Directional passive water transport in open micro channels. Focus of this application is to improve the water transport in a microstructure to transport the liquid water out of the BPP. It considers a microstructure that transports the water passively in a preferred direction. Before manufacturing the microstructure, this concept was tested using 2D LBM simulation and for more accuracy it was followed up by a 3D simulation. In both 2D and 3D LBM was compared to VOF model. Moreover, all of the simulations are validated by an experiment. This application is discussed in chapter 5.

In view of these applications in Section 3.2 we remind the principles of our LBM model and present how it calculates single and multiphase flow evolution. This provides an overview on the implementation of this method and defines parameters such as velocity, pressure,

or contact angle. Section 3.3 validates the two-dimensional variant by comparing problems designed for simulation against well-known analytical solutions. Final section 3.4 of this chapter validates the code by applying it to the specific microfluidics problem described in number 1 of the above list.

## 3.2 Lattice Boltzmann method for two phase flow

The LBM assumes phases composed of particles whose microscopic velocities  $e_0, \dots, e_N$  belong to a finite set of  $N+1$  vectors improperly named velocity lattice. In two (or three) - dimensional simulation  $N=8$  (or  $N=18$ ) and the velocity lattice is noted (D2Q9) or (D3Q19). At each time step the distribution of these velocities determines the particle positions on a discrete lattice that represents the flow domain. Interactions between phases are accounted by the collision operator that manages the distribution of the particle's velocity at the end of each time step. The simulations presented here are performed with the LBM using Rothman Keller model (RK) The LBM multiphase method in this study is based on publications of Liu and Leclaire et al. [34]–[36]. They have presented a detailed derivation of the model in their publication. The advantages of this method are the surface tension, viscosity and contact angle are independently adjustable. Moreover, this method separates the phases with a clear phase interface.

### 3.2.1 Basic principle and collision operator

Each phase  $k$  (for example, 1: *water*, 2: *heptane*) is described by a probability distribution function (PDF)  $f_i^k(x, t)$ , where index  $i$  represents the velocity vector  $e_i$ . Rothman and Keller (RK) [37] originally used the color ‘red’ or ‘blue’ (here water and heptane) to identify each phase ( $k$ ). Hence, this method is known as color model [38]. The total PDF is:

$$f_i(\mathbf{x}, t) = \sum_k f_i^k(\mathbf{x}, t) \quad (3.1)$$

The macroscopic properties are defined by the sum of all probabilities in all velocity vectors. As an example, the density  $\rho$  can be written as:

$$\rho = \sum_i \sum_k f_i^k \quad (3.2)$$

The macroscopic velocity  $v$  of the flow is calculated using density and average weight of discrete velocities:

$$v = \frac{1}{\rho} \sum_i \sum_k e_i f_i^k \quad (3.3)$$

$e_i$  for 2D (D2Q9) and 3D (D3Q19) is defined as:

$$\mathbf{e} = c \begin{pmatrix} 0 & 1 & 0 & -1 & 0 & 1 & -1 & 1 & -1 \\ 0 & 0 & 1 & 0 & -1 & 1 & 1 & -1 & -1 \end{pmatrix} \quad (3.4)$$

$$e = c \begin{pmatrix} 0 & 1 & -1 & 0 & 0 & 0 & 0 & 1 & -1 & 1 & -1 & 1 & -1 & 1 & -1 & 0 & 0 & 0 & 0 \\ 0 & 0 & 0 & 1 & -1 & 0 & 0 & 1 & -1 & -1 & 1 & 0 & 0 & 0 & 0 & 1 & -1 & 1 & -1 \\ 0 & 0 & 0 & 0 & 0 & 1 & -1 & 0 & 0 & 0 & 0 & 1 & -1 & -1 & 1 & 1 & -1 & -1 & 1 \end{pmatrix}$$

And the pressure  $p_k$  for the D2Q9 and D3Q19 is calculated using equation of state as:

$$\begin{aligned} p_k &= \rho_k (c_s^k)^2 = \frac{3}{5} \rho_k (1 - \alpha_k) \\ p_k &= \rho_k (c_s^k)^2 = \frac{1}{2} \rho_k (1 - \alpha_k) \end{aligned} \quad (3.5)$$

Where,  $c_s$  is the speed of sound and,  $\alpha_k$  is a free parameter to set the pressure level in the system. For more information about the parameters please refer to [39].

The LBM advances in time. There are three main steps in each iteration in RK model, streaming, collision and, recoloring. The evolution of the distribution function in time for each phase  $k$  can be expressed as:

$$f_i^k(\mathbf{x} + e_i \Delta t, t + \Delta t) = f_i^k(\mathbf{x}, t) + \Omega_i^{k,1}(f_i^k(\mathbf{x}, t)) \quad (3.6)$$

### 3.2.2 RK calculation process

The collision operator  $\Omega_i^k$  in equation 4 is calculated using three sub operators:

- 1) Single phase collision (SRT-BGK)

$$f_i^k(\mathbf{x}, t^*) = f_i^k(\mathbf{x}, t) + \Omega_i^{k,1}(f_i^k(\mathbf{x}, t)) \quad (3.7)$$

This equation is for the relaxation in the single-phase system. It assures that the system obeys the macroscopic values of the Navier-Stokes equations.

$$\Omega_i^{k,1} = -\frac{f_i^k(\mathbf{x}, t) - f_i^{k,eq}(\mathbf{x}, t)}{\tau_k} \quad (3.8)$$

Where  $\tau_k$  is the relaxation time of the collision process and,  $f_i^{k,eq}$  is the local equilibrium distribution of the fluid velocities. Relaxation time is related to kinematic viscosity  $\nu_k$  by:

$$\tau_k = \frac{3\nu_k}{c^2\Delta t} + 0.5 \quad (3.9)$$

In this project we use a single relaxation time for both phases. Density average of kinematic viscosity  $\bar{\nu}$  is defined as:

$$\bar{\nu} = \left( \sum_k \frac{\rho_k}{\rho\nu_k} \right)^{-1} \quad (3.10)$$

The local equilibrium function  $f_i^{k,eq}$  is determined by Maxwell-Boltzmann distribution.

$$f_i^{k,eq} = \rho \left( \phi_i^k + w_i \left[ 3 \frac{e_i \mathbf{v}}{c^2} + \frac{9}{2} \frac{(e_i \mathbf{v})^2}{c^4} - \frac{3}{2} \frac{\mathbf{v}^2}{c^2} \right] \right) \quad (3.11)$$

Where  $\phi_i^k$  adjust the compressibility of the fluid and  $w_i$  is weighting parameter for each node [39].

$$\phi_i^k = \begin{cases} \alpha_k & i = 0 \\ (1 - \alpha_k)/5 & i = 1 \dots 4 \\ (1 - \alpha_k)/20 & i = 5 \dots 8 \end{cases} \quad (3.12)$$

$$\phi_i^k = \begin{cases} \alpha_k & i = 0 \\ (1 - \alpha_k)/12 & i = 1 \dots 6 \\ (1 - \alpha_k)/24 & i = 7 \dots 18 \end{cases} \quad (3.13)$$

$$w_i = \begin{cases} 4/9 & i = 0 \\ 1/9 & i = 1 \dots 4 \\ 1/36 & i = 5 \dots 8 \end{cases} \quad (3.14)$$

$$w_i = \begin{cases} 1/3 & i = 0 \\ 1/18 & i = 1 \dots 6 \\ 1/36 & i = 7 \dots 18 \end{cases} \quad (3.15)$$

2) Two phase collision (Perturbation)

$$f_i^k(x, t^{**}) = f_i^k(x, t^*) + \Omega_i^{k,2} (f_i^k(x, t^*)) \quad (3.16)$$

Perturbation operator  $f_i^k(x, t^{**})$  introduces the surface tension in the model. To separate the phases a color-field  $\psi(x, t)$  can be defined:

$$\psi(\mathbf{x}, t) = \frac{\rho_{\mathbf{k}_1} - \rho_{\mathbf{k}_2}}{\rho_{\mathbf{k}_1} + \rho_{\mathbf{k}_2}} \quad (3.17)$$

Reis and Phillips [40] introduced:

$$\Omega_i^{k,2} (f_i^k(\mathbf{x}, t^*)) = \frac{A_k}{2} |\nabla\psi| \left[ w_i \frac{(e_i \nabla\psi)^2}{|\nabla\psi|^2} - B_i \right] \quad (3.18)$$

The interfacial properties adjusted by  $A_k$  and  $B_i$  can recover the Navier-Stokes equations.  $\nabla\psi$  is the color gradient in the water/heptane region.

3) Two-phase collision (Recoloring)

$$f_i^k(\mathbf{x}, t^{***}) = \Omega_i^{k,3} (f_i^k(\mathbf{x}, t^{**})) \quad (3.19)$$

This step is the characteristic of the RK model. The recoloring separates two fluids from each other. The R-K model significantly reduces spurious velocities compare to other methods [36].

$$\Omega_i^{k_1,3} (f_i^{k_1}(x, t^{**})) = \frac{\rho_{k_1}}{\rho} f_i + \beta \frac{\rho_{k_1} \rho_{k_2}}{\rho^2} \cos(\varphi_i) f_i^{\text{eq}} \Big|_{v=0} \quad (3.20)$$

$$\Omega_i^{k_2,3} (f_i^{k_2}(x, t^{**})) = \frac{\rho_{k_2}}{\rho} f_i + \beta \frac{\rho_{k_1} \rho_{k_2}}{\rho^2} \cos(\varphi_i) f_i^{\text{eq}} \Big|_{v=0} \quad (3.21)$$

where  $\varphi_i$  is the angle between the color gradient and the velocity vector.  $f_i$  and  $\varphi_i$  take values between 0 and 1.[38], [41]]

$$\cos(\varphi_i) = \frac{(e_i \nabla\psi)^2}{|e_i| |\nabla\psi|} \quad (3.22)$$

The operator allows the mixing at the interface between the phases. The interfacial thickness can be adjusted by  $\beta$  but the interfacial tension is determined by  $A_k$ .

4) Streaming

This step updates the particle distribution functions the new values are written to neighbor nodes. Then the boundary conditions can be applied. This completes a single iteration of the simulation and prepares the system for next iteration.

### 3.3 Implementation and validation in the 2D

In order to verify our model, we performed the Laplace test, static contact angle test, layered flow for two immiscible fluids test benchmark usually are applied to LBM method. Here we describe each test and its validation result.

#### 3.3.1 Laplace test

There is a force balance at the interface between the two phases. The change in interface form, result in the pressure difference between the fluids. Surface tension can be described using the Laplace law [42]:

$$\Delta p = \frac{\sigma}{r} \quad (3.23)$$

Where  $\sigma$  is the surface tension and  $\Delta p$  is the pressure difference. This equation represents the linear relationship between surface tension and curvature  $1/r$ . The surface tension can be estimated by simulating a series of drops with various radii. (see Figure 3.1)

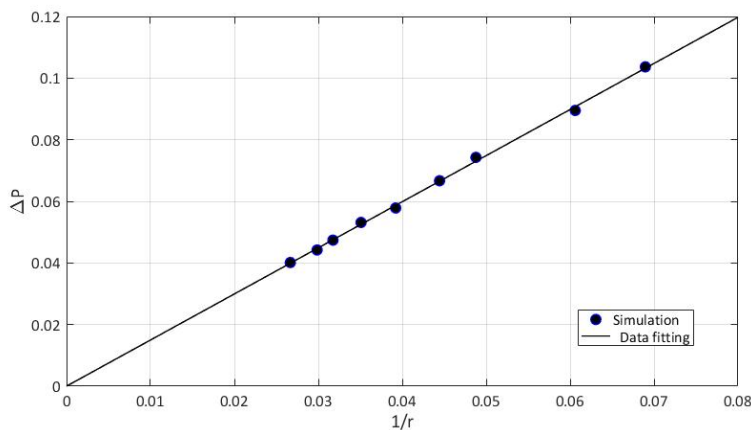


Figure 3.1: Change in pressure drop across the droplet surface with bubble radius, in simulation domain of 100x100 lattice unit (lu).

#### 3.3.2 Static contact angle

To validate the contact angle, it should be implemented in a capillary free model. Therefore, the system in Figure 3.2 (left) can be used to assign two contact angles for each surface. The model size is 32x200 lattice units (lu) and, in  $x$  direction, a periodic boundary condition was applied. Figure 3.2 was calculated using density  $\rho = 1$  and viscosity ( $\nu$ ) = 1/6. In each simulation a contact angle was assigned to top and bottom (for instance 85 and 95 degrees).

$$\sigma_{\text{red, blue}} \cdot \cos(\theta) = \sigma_{\text{blue, solid}} - \sigma_{\text{red, solid}} \quad (3.24)$$

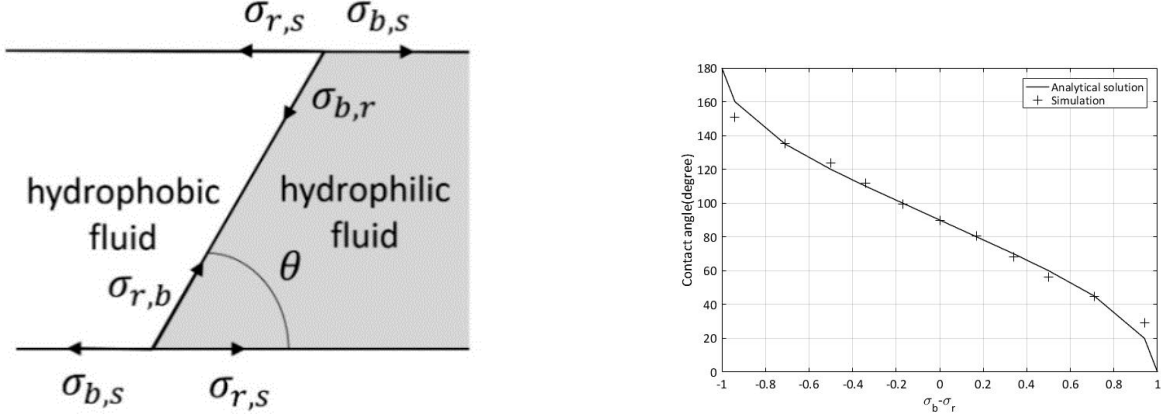


Figure 3.2: Force balance between the two fluids and the solid phase. In the LBM, the fluids are indicated as hydrophobic (index b) and hydrophilic (index r). Depending on the model parameters, the LBM can be used to simulate a contact angle between  $0^\circ$  and  $180^\circ$  (right).

### 3.3.3 Layered flow for immiscible two-phase flow

In the Laplace test, we verified the surface tension, and the fluid interaction with the surface was verified with the contact angle. These methods are mostly steady; however, the fluid behavior in T-junctions is dynamic. The last validation method verified the numerical method in a dynamic test. The analytical solution for the layered flow was calculated from the Navier-Stokes equation [43].

$$\begin{aligned} u_r &= \frac{dp}{dx} \left( \frac{1}{2\mu_r} y^2 + \frac{h(\mu_b - \mu_r)}{2\mu_r(\mu_b + \mu_r)} y - \frac{h^2}{\mu_b + \mu_r} \right) \\ u_b &= \frac{dp}{dx} \left( \frac{1}{2\mu_b} y^2 + \frac{h(\mu_b - \mu_r)}{2\mu_b(\mu_b + \mu_r)} y - \frac{h^2}{\mu_b + \mu_r} \right) \end{aligned} \quad (3.25)$$

Where  $\frac{dp}{dx}$  is the pressure gradient,  $h$  is channel radius,  $x$  is position in the channel,  $\mu_b$  and  $\mu_r$  are kinematic viscosity for red and blue phases.

We simulated the layered flow for a 40-lu channel as shown in Figure 3.3. The viscosity ratio was chosen as 1:5 at a Reynolds numbers of  $Re = 25$  with respect to the higher viscous fluid and for  $Re = 125$ . At the solid walls, the half-way bounce-back boundary was used to reproduce the non-slip boundary condition.

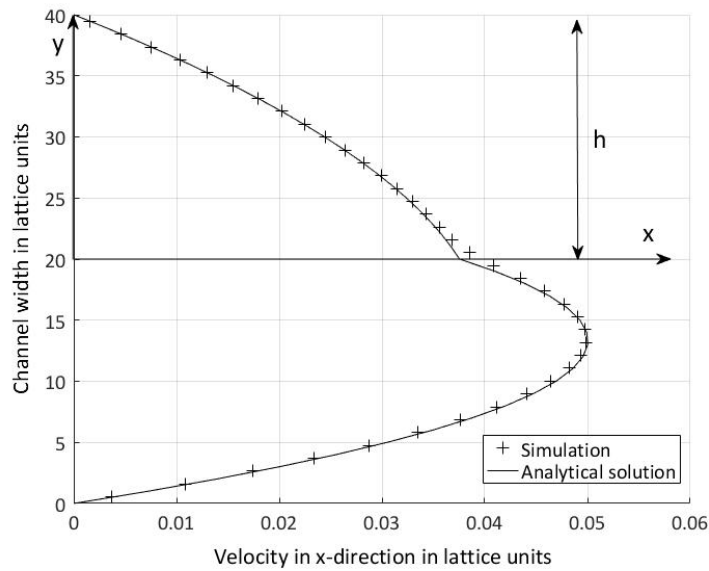


Figure 3.3: Velocity profile in two phase layered flow.

## 3.4 Application of LBM RK to two phase flow in T-Junction

### 3.4.1 T-junction as droplet generation system

In recent years microfluidics became an attractive field of research, since it has a wide range of applications such as Lab-on-a-chip devices, cosmetics, drug delivery, microfabrication, and chemical synthesis [44], [45]. In continuous-flow microfluidics, a droplet flow can be used to act as an isolated reactor with the minimum consumption of reagents [46], [47]. Therefore, the droplet formation for liquid/liquid or gas/liquid systems is important: in this study we concentrate our attention on droplet formation in a 1-mm channel geometry. In this range, droplet flow is successfully used in liquid/liquid systems for extraction [48]–[50] and synthesis of fine chemicals and pharmaceuticals [51]–[53]. In gas/liquid systems, applications include membrane fuel cells [54] and chemical synthesis [55]–[57]. For liquid-liquid extraction (LLE) processes, flow chemistry offers the benefit of excellent control over interfacial exchange parameters. In combination with chemical reactions in flow LLE can be integrated as in-line purification technique. Due to the combination of process steps, faster exchange of matter, and reduction in chemical consumption, LLE in microsystems leads to highly efficient processes [48]–[50]. For chemical synthesis, the short diffusion times for mass and heat transfer lead to a new field of process intensification which includes high temperatures, high pressures and high concentrations (solvent-free) to explosive conditions [51]–[53]. To achieve high productive microfluidic systems, a parallelization of the microchannel is crucial [58]. To build precise, uniform flow distributors a good knowledge of the droplet formation process

is necessary.

One of the simplest but most common methods to generate droplets is applying appropriate channel geometries [59]–[61]. The T-junction is the simplest microfluidic geometry for producing droplets. This study focuses on a specific configuration of the T-junction which is called head-on device [59], [62]. It consists of three channels that scatter a fluid (the dispersed phase) in an other one (the continuous phase), given that both are not miscible. In this device the dispersed phase (DP) and the continuous phase (CP) flow toward each other, as depicted in Figure 3.4. The dispersed phase should not wet the walls. Shear stress and pressure drop play an important role in droplet generation. The continuous phase creates a shear stress which detaches the dispersed phase and generates a droplet. Droplet length and frequency in T-junctions depend on various parameters such as flow rate, geometry, viscosity, surface tension, and contact angle. Over the last few years, numerous experimental and numerical studies aimed at determining the effect of each parameter on droplet formation. In the following sections, we discuss these parameters in detail.

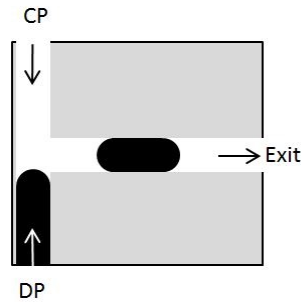


Figure 3.4: Head-on device geometry.

### 3.4.1.1 Geometry

Shi et al. [63] studied numerically the droplet formation in a T-junction using a lattice Boltzmann (LB) free-energy model. They concluded that the ratio of the main channel width to the lateral channel width of the T-junction plays an important role in the droplet formation. They found that the droplet length increases for a fixed capillary number with an increase in the ratio of dispersed to continuous phase inlet.

### 3.4.1.2 Contact angle

Shazia Bashir et al. [44] found that the surface properties of the main channel in T-junctions determine the droplet length. The contact angle describes the interaction between the fluid and the channel wall. The contact angle is the angle between channel wall and the interface between wetting and non-wetting fluid when these two meet the surfaces. They found that the droplet break-up time decreases as the contact angle increases from 120 to 180 degrees. Moreover, the fluid velocity in the microchannel increases with incrementing contact angle.

Finally, when the wetting property of the channel wall is hydrophilic, the advancing and receding contact angle changes [63].

### 3.4.1.3 Flow rate

Haihu Liu et al. [64] studied the influence of the flow rate ratio on droplet formation. They found in both simulation and experiment that the droplet diameter decreases gradually upon increasing the capillary number. They separated the capillary number using a critical value into large and small capillary numbers. Droplet size variation with increase in contact angle is higher in small capillary numbers; however, it decreases in high capillary numbers [64], [65]. Gupta et al. [66] found that the droplet volume grows when the dispersed flow rate increases. Moreover, a linear relationship between the droplet volume and flow rate for low capillary number was reported by De Menech et al. [65].

### 3.4.1.4 Viscosity

The viscosity of both the continuous phase and dispersed phase influences the droplet diameter. For a fixed continuous phase viscosity, an increase in the dispersed phase viscosity results in a decrease in droplet length [33]. Similarly, the droplet volume grows as the viscosity increases [66].

### 3.4.1.5 Surface tension

The droplet length increases for higher surface tension values and viscosity ratios of the fluids [44][33]. In this paper, we present the simulation result of the droplet formation in a head-on device using a two-phase LB method (LBM). We compare the numerical results to experimental data. The size of the microfluidic channels of our system is 1 mm to reach relatively high volumetric fluxes as used in chemical synthesis reactors. Thus, the lateral dimension of our microchannel is large compared to the majority of other publications in this field [67]. As a consequence, the capillary number of the flow regimes is smaller than  $10^{-5}$ , which is approximately two orders of magnitude smaller than other studies. Additionally, we use T-junctions made from poly (methyl methacrylate) (PMMA) and a water/heptane system which has no clear distinction between the dispersed and the continuous phases due to a contact angle of approximately 90 degrees. For this system, we show the influence of the volumetric flux on the droplet formation in the head-on device.

## 3.4.2 Simulation of two-phase flow in T-junction

### 3.4.2.1 Model implementation and hardware requirements

The described LB model was implemented in Matlab (version R2017a). The required memory was very moderate. Typically, a lattice of  $512 \times 512 = 262,144$  nodes requires about 20 Mb of random-access memory (RAM). The bottleneck of the transient simulations was given by the time steps. As pointed out in the previous section in Equation 3.9, the time step  $\Delta t$  is closely related to the parameters of the simulated fluids. (Therefore, the generation of one flow pattern, as shown in Section 5, takes several hours on a modern 3 GHz central processing unit (CPU). The exact values of CPU time depend on the chosen volumetric flux.)

### 3.4.2.2 T-Junction simulation

There are different methods to stimulate the flow in LBM. Velocity and pressure boundary conditions are two possible approaches. These boundary conditions operate by varying the densities at specified points. Another method is to initiate the flow by volume or external force. This method is convenient to implement especially in combination with periodic boundary conditions. In this study, all the mentioned boundary conditions were applied. In the following sections, we discuss each method in detail.

### 3.4.2.3 Velocity-pressure boundary conditions

The head-on device geometry is shown in Figure 3.5a. The velocity boundary condition was defined at the inlets, and the pressure boundary condition was defined at the outflow. These boundaries were implemented based on Sukop et al. [68]. Unfortunately, the application of these boundary conditions in LBM led to several problems. At first, reproducing the flow rates of the experiment at a Reynolds numbers of approximately 10 resulted in an unrealistically high-pressure gradient in the main channel. Consequently, the droplet size expanded gradually in the main channel. In addition, at low flow rates, these boundary conditions corresponded to a compressible behavior of the fluids. Finally, the velocity boundary condition did not satisfy the conservation of mass in the system, which was also reported in references [67], [69]. To overcome these drawbacks, we used a volume force in combination with periodic boundary conditions as explained below.



Figure 3.5: a) Standard geometry of the T-junction, b) modified geometry for periodic boundary conditions.

#### 3.4.2.4 Periodic boundary conditions and volume force

As mentioned before external or volume force is another method to initiate the flow field. The external force can be set for each fluid separately in the domain. We combined the volume force with periodic boundary conditions, which required a modified geometry as depicted in Figure 3.5b. As a result of the periodic boundary condition, we guaranteed the conservation of mass for both phases exactly [68].

As shown in Table 3.1, we wanted to simulate the same flow rate for both phases. This required a proportional integral (PI) controller. We placed sensors 1 and 2 close to the inlet and sensor 3 on the main channel. Sensors 1 and 2 controlled the flow for an equal flow rate simultaneously, while sensor 3 was used to maintain the defined flow rate in the main channel (Figure 3.6). The values of the sensors were constantly monitored. Based on these values, the controller changed the external force to achieve the desired flow rates.



Figure 3.6: Sensor positioning and the flow direction to adjust the flow rate.

#### 3.4.2.5 Flow conditions

Experimental validation of the T-junction. The simulation was performed on three different grid resolutions, i. e. a channel width of 10, 20, and 40 lu corresponding to a channel width of 1 mm. Additionally, we could match exactly the viscosity ratio of heptane/water with the experiment. There was a small difference between the contact angle in the simulation ( $80^\circ$ ) and the experiment ( $70^\circ$ ) in order to increase the numerical stability of the simulation. Moreover, we could perform stable simulations with a Reynolds number of 1–17, which was comparable to the range in the experiment. Finally, it was not possible to match the capillary number between experiment and simulation. This was due to the relatively large channel width. The simulation of capillary numbers down to  $10^{-5}$  would require a grid resolution one hundred times higher and was not feasible. Nevertheless, the simulation results show that the simulation and the experiment are comparable, since both two-phase systems were in a similar regime. All flow parameters for simulation and experiment can be found in Table 3.1.

#### 3.4.2.6 Computational efforts

The simulations were performed on an intel(R) Core(TM) i5-4590 CPU 3.3 GHz processor and 16 GB of Ram. The computational time varies depend on the grid resolution. For 10,

Parameter	Dimension	Simulation	Experiment
Channel width	(mm)	10, 20, 40 lu $\approx$ 1 mm	1
Viscosity ratio	(mm)	0.6839	0.6839
Density ratio	(mm)	1	1.468
Contact angle ( $\theta$ )	( $^{\circ}$ )	80	About 90
Flow rate ratio	(-)	1	1
Reynolds number (Re)	(-)	2–9	2–12
Capillary number (Ca)	(-)	$10^{-3}$ – $10^{-1}$	$10^{-5}$ – $10^{-4}$
Flow rate	(mL/min)	0.13–0.58	0.13–0.72

Table 3.1: T-Junction Boundary condition in simulation and experiment. The 1-mm channel was simulated using 10, 20, 40 lu channel sizes.

20, 40 lu each case took approximately 0.5, 4, 19 hours. Moreover, the time step size varies between  $1.6 \times 10^{-3}$  to  $1.0 \times 10^{-4}$  and the time step range (iteration) is from 1 to 5000-289000. All flow parameters for simulation and experiment can be found in Table 3.1.

### 3.4.3 Experimental validation of the T-junction

The experimental work performed in collaboration with Hochschule Mannheim. The flow experiments were carried out in a self-build micro structured head-on device made from poly (methyl methacrylate) (PMMA) (Figure 3.7). The design consisted of a square cross section of 1 x 1 mm which was manufactured by mechanical milling (MD24 CNC, GOLmatic Werkzeugmaschinen, Birkenau, Germany). The head-on device was cautiously bonded with a second PMMA plate (100 x 100 x 15 mm) using acetone. The second PMMA plate was made to be slightly thicker due to the fluid connections (1/4" - 28 UNF-Flat-Bottom port) for the inlet and outlet streams. The inlet and outlet streams were maintained with a 1/16" FEP capillary (Fluorinated ethylene propylene). The continuous feed stream of the liquid reactants was provided by a syringe pump (Pump 11 Elite, Harvard Apparatus, United States of America) equipped with two 25 mL glass syringes (ILS GmbH, Stützerbach, Germany). The outlet stream was collected in a headspace vial. For the determination of the two-phase flow characteristics, the liquid stream was imaged with a digital camera (model EOS 60D EF-S 15–85 mm, Canon, Osaka, Japan). The T-junction was illuminated with a light source (ACE Light Source, Polytec GmbH, Waldbronn, Germany) for improved visualization. The experimental set-up is displayed in Figure 3.7.

The droplet formation process was studied in a head-on-device with heptane (VWR, United States of America) which was used without further purification and deionized water. No surfactants were used in this study to stabilize the flow pattern. We used water and heptane since they have similar densities. The water in contact with PMMA was hydrophobic and the heptane was hydrophilic. The experiments were carried out at room temperature and

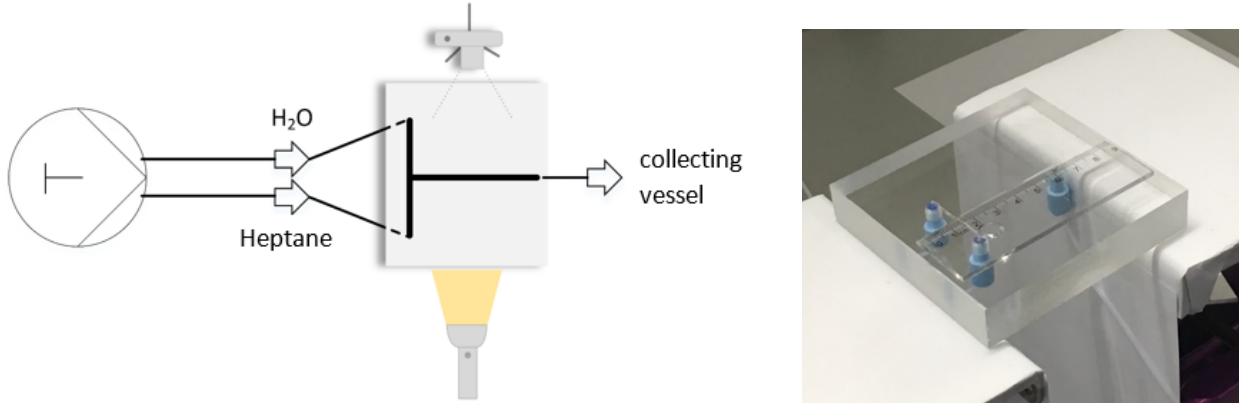


Figure 3.7: Experimental set-up for the flow experiments (left), and the head-on-device made from poly (methyl methacrylate) (PMMA) by mechanical milling (right).

atmospheric pressure. The operating parameters of the flow experiments including channel dimensions, flow rates, and characteristic dimensionless numbers are displayed in Table 3.1.

### 3.4.4 Droplet formation process

Thorsen et al [70] first introduced the droplet generation using T-Junctions and his work was followed by Shui et al. [71] in head-on devices. In our simulations and in the experiments, we observed five steps of droplet generation. This is depicted in Figure 3.8 as follows: (1) The disperse phase enters the junction; (2) it grows until the entire width of channel is filled; (3) the continues phase squeezes the disperse phase at the junction, (4) the disperse phase begins to break at the junction; (5) finally the droplet dispatches into the continuous phase. These steps correspond to the data published by Shui [71].

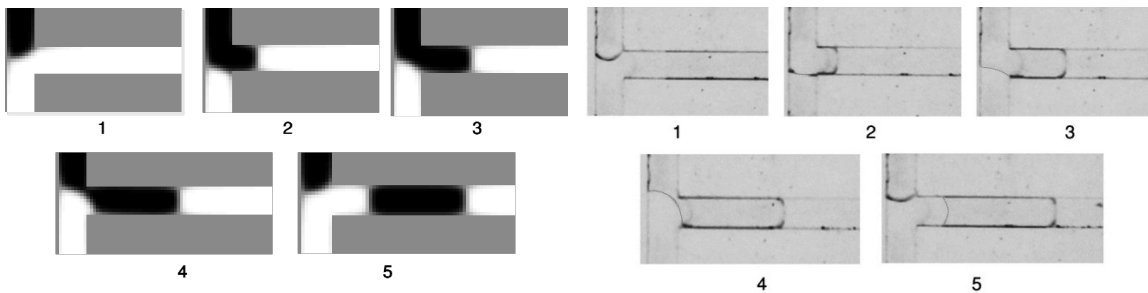


Figure 3.8: Five steps of droplet formation at the T- junction, the simulation is shown on the left (channel width 10 lu) and the experiment is shown on the right.

Additionally, Shui et al. [71] reported three different flow regimes at the outlet of the head-on device. In their publication, they called these flow regimes as follows: (I) dripping–squeezing, (II) jetting–shearing, and (III) threading. In this study, we were able to reproduce the three flow types using LBM. In the following sections, each flow form is discussed in detail.

- 1) Dripping-Squeezing: In this regime, the droplets are mostly homogeneous and equal (Figure 3.9). Here, the surface tension forces are greater than shear forces. The flow is stable, and droplets form rapidly. The homogeneous droplets have practical use in microfluidics, as these droplets act as individual reactors.



Figure 3.9: Simulation of squeezing regime for 40 lu.

- 2) Jetting-Shearing: this range initiates with transition from homogeneous droplets to varying droplet sizes. The increase in flow rate result in a new flow form. In this range the viscosity is dominant at the junction and, therefore, the tip of the disperse flow enters along continues phase in the main channel and form a parallel/layered flow (steps 1-3 in Figure 3.10). The surface tension force creates a round form at the tip of the flow (step 4). The tip advances prior to the wall surface. As it contacts the wall, the continues phase squeezes the disperse phase and a droplet detaches (step 5). The droplet generation cycle progresses and a continuous phase droplet form (step 6). At this point in simulation, this process ends as the main channel is filled with layered flow and droplets detach downstream. In the experiment, we observed that the flow changes its behavior in a cycle as follows: the droplets are generated rapidly with various sizes; afterward, the flow changes to layered flow and the cycle continues.

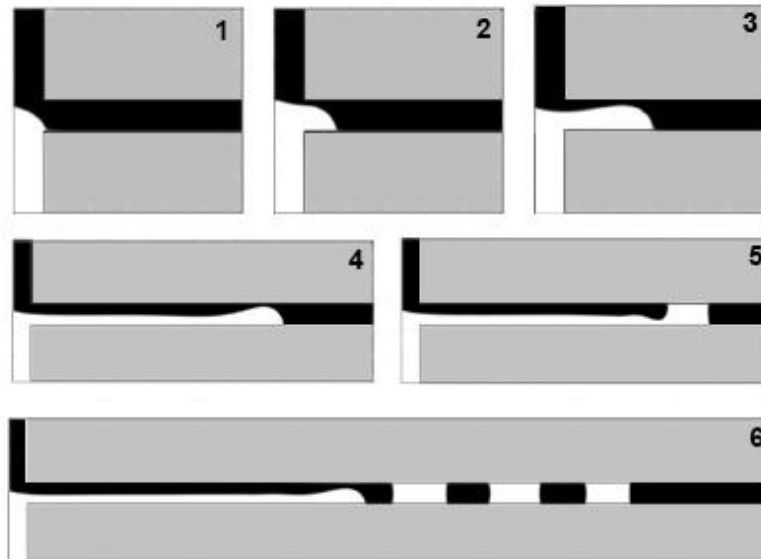


Figure 3.10: Droplet generation process in middle flow for 40 lu.

- 3) Threading: as the flow rate increases, the stable droplet flow turns into unstable flow with various droplet sizes. In the experiment the droplets are generated rapidly yet they are non-uniform. At this point, by increasing the flow rate the viscous forces are dominant with neither surface tension nor shear stresses existing. At higher flow rates pressure drop is eliminated at the junction; hence, the tip of the dispersed flow does not have the time to grow or block the channel and shape the layered flow [71]. However, in this regime, the droplets are generated downstream of the T-junction. We observed this phenomenon in the experiment and simulation, as depicted in Figure 3.8. The transient flow was also reported by References [64], [66], [71].

Experiment and simulation showed a transition between jetting-shearing and threading at comparable Reynolds numbers of  $Re > 9$  in the simulation and  $Re > 12$  in the experiment.

### 3.4.5 Mesh properties

The mesh independence study was performed on a uniform rectangular 2D grid. The optimal channel width was found in the 20 lu. Lower resolution lead to a less accurate interface and higher resolution create sharp interface with oscillations, that can be observed in the slug meniscus of Figure 3.11c. Moreover, higher resolution increases the computational time dramatically.

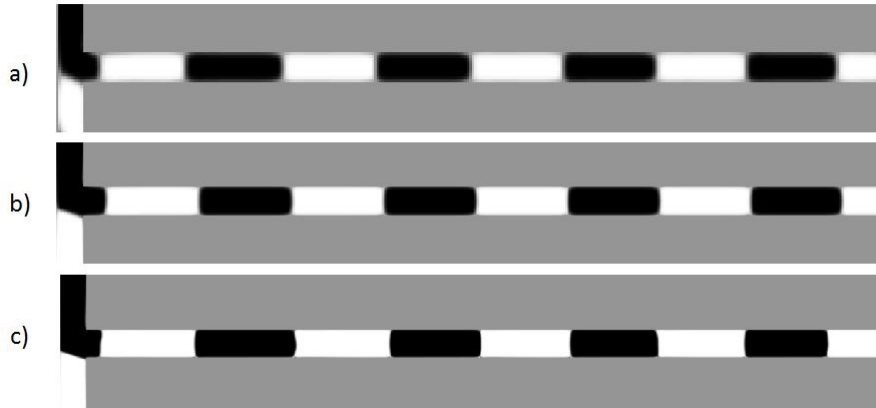


Figure 3.11: Influence of the resolution in the flow rate of 0.26 ml/min. The channel resolution is 10, 20 and 40 lu which correspond to 42600, 170400, 681600 domain grid points.

### 3.4.6 Discussion

In addition to the qualitative agreement between our LBM simulations and the flow experiments, we discuss here the size of the generated droplets as a quantitative measure. However, we must note that we are comparing two-dimensional (2D) simulations to three-dimensional (3D) experimental results. As one can see from Figure 3.12, the length of the droplets in the

experiments was more or less constant over the investigated range of flow rates. Additionally, the droplets of the continuous phase (water) were slightly larger than those of the dispersed phase (heptane). The LBM simulation results were comparable but showed some remarkable differences.

We performed a range of simulations to study the droplet diameter's relationship with the flow rate. In the simulations, a Reynolds number larger than nine led to the jetting-shearing regime, while, in the experiments, the droplet formation was stable up to a Reynolds number of approximately 12.

As seen in Figure 3.12, the droplet lengths between the simulations and experiments were comparable. Interestingly, both methods showed larger droplets for the continuous phase (water) and smaller ones for the dispersed phase (heptane). This was independent of the flow rate and, obviously, a result of the difference in the viscosity of both fluids. In the simulations, smaller flow rates corresponded to an increased variance in the droplet length. This variance was directly linked to our simulation approach where we used PI controllers to generate constant volumetric fluxes. Additionally, we saw a similar effect when we changed the lattice resolution, whereby we got larger variances in droplet length with higher resolution.

In summary, we found a good agreement between the simulations and the experimental data. To our belief, the observed differences were mainly an effect of the simulation being reduced to 2D and that the boundary conditions required the use of a PI controller.

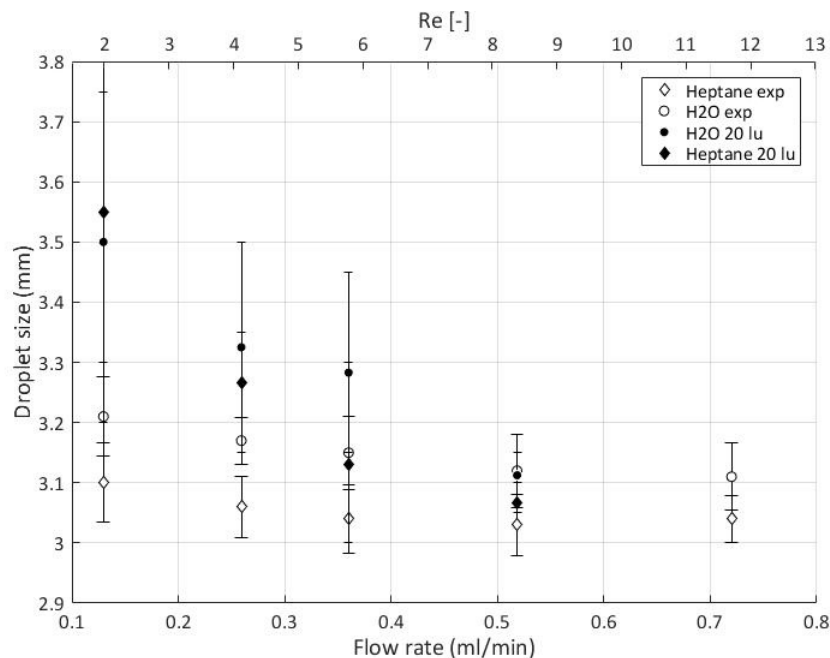


Figure 3.12: Flow rate relation with droplet size in simulation and experiment.

## 3.5 Chapter 3 summary

In this chapter, multi-phase LBM with RK model was used to simulate the head-on device with a channel width of 1 mm channel. Compared to other microfluidic devices, a channel width of 1 mm is relatively large, but is required for relevant volumetric fluxes in chemical synthesis reactors. The simulation on this scale was challenging due to the small capillary number of the flow regime. Additionally, we encountered several problems using pressure and velocity boundary conditions with the LBM which were already reported in other publications. We overcame these problems by forcing periodicity of the geometry and the use of a volume force. The volume force acted differently on both fluids and equal volumetric fluxes for both fluids were regulated by a PI controller.

Although the simulations were only performed in 2D, we could reproduce the three main flow regimes squeezing, dripping, and jetting. The transition between these regimes depended on the Reynolds numbers which were comparable between simulation and experiment. For the experiment, we used a self-built micro-structured head-on device with water and heptane as the continuous and dispersed phases, respectively.

We used the observed droplet length as a quantitative measure to compare our simulation results to the experiments. There was relatively good agreement between the simulation and the experiment regarding the length of the droplets, while the variance of the length in the simulation was rather large. The variance was caused by the PI controller. To our understanding, significant differences between the simulations and experiments were due to the comparison of 2D LBM results with 3D experimental data.

# Chapter 4

## From reference system to integrated BPP and GDL

### 4.1 Introduction

In section 1.2.3.4 the role and various BPP designs were described. Then, in Section 2.4.1 a set of operating parameters were introduced. Their values are specified in Table 2.2. These parameters set the boundary conditions of the flow domain of our simulation and experiment. The reference fuel cell and the numerical methods for the simulation of fuel cell operation have been detailed in the present chapter. Moreover, the focus will be on improving the equal distribution of flow in BPPs. Since the characteristic behavior of the flow depends on the gas properties such as viscosity, the anode and cathode are considered separately. In this chapter the focus is on the anode side. The new design modifies the flow field within limits imposed by manufacturing constraints.

In section 2.4.2 CFD simulation demonstrated already known inhomogeneous flow distribution of the flow field in BPP of standard design. In the present chapter the optimization of the flow field starts with one of the geometries which were introduced in BPPs for anode side. Then, the author has developed an extension code for LBM simulation to optimize the flow field. This extension code couples the geometry with the flow field. The program decide to modify the geometry based on the optimization parameters provided by user and the velocity or pressure parameters from two-dimensional flow field. This method has it challenges which will be described for 2D simulation. In Section 4.2.c.ii after presenting the challenges between the 2D and 3D design, the author proposes a solution to 2D optimization limit and tests proposed geometries by 3D flow field simulation in 4.3.3 section.

In the Section 1.2.3.4, the author presented various flow forms used in BPPs. He will demonstrate his findings in pin typed and parallel flow field. In this chapter the LBM code described in Chapter 3 is used to predict the flow field and propose new geometries with the help of an adjoint algorithm which designs the geometry according to conditions provided by user.

## 4.2 Anode side flow domain

Prior to the optimization the flow field parameters (velocity, pressure) should be calculated. Then the algorithm written by the author can adapt the geometry step wise to the flow field parameters. This capability is presented in next sections for the pin typed flow field and for parallel flow field. The author will describe extensively the advantages and disadvantages of each type and the 2D algorithm itself.

### 4.2.1 Pin typed flow field

LBM is very flexible when it comes to geometry. It is possible to change the flow field in a few iterations to achieve the ideal flow field. However, the predefined criterion that quantifies the deviation from the aim of the optimization plays a crucial role. Here optimization algorithm and the optimization sequence are demonstrated. This simulation aim is to achieve a homogeneous flow field to have equal distribution in a square surface. The algorithm first calculates the flow field until the steady state. In algorithm the domain is divided into 20x20 cells. Average of the monitored variable (which is velocity in this case) is written for each part of domain. In the next step it creates a map with average velocity of each blocks of the square shape domain. Figure 4.1 illustrates these two steps. Finally, this information will be used to change the geometry. Where the averaged velocity is high, more resistance will be introduced in the geometry by adding solid blocks (obstacles) to flow. Moreover, where average velocity is low, these solid blocks will be removed.

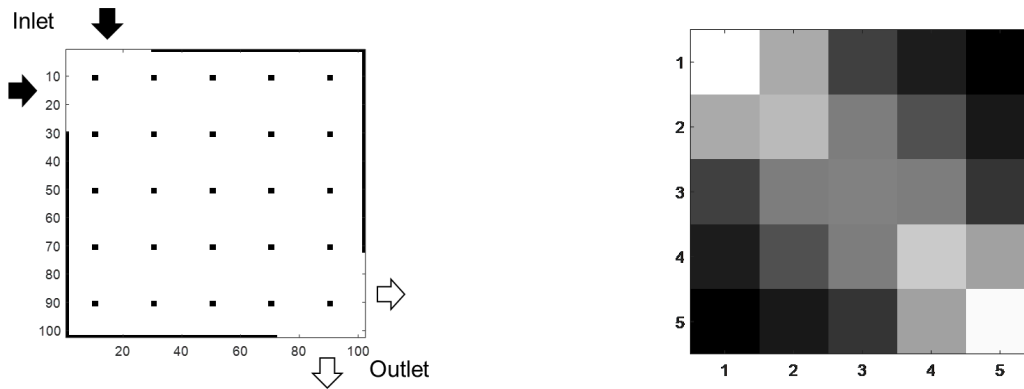


Figure 4.1: Pin typed initial geometry (left), velocity map, white represents high mean velocity and dark represents low mean velocity inside a 20x20 cell (right).

There are various possible methods to alter the domain based on the predefined criteria. Here two methods were implemented and tested. First method which can be used, in the pin typed domain is the changes can be done immediately to entire domain. This method does influence the geometry drastically in each iteration therefore, it was not used here. Second method is to, apply the changes sequentially for each zone (20x20 cell) in specific iterations. In this simulation the second method is used. Figure 4.2 represents the result of

the algorithm. In the regions with high mean velocity the geometry is dense (creates higher resistance to flow) and in the regions with lower mean velocity it is less dense to decrease the flow resistance.

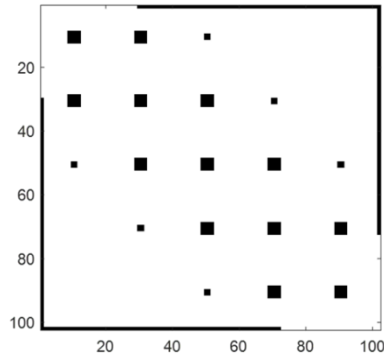


Figure 4.2: Optimized geometry introduces more resistance in the shortest path of reactant.

Flexibility and relatively easy implementation, highly adjustable with respect to the boundary are the advantages of this method. In contrast, the preconditions for geometry optimization can become complex since they can lead to unwanted changes in geometry. In this specific case the author run the simulation for various domain size and pin distribution to vary the porosity in the domain.

The pin typed geometry has a number of disadvantages for example: This structure should support the membrane therefore, if the pins are too small, they can pierce into membrane. Moreover, the structure does not offer enough contact to membrane for harvesting the electricity. It is possible to include various parameters such as the minimum thickness of the pin to perform the optimization to avoid having small pins that can pierce the membrane however, that will make the optimization more complex specially in third dimension. Considering the minimum and maximum size of the pins, the hazards of damaging the membrane, and LBM code limitation (single processor) the author did not continue the optimization of pin type structure.

## 4.2.2 Parallel flow field

The second candidate for optimization is the parallel flow field. The anode side parallel flow field should distribute the hydrogen on the catalyst layer and should have good contact to membrane to transport the electrons during the operation of the PEMFC. Hydrogen viscosity is about half of the air and it creates less pressure loss in small channels. Therefore, the anode can have more channels than the cathode.

Simultaneously to algorithm development and geometry optimization author made the first prototype. First prototype is a design for manufacturability (also known as design for manufacturing or DFM) study. In first prototype the author objective is to understand the

capabilities of SLM with important criteria which are required for an optimized flow field. One of such criteria is to increase the parallel channels from 11 to 60 channels in monopolar plate. This means the wall surface between the channels were shrunk to  $100\ \mu\text{m}$ . These parallel channels are located vertically behind the mesh in figures 4.3 and 4.16 right. Second criterion is integrating GDL into the parallel flow field. In the first prototype the active surface consists of a mesh superimposed on the parallel channels (Figure 4.5). The mesh on the surface of the parallel channel has two purposes: firstly, it improves the mechanical stability of individual walls, secondly it increases the channel to land ratio. Another objective of this work is to understand if this geometry provides enough mechanical stability or not. A detailed view of the mesh is demonstrated in Figure 4.3 Detail C. Third criterion is to design a support structure to close the top layer of the channels. The details of that geometry is shown from top view in Figure 4.3 in Detail F. It presents the rectangular shape with rounded corners structure in the middle which lies on the bottom of the channel (3D view the supporting geometry is in 4.6 right) and it rise up to the rectangular shape of the top layer. 0.5 cm frame size of the design is being used to place a  $200\ \mu\text{m}$  sealing. The manufacturing method of the first prototype is explained in section 1.6. The target is to understand the limits of this manufacturing method with respect to our application and to answer which kind of manufacturing challenges will be associated with first prototype, which is a flat thin complex geometry.

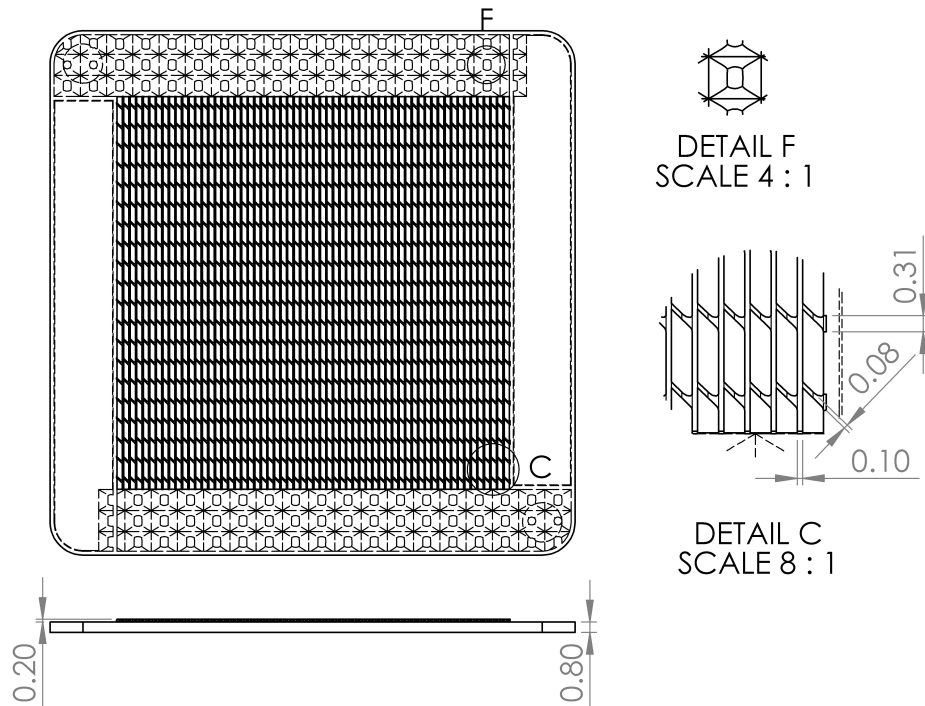


Figure 4.3: CAD drawing of first prototype. Inlet and outlet are visible on top left and bottom right. Notice the support geometry near inlet/outlet. "Detail F" displays a single support structure and "Detail C" displays mesh on the channels.

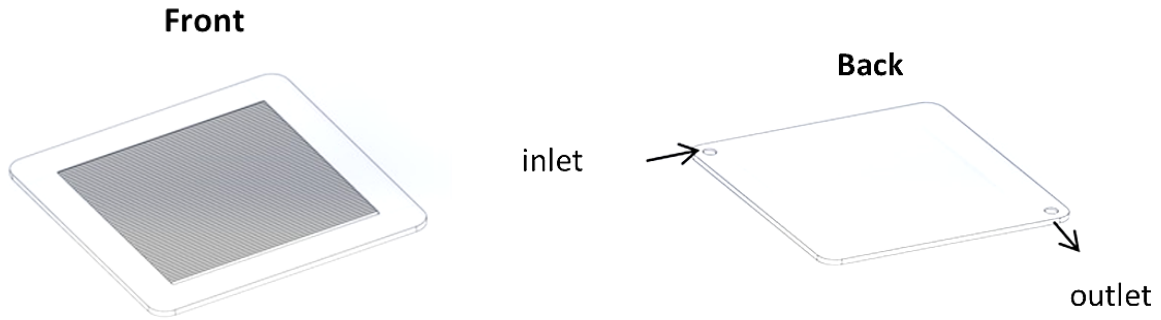


Figure 4.4: Front and back as well as inlet and outlet of the first prototype.

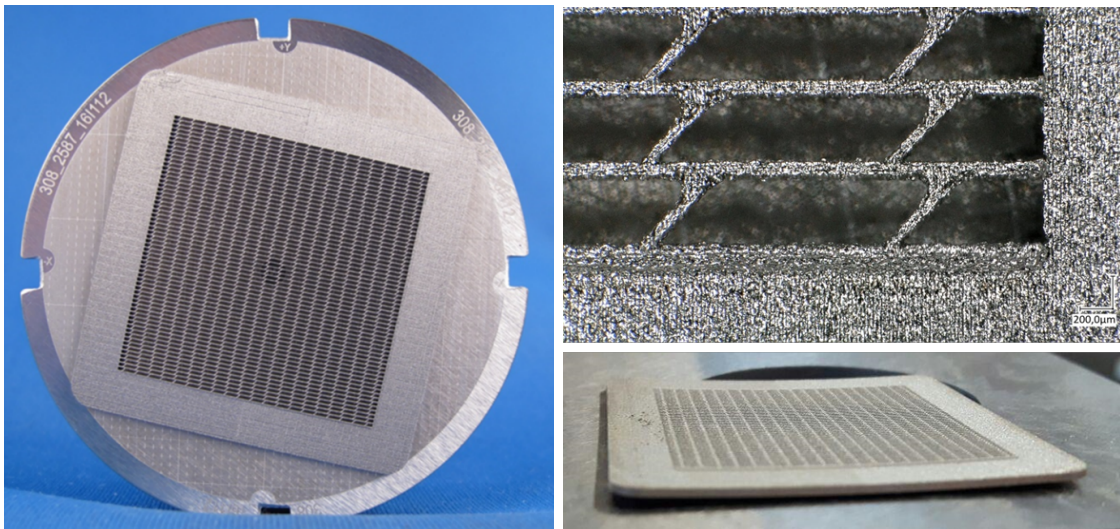


Figure 4.5: First prototype for anode side manufactured on the platform (left), mesh like structure on the parallel channels (right top), deformation caused by the internal stresses inside the 1.4404 stainless steel part (right bottom).

The design of this product had challenges because the author must consider various variables such as the minimum thickness possible to cut from the platform to have structural integrity and minimum thickness in the mesh in addition to specially made support structure to close the channels on the top. Moreover, electrical discharge machining (EDM) and Sinker EDM have been used to cut the product from the prototype platform and create inlet and outlet in the structure. In Figure 4.6 the inlet/outlet is shown under microscope. It was not possible to create this product using conventional additive manufacturing technique. Therefore, the sandwich build process was selected. In this method the platform which builds the back face is represented on Figure 4.6. It is integrated into the structure of the laser sintered powder. *A* and *B* present two parts of base platform and powder sintered material. After cleaning the component were sent to tempering to reduce the internal stresses in the manufactured part. Although tempering was performed to reduce internal stresses and by selecting the 1.4404 stainless steel in addition to adapting the design the product was slightly curved at the end. Since the product thickness is only 1 mm by applying slight force (during tightening the

screws in assembly) we could test this part inside the fuel cell. As it was mentioned before another challenge was to build the supporting structure to close the 0.5 cm wide frame surface on the front side. The inlet and the outlet were removed from the structure by sinker EDM. For better visualization the CAD design of the product is on the right side before EDM. The supporting structure has four sides and in design the author tried to decrease the lower contact surface to as small as possible while covering the maximum surface possible on the top. This was challenging because the support structure had only 0.3 mm height.

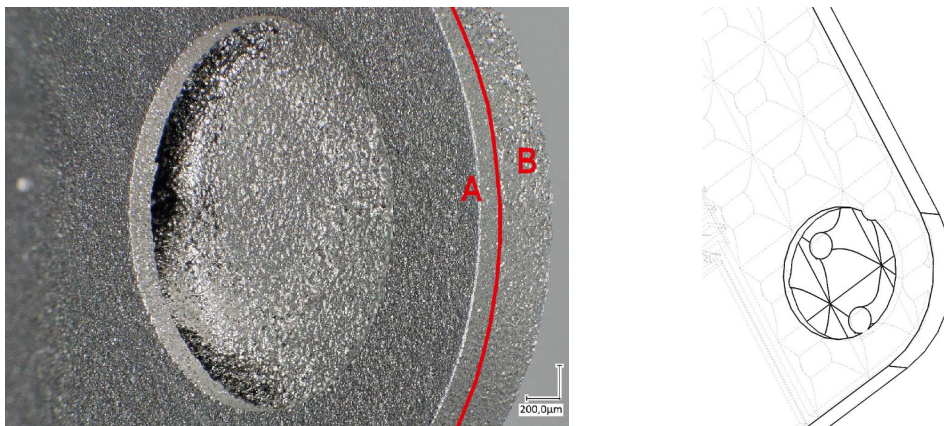


Figure 4.6: First prototype contains two components: *A* side which is the material from the base platform and *B* powder sintered material which was added to the top layer (left), CAD design of the supporting structure (right). It present the support geometry prior its removal by sinker EDM.

### 4.3 Parallel flow field optimization

The parallel flow field of the reference system has been described in Chapter 2, where the fluid flow in the monopolar plate has been studied as well. The flow field of the first prototype is the focus of this chapter. The first prototype consists of 60 parallel channels which are separated by walls with thickness of  $100 \mu\text{m}$ . Here the author investigates the flow field in first prototype and tries to optimize the flow field in order to achieve homogeneous reactant distribution on the membrane. To achieve this target LBM method a self-developed algorithm to optimizes the geometry based on the flow field are used.

At the time of manufacturing the first prototype the author dedicated the time to calculate the flow field of the structure using 2D LBM. Figure 4.7 displays the average velocity (right panel) in each channel of the first prototype (left panel). Here specific simplifications are required to employ the existing code. For example, the inlet and the outlet in the simulation are necessarily different from the actual first prototype which has the third dimension. Moreover, the domain is limited to  $1100 \times 1000$  cells. The pyramid shaped supporting structure in simulation is represented by the blue rectangular structure. The 3D pyramid shape is shown in Figure 4.6 right and 2D shape is in detail F of Figure 4.3. This supporting structure

influences the flow of reactant in the channels and create resistance in flow. This leads to inhomogeneous distribution in the channels. On the other hand this structure is necessary to close the top layer because this component is built layer by layer and in order to build a new layer there must be a support structure underneath it. On the top of the closed channels sealing will be placed in the assembly as it was described in section 4.2.2.

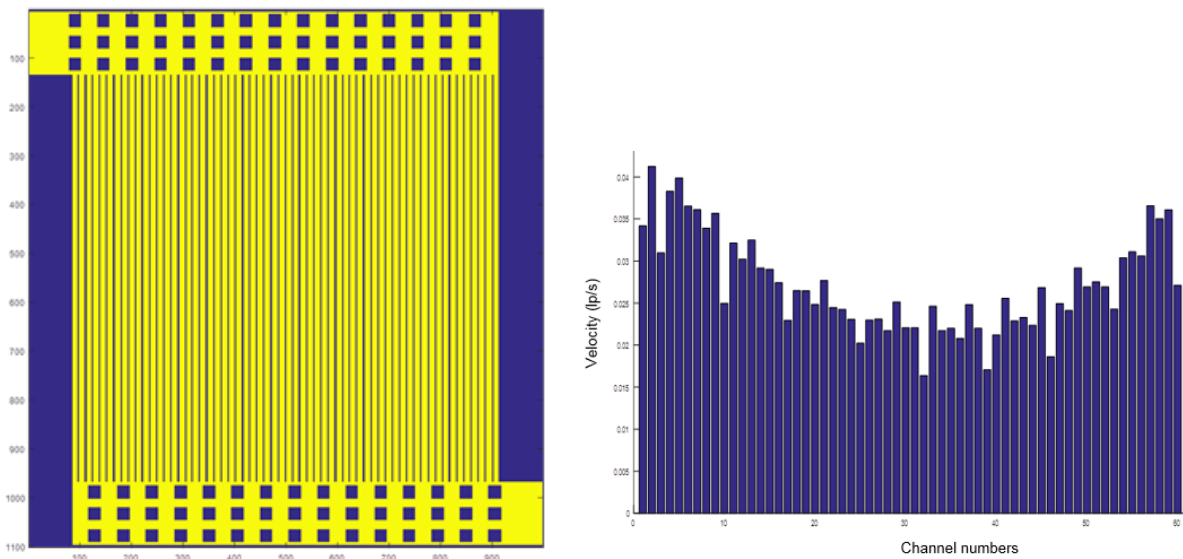


Figure 4.7: Slice from the first prototype, flow field is yellow and solid walls are in blue (left), average velocity in each channel computed by LBM (right).

The 2D Simulation of steady gas flows is obtained with an existing evolutionary LBM code. Running it in the channels of the first prototype returns an unequal flow rate distribution (Figure 4.7 right). This is due to the pressure loss in the inlet and the outlet channels.

We used the simulation to find better geometry, i.e. changing the thickness of the walls along the channels. To this end, we inserted the steady flow simulation in an algorithm that uses it to determine the flow rates  $\dot{v}$  in any considered set of channels. Hence, the algorithm quantifies the degree of non-uniformity of the channel flows by computing the deviation between the maximum and minimum volume flow rate, a quantity that plays the role of an objective function. The algorithm uses this information to automatically modify channel widths so as to decrease non-uniformity. The procedure block diagram of the algorithm is depicted in Figure 4.8. The algorithm stops when the objective function is smaller than a prescribed quantity. The block diagram functions as following. First step calculates the primary values in steady state, second step calculate the flow rate in each channel based on velocity and the channel width, third step check if the difference between maximum and minimum flow rate is above or below the given value. If it is below then the solution is converged and will be terminated if not it will go to fourth step. Based on the value of  $\Delta Q$  the channel wall thickness increases accordingly the channel length. If the value is maximum compared to the predefined constant value for optimization total length of the channel will be thickened, whereas if the deviation is half of the predefined constant value half of the length of the channel will be thicken. After some iterations a new value determine if the

optimization was enough or another channel still has high flow rate compare to the minimum flow rate in the channels.

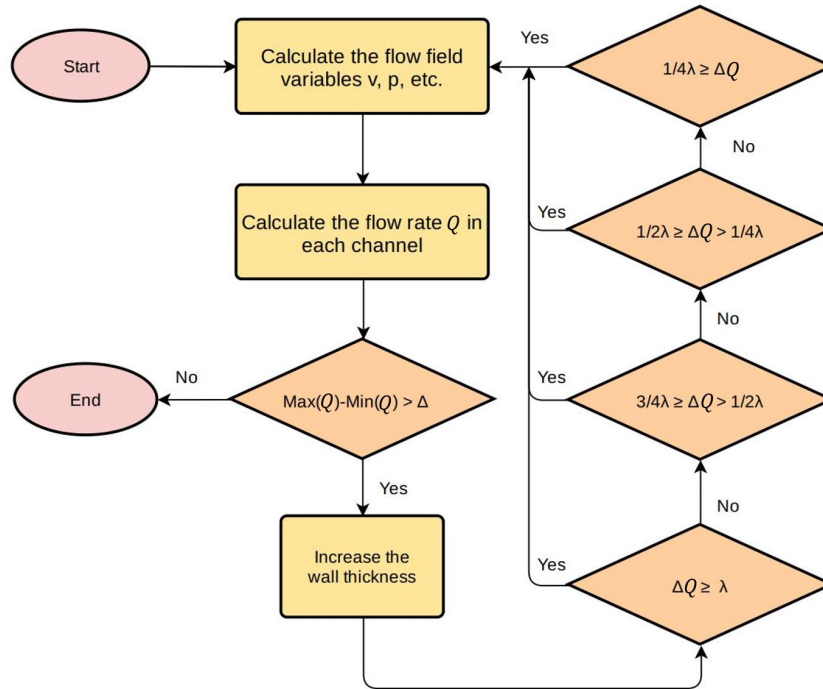


Figure 4.8: Algorithm to change individual channel width.

The algorithm changed the initial geometry Figure 4.7 to 4.10 left. The algorithm reduced the channel width near inlet and outlet and maintained the original channel width in the middle as in Figure 4.9. In the Figure 4.10 right the volume flow rate is shown there still exists some deviation between the channels. These deviations can be reduced if the grid resolution is higher. This resolution was at the edge of the balance between the maximum achievable accuracy and the performance. Although, the 2D LBM simulation works for the first study it has some limitations. The code is not designed for parallel processing. Therefore, the grid resolution limits the accuracy directly. As the result, the author made the decision to validate the result using COMSOL. It is a well-known conventional CFD program and it is capable of parallel processing.

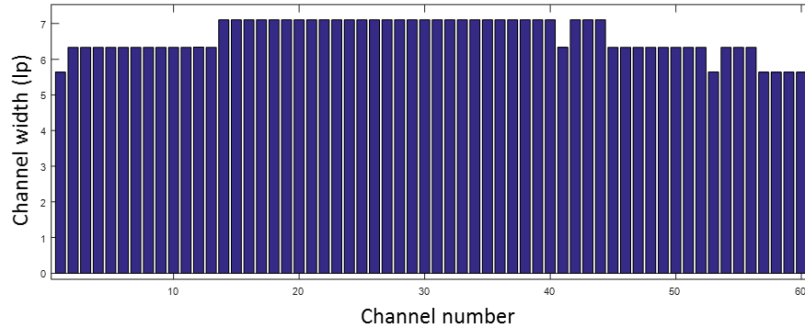


Figure 4.9: Channel width distribution in the channels.

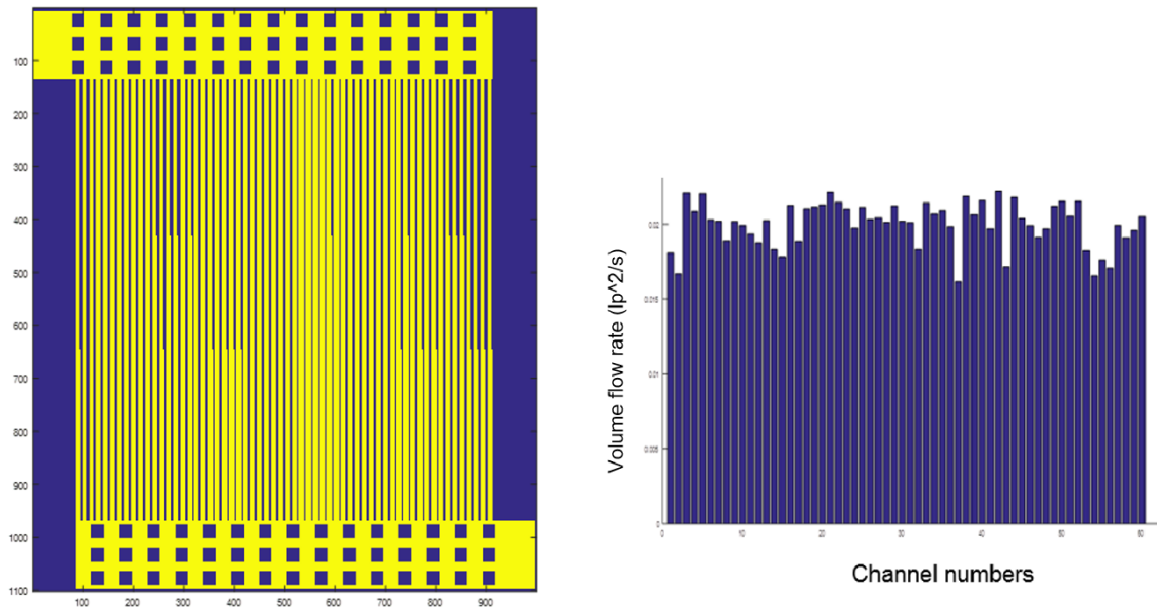


Figure 4.10: The optimized channels (left), the algorithm has thickened the walls differently to reduce the flow rate locally. Volume flow rates in each channel (right).

### 4.3.1 2D LBM comparison with COMSOL

Due to the limits of the LBM code which was used in the institute, parallel processing was not possible. Therefore, in order to proof the results are not mesh dependent a comparison between the 2D LBM simulation and COMSOL was performed. This has important role on the accuracy of the optimization algorithm in LBM. The geometry presented in Figure 4.7 has a velocity distribution shown in Figure 4.11 in 2D simulation. 1 million grid points in the LBM compared to 2.5 million cells in COMSOL present that LBM requires higher cell numbers to capture the flow field velocity distribution. This resulted in jumps instead of small deviation visible in COMSOL simulation.

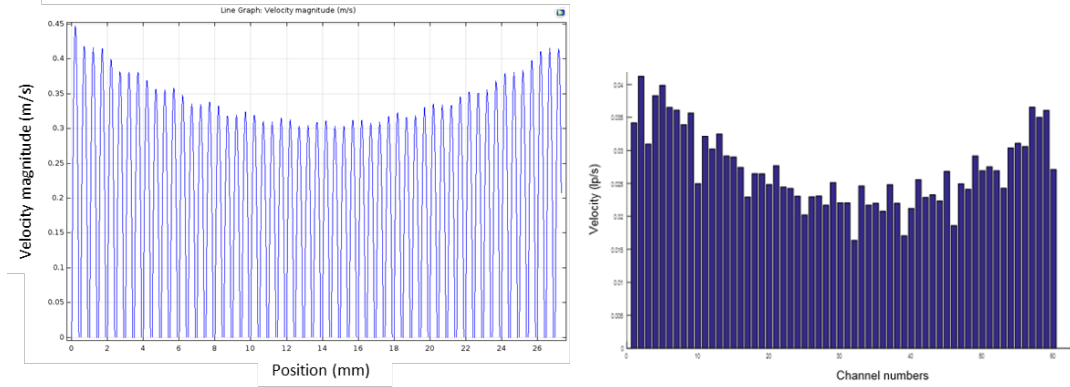


Figure 4.11: 2D simulation of initial geometry with COMSOL left and with LBM right.

In the last paragraph the first prototype was simulated in two separate methods (LBM and commercial software COMSOL) to evaluate the influence of the mesh on results. The second comparison is between the optimized channels in 2D using COMSOL and LBM. The optimized geometry is shown in Figure 4.10 left. The COMSOL and LBM simulations consist of 2 million cells and 1 million grid points accordingly. Again the influence of the grid points in optimization are clear. Therefore, the parallel calculation capability is essential for geometry optimization. In this part 2D LBM simulation was compared to COMSOL, the difference between two methods was number of cells and parallel processing capability. Now how does this difference influence same simulation in the 3D flow field.

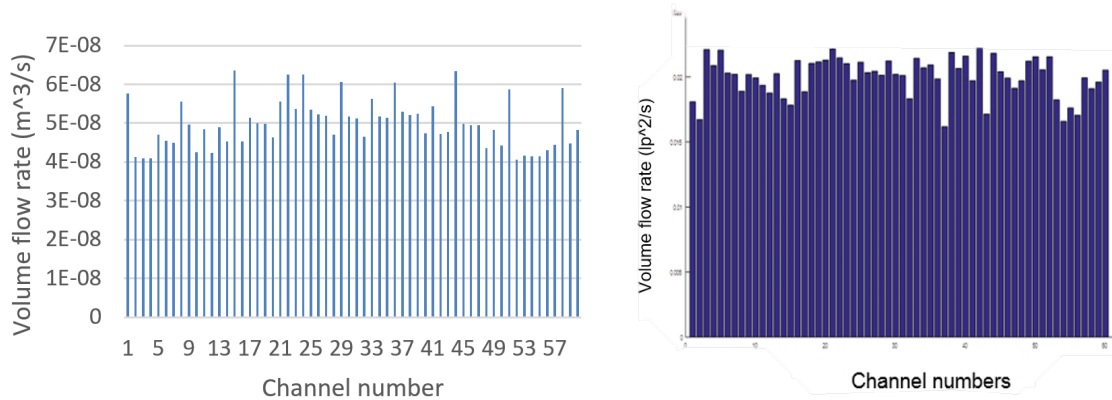


Figure 4.12: 2D simulation of optimized geometry, COMSOL (left) and with LBM (right).

### 4.3.2 2D and 3D comparison with COMSOL

It is common to simplify the problem by reducing the dimension of the problem from 3D to 2D or cleaning the geometry to calculate the solution efficiently. However, the simplification must not have a major impact on the solution. Hence, the author made a 3D geometry deduced from the optimized flow field shown in Figure 4.10 left then performed a 3D simulation with optimized shaped. 2D and 3D simulation for optimized shape were performed

with COMSOL to evaluate if the flow distribution differs. They return different results, more specifically parabolic distribution in the 3D simulation which is similar to the initial flow field before optimization. In the 2D simulation the third dimension is always considered as infinitely long. However, this simplification is true in many applications which the third dimension is considerably larger compare to the other dimensions. In the 2D simulation the third dimension is considered as infinitely large compared to channel width but the channel depth here is 0.8 mm which cannot be considered large compared to length of the channel (30 mm) and width of the channel (0.4 mm). Therefore, the 2D optimization is not sufficient to design a 3D product when the third dimension is small compared to channel width.

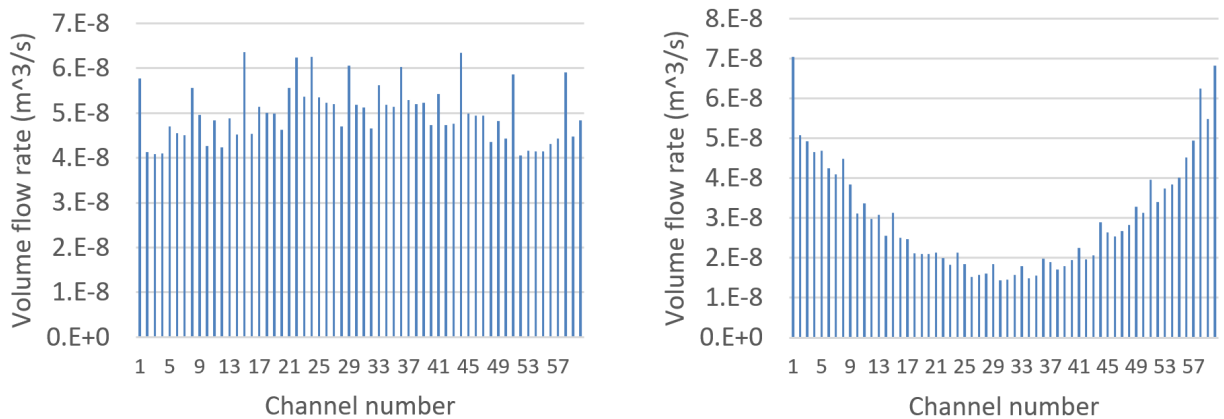


Figure 4.13: 2D (left) comparison to 3D (right) simulation for optimized geometry with COMSOL.

The above results prove that a 3D design with respect to the flow conditions is necessary. Therefore, the author designed logical pathways to eliminate the inhomogeneous flow distribution and verified them using 3D simulation using COMSOL. The work here can be followed up by a 3D LBM simulation capable of parallel multi-processor computing.

### 4.3.3 Three-dimensional flow field

The logic of the 3D flow field design idea lies on two important aspects. First aspect is homogeneous flow field using repetitive structure and second is manufacturability. In this section the author attempts to minimize the pressure difference in the channels by introducing channel grouping. Channel grouping connects a group of channels together near the inlet or outlet area. The channels on the active area remain identical. By grouping the channels, the total traveled distance for the gas is nearly identical for each group of channels and the gas cannot travel the shortest path compared to first prototype. The second aspect is to focus on a design manufacturability by the AM. As it was mentioned before maximum manufacturing size is 4x4 cm with 3x3 cm active surface which is equal to the size of the membrane.

In the fluid dynamics the flow always takes the shortest path to confront the least resistance. In the CFD simulations the author understood the structure outside the active surfaces region influences strongly the flow field in the channels inside the active surface region.

Therefore, the new design must focus on channels near inlet/outlet to improve uniform distribution of reactant in flow field. Therefore, two designs were proposed here to increase the homogeneity of flow distribution with respect to limits in manufacturability. These designs are called "sloped parallel flow" and "cross-flow field". Each six channels are packed together to exhibit the nearly identical total traveled distance; hence they present similar pressure drop. Figure 4.14 shows the two new designs and the first prototype. In addition, the grouping provides the necessary support to build the top surface on the support structure outside active region. A graphical demonstration of the support structure is given in Figure 4.3 and 4.5, As it is shown top layer of the inlet and outlet channels are closed to avoid leakage and placement of the sealing outside the active region. The principles of the two new designs are detailed below.

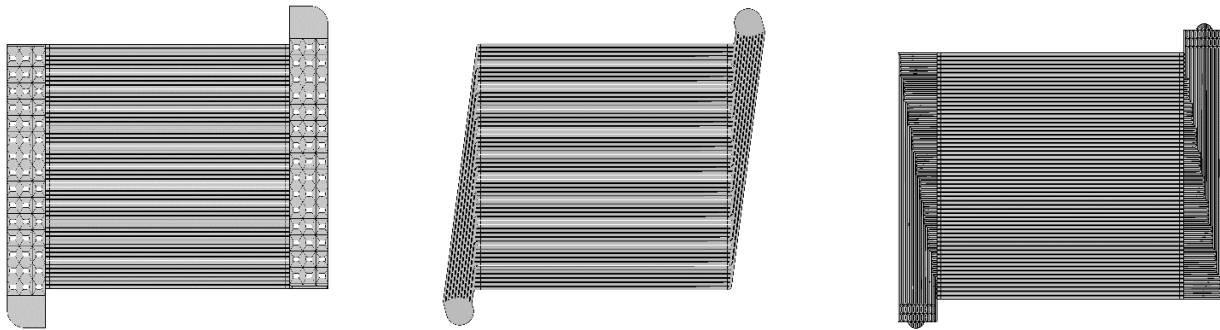


Figure 4.14: Proposed 3D flow field geometries for AM, from left to right, first prototype, sloped parallel flow field, and cross-flow field.

Sloped parallel flow field has inclined channels. This design reduces the length of the channels to minimum. The cross-flow field has 90 degree edges and all of the channels have arcs these arcs should provide the support structure for the top layer. A view from bottom side of the structure is provided in Figure 4.15 right.

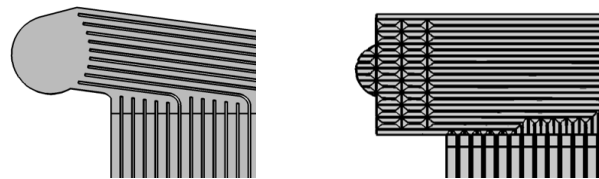


Figure 4.15: channel grouping in the inlet area for sloped parallel flow field (left). Cross parallel flow field (right) this geometry has an small arcs inside the channels to create the support structure for the top layer of the channel.

#### 4.3.4 Parallel flow field CFD simulation

The flow field is simulated for all the above structures. Flow distribution in the first prototype in Figure 4.17 presents high velocity near the inlet and outlet channels, the middle channels has the lowest velocity. All the channels have equal width. The difference between

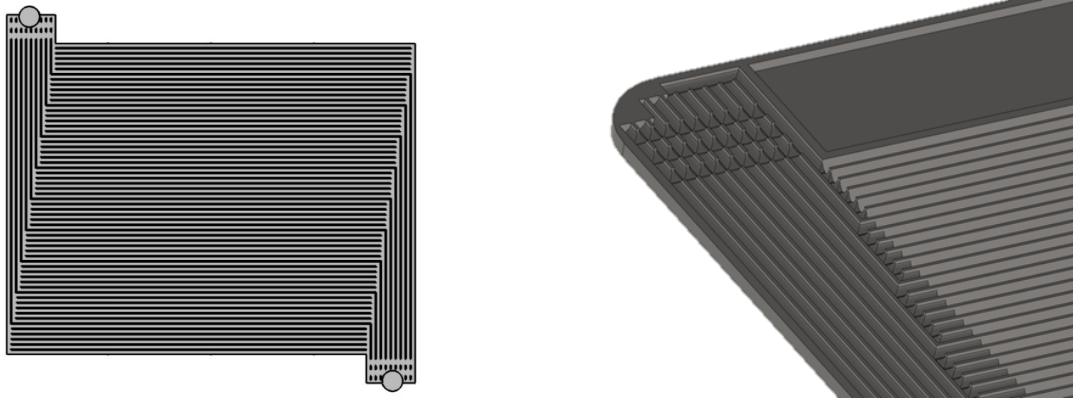


Figure 4.16: Flow field inside the cross-flow field structures, bottom view (left), inlet/outlet supporting structure (right).

the low and highest velocity is 88%. In comparison the reference cell has 73% difference between highest and lowest velocity. Here the objective was to prepare the first structure with stainless steel and understanding limits of SLM and stainless steel material. More information regarding the experiment of the manufactured part is presented in section 4.4.

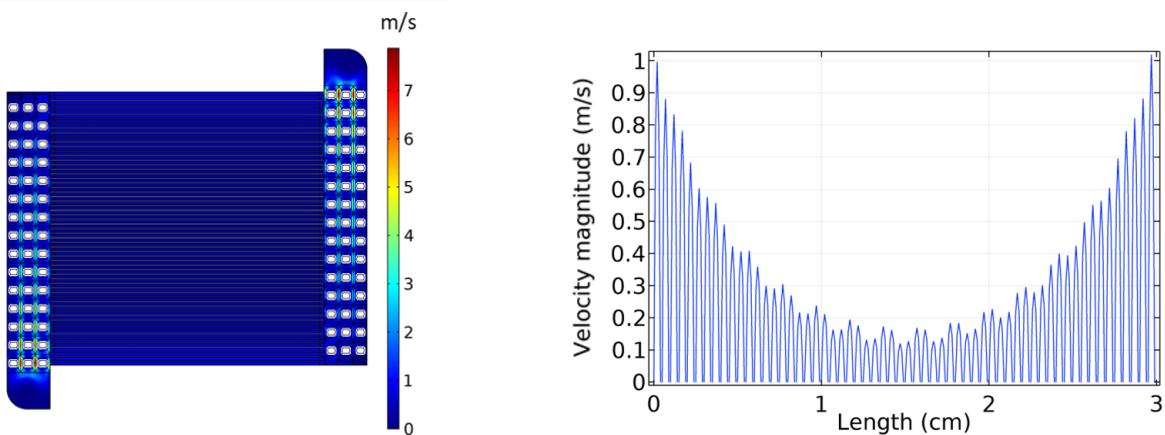


Figure 4.17: Velocity distribution in the first AM prototype (left), velocity distribution in the midsection of the channels (right).

Sloped Parallel flow field, present better flow distribution in the domain. Here the maximum to minimum velocity ratio is 30%. In each channel group, first and the last channels have the highest velocity. This effect was seen in the first prototype but in smaller scale, since the channels are spread in 10 groups instead of 60 individual channels.

cross-flow structure has the best flow distribution compared to the other two designs. Figure 4.19 present the pressure difference between the geometries. The maximum to minimum velocity ratio is 20%. 10% difference in velocity distribution between the sloped parallel flow and crossed flow is due to the difference in structure. In the first design the channels are rounded in the both sides near the active surface. However, in crossed flow they have sharp

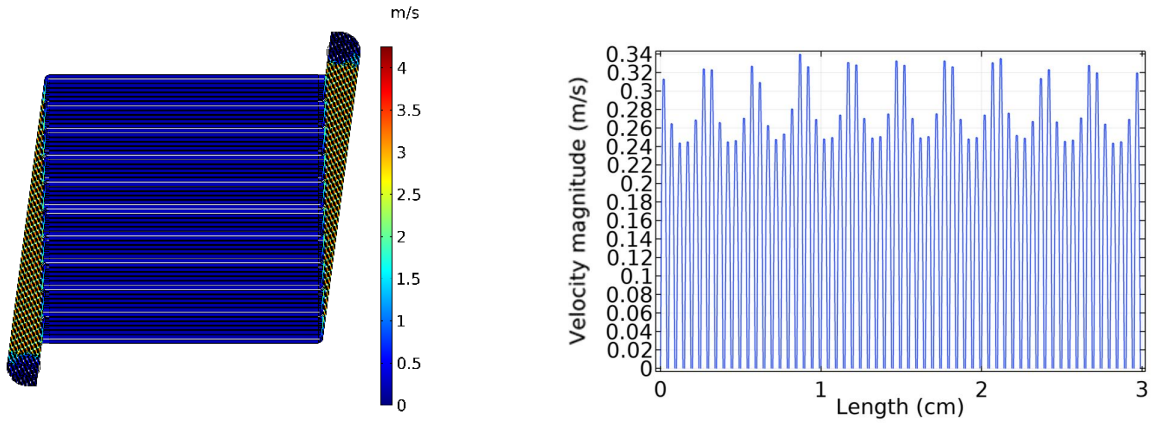


Figure 4.18: Velocity distribution in sloped parallel flow field (left), velocity distribution in the midsection of the channels (right).

edges (Figures 4.18 and 4.20).

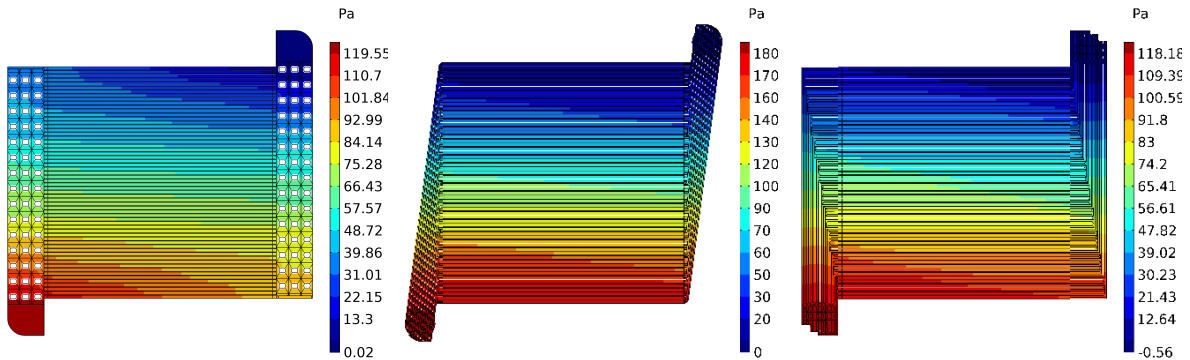


Figure 4.19: Pressure distribution in different flow field.

The pressure drop between the inlet and the outlet is a reliable parameter to differentiate between the three designs. The first prototype and the crossed flow field present similar pressure drop in domain. The first prototype presents a more drastic pressure change in each channel therefore, the velocity distribution is inhomogeneous compared to crossed flow. The sloped flow presents the highest pressure drop between the three designs. In the first and the last design the highest possible surface was used in the geometry however, the least surface or volume was used in the sloped structure. This is the main reason for the highest pressure drop in the sloped parallel flow structure.

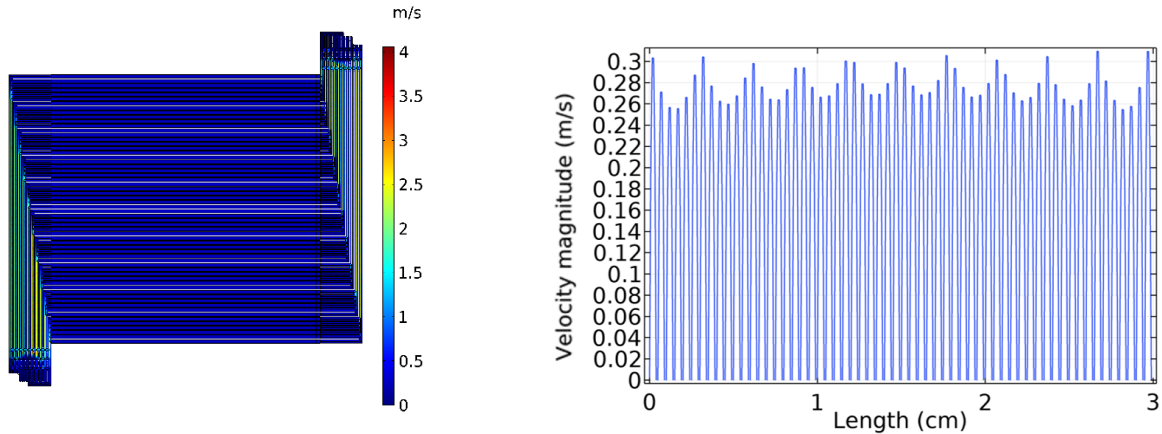


Figure 4.20: Velocity distribution in crossed flow field (left), velocity distribution in the midsection of the channels (right).

## 4.4 Reference system comparison to first prototype

With the first prototype the limitations of additive manufacturing were tested. Moreover, the performance was measured with our in-house designed test rig. The test rig measures the polarization curve which documents the relation between current and potential in the fuel cell. The importance of this diagram was mentioned in 1.3.2 section.

Until now we have presented the simulation results in the flow field and reference system. In order to have a better understanding this result we perform the experimental study. The simulation provides insight on parameters which are hard to determine in the experiment such as, local velocity, pressure, local concentration of reactants. Therefore, the author performed the simulation to determine these parameters and validate the reference FC by simulation analysis.

The experiment in the test rig was performed by another PhD student. She measured the polarization curve for both first prototype and the reference fuel cell. The polarization curve shown in Figure 4.21 present that the reference FC is capable of generating more current with less voltage drop. In other words, the first prototype generates less power than the reference system. This might be due to unequal velocity distribution between channels and the land to channel ratio. Moreover, the channel to land ratio in the reference system is 1 whereas it is 2.7 in first prototype. Hence the reactants have more contact with the membrane in the first prototype. The generated electricity cannot transfer well from the membrane surface due to insufficient physical surface contact with the metal grid.

## 4.5 Conclusion

In conclusion the first prototype presents that manufacturing monopolar plate with SLM method is feasible. However, as it was expected from non-optimized flow field this prototype

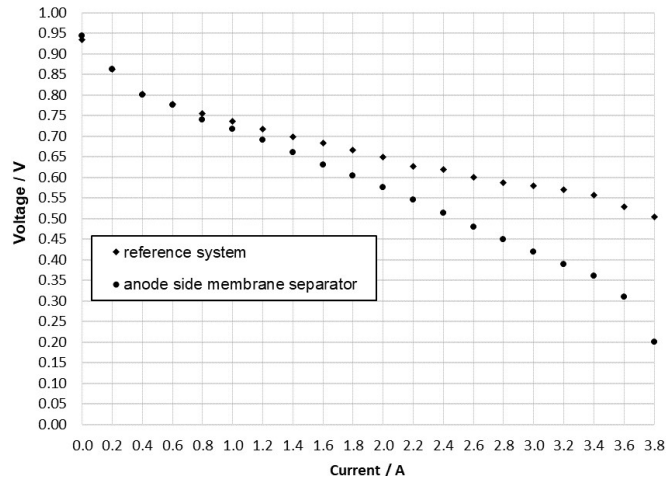


Figure 4.21: Polarisation curve of the first prototype and reference system in experiment (left), The fuel cell assembly in the DHBW test rig. Voltmeter shows the operating voltage of the PEMFC (right).

harvests less energy from the membrane compare to the reference system. This is due to non-uniform flow field created by the supporting structure before the parallel channels as we have presented it in Figure 4.17 right. Moreover, the channel to land ratio influences this result as it was mentioned before. This chapter details the numerical and experimental tools that help us improving our knowledge of BPP channel fluid flows in operating fuel cell. Moreover, it describes the innovative designs suggested by the numerical approach for the fluid domain.

Since 2D and 3D codes return different results, accurate flow simulations require the third dimension. Ratio of the height of the channels to the width is small which makes the influence of third dimension not negligible. In this case the here used LBM code requires considerably long computation time to drive the algorithm that uniform the maximal velocities in the channels by adapting their widths. Appropriate design of inlet in the set of the channels proved necessary to achieve almost uniform velocity distribution in the parallel channels. Nevertheless, the monopolar plate prototype issued from this approach was found to produce less electrical power than the reference system. This study can support the future studies for manufacturing the monopolar plate using SLM method by providing a holistic view from DFM to CFD. Moreover, the mentioned optimisation criteria can support the researchers in future studies to design and build improved flow fields in monopolar plates.

# Chapter 5

## Application of passive directional transport in PEMFC

### 5.1 Introduction

Chapter 4 discussed innovative designs of anode side BPP channels: they supply the fuel cell membrane with hydrogen. Cathode side channels instead carry air, and manage the water produced by the electrochemical reaction. It is known that the dynamic viscosity of air and hydrogen are in 2.01 ratio. Moreover, stoichiometry defines cathode and anode flow rates to be in a ratio of 3.18. Hence, cathode BPP channels must be wider to decrease the pressure drop. Moreover, the water produced by the reaction is in liquid and/or vapor phase depending on cell temperature. Water vapor is added to the cathode (by the humidifier) to increase the membrane conductivity [72]. The liquid water tends to cause channel blockage and irregular flow distribution: both decrease the cell power by limiting the reactants and the chemical reaction. This was mentioned in section 1.3.2.

Therefore, in this chapter we study how appropriately modifying a planar surface may help us evacuating superfluous liquid water without any external energy input. This means that we concentrate our attention on passive transport. The liquid water can be transported actively or passively. Active transport occurs when a pump activated for a short period of time increases the flow rates to blow the liquid water out of the fuel cell. By contrast, no external energy is needed for passive transport caused by capillary forces, i.e. by the interaction between solid surface and fluid that lifts water in a thin pipe, for instance. We moreover say that the transport is directional when liquid motion exhibits a privileged direction. We will see that super-imposing appropriate relief to planar surface facilitates directional passive transport of water drops. We postpone to the future the task of applying the result of this chapter to new design of cathode bipolar channels. If the author can validate directional transport it may be applied to the bottom of cathode as it is depicted in Figure 5.1. The chapter begins by Section 5.2 that specifies our approach of passive directional transport on almost planar surfaces patterned with fin shaped parallel channels already described in literature. However, our ultimate aim requires specific materials. This approach combines

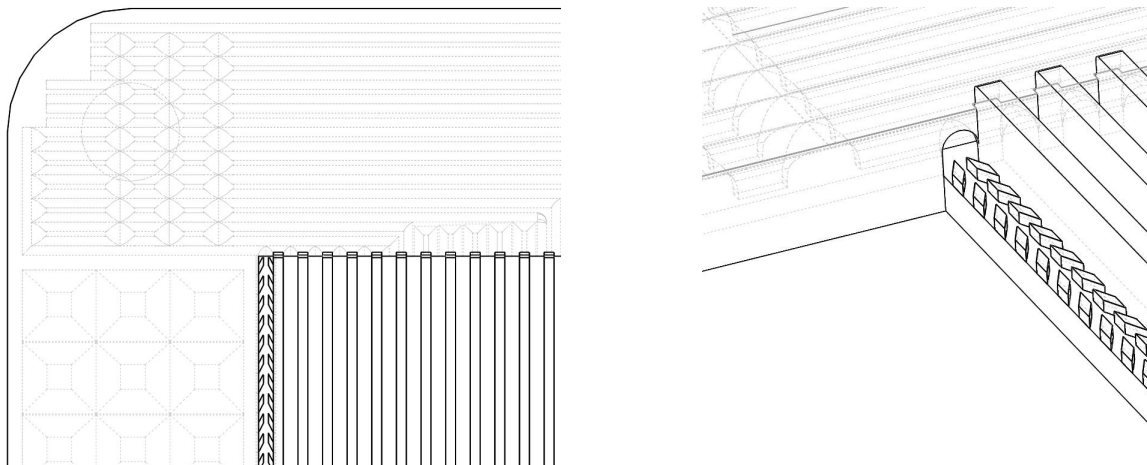


Figure 5.1: Top view of possible integration of fin-shaped geometry in single first channel from left (left), cutaway side view (right) the structure is removed for the visibility.

numerical simulation and experiment . The experiment is described in Section 5.3, since it prescribes the conditions of the simulation. The latter uses two methods, among which the LBM code already considered in Chapter 3. Section 5.4 is devoted to a complementary approach based on VOF method. Section 5.5 discusses the results and compares with the experiment.

## 5.2 Problem and method

In view of improving liquid transport in parallel flow field BPP, we apply numerical and experimental approaches to predict and evaluate spontaneous liquid displacement on manufactured structures made by micro laser sintering with stainless steel .

### 5.2.1 Foreword

In microfluidics, water forms droplets which remain pinned on the surfaces. The transport or spread of these droplets is a challenging task in an industrial framework as lubrication, chemical reaction, heat exchanger, and water circulation in fuel cell. In most microfluidic devices, liquid motion is provided by a pump or an external energy input such as piezo elements. Nevertheless, surface heterogeneity as a gradient of wettability enhances droplet spreading without any external energy input. It is a relaxation dynamics of the drop/surface system which decreases its free energy. Such liquid movement is usually called passive transport when the liquid flow has a privileged direction. Passive transport becomes highly desirable in industrial processes [73], [74].

Such a directional transport is involved in living world. Some species like insects, lizards

and plants living in deserts use it to harvest water [75]–[78]. Heterogeneous wettability driven liquid motion was also observed on wharf roach skin [79], and its frequent use by living organisms inspired a variety of industrial applications [80]–[82]. In all these situations, it is the surface heterogeneity that causes liquid drops to move. Heterogeneity can result from spatial variations of the wettability [83]–[87], i.e. solid-liquid contact angle. This is done usually by physio-chemical treatment applied to solid surface [88]–[90]. Surface heterogeneity can also be caused by small scale (micrometric) topographic structure on the smooth solid surface acting as capillary [75]–[77], [91]–[93]. The water spreading through these microchannels is called water wicking in the literature [91].

In the present chapter we focus on the latter case, and more specifically on spontaneous directional liquid drop wicking caused by patterns forming channels added on solid plate. Motivated by the design of BPPs that evacuate water excess in Proton Exchange Membrane fuel cells [94], we consider fin-shaped channels as those proposed by [91]. Inspired by the latter reference, we present an experiment that shows the direction spreading of a water drop on the patterned surface. We prepare it and interpret it by numerical simulation of the evolution of the drop. Moreover, we choose materials compatible with low temperature hydrogen fuel cell constraints, i.e. robust and conducting electricity. Various experiments analyze passive directional water motion driven by geometry [75]–[77], [79] or by wettability gradient [88]–[90] as well. Various numerical simulations analyze the evolution of velocity field, water content, interfaces and pressure in the latter case [83]–[90], [95]. However, theoretical approaches to drop wicking in channels of complex geometry [91][92] merely use semi-empirical formulas, and such domains do not simplify numerical simulation. No reference attempted simulating liquid drops evolution on channels as complex as the fin-shaped ones first considered by [91] or limited by tilted pillars [93].

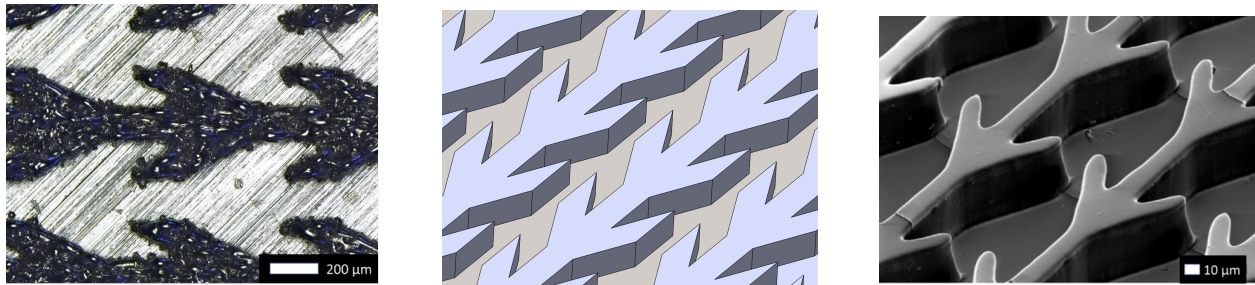


Figure 5.2: Fin shaped structures added to a flat surface. Top views of the fin-shaped structure studied here and manufactured by SLM in a picture from above (left), CAD in an isometric view (middle), and original PDMS part (right). Notice the different scales and compare the rough metallic structure manufactured by SLM (left) with the smooth surface considered in [91] made of resin (right).

## 5.2.2 Structure geometry

We modify the flat and smooth surface by building micro-channels on it. The structure of the micro-channels is inspired from the the fin-shaped one on which [91] observed one-directional

wicking (Figure 5.2 right). represents these micro-channels: (left panel) here considered ones and (right panel) the original version of [91]. In this chapter, the term "channel" refers to fin-shaped micro-channel and no longer to the fuel cell channel.

According to , the studied channels are about four times wider and two times deeper than the original version of [91]. Whether we still observe at larger scale the one-directional wicking is not a priori guaranteed, since experiments of [92] demonstrate that pattern scale does influence spontaneous directional wicking, which [91] found more rapid on thinner channels. The fuel cell framework imposes also a material that significantly differs from the ones of [96], these changes are discussed in the following.

### 5.2.3 Material constraints

A robust material that conducts electric current and resists corrosion and heat is highly desirable for our purpose. Stainless steel satisfies these requirements. Since [91] found smaller patterns more efficient, we manufacture our structures by the Selective Laser Melting (SLM) technology that adapts to steel and achieves high resolution. Nevertheless, sizes as small as in this reference are out of reach. Moreover, the SLM technique cannot avoid slight deviations between CAD design and manufactured component, which we also expect to influence wicking. Finally, the reaction product in PEM-fuel cell is pure water, which returns a water/steel contact angle larger than in the drop transport experiment [26, 1]. It turns out that the latter was performed on Polymethylmethacrylate (PMMA) and Polydimethylsiloxane (PDMS) substrates, which of course do not satisfy our robustness and electric conductivity requirements. Moreover, reference [96] associates these substrates with IPA and soapy water. Since it seems that drop wicking on a given structure is decreased when we increase the contact angle, we expect uncovering optimal conditions upon exploring the 0-70-degree range. The numerical simulation is the most flexible tool to study the influence of contact angle. However, it needs being validated against real life experiments. Our method consists in combining these two approaches.

### 5.2.4 Method

Numerical approach using either the interface tracking by Volume of Fluid (VOF) or the Lattice Boltzmann Method (LBM), captures drop motion in a channel limited by the patterns described in Figure 5.2. We will see in Section 5.5 that interface tracking suggests directional drop motion at contact angle smaller than 70 degree. We validate the numerical approach by experimental set-up on steel structures based on the geometry introduced by [87]. We do observe liquid transport right after a distilled water drop is set on each one of three steel structures manufactured by ourselves and exhibiting the fin-shaped geometry of Figure 5.2 with slightly varied scales. It turns out that channel width influences spontaneous drop displacement. Manufacturing and measurements are detailed in Section 5.3. After a brief description of the underlying physical model in Section 5.4, numerical issues are detailed in Section 5.5 which also compares with the experiment.

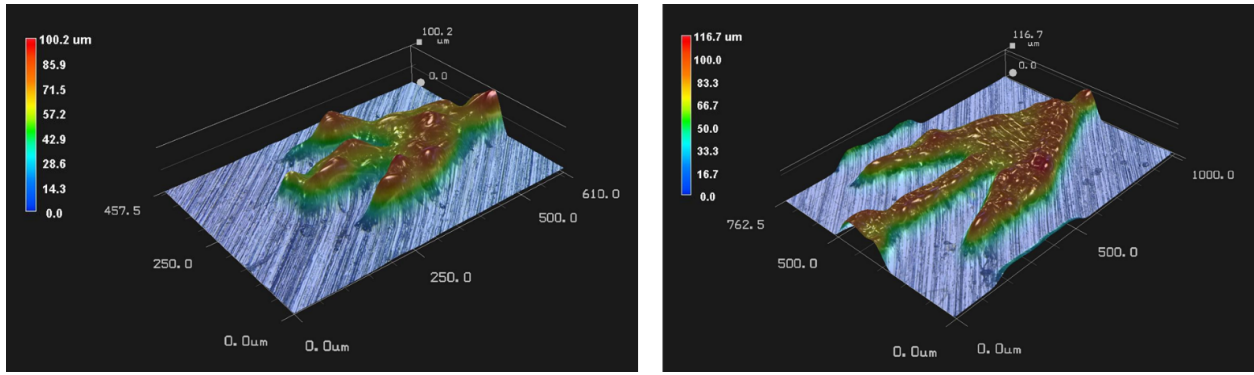


Figure 5.3: The pictures represent the basic element of structure manufactured by SLM. [left] Structure A and [right] structure C of the experimental set-up (Figure 5.4) corresponding to the smallest and largest lengths specified in Figure 5.5. Colours indicate height measured from the steel platform.

### 5.3 Experimental study of liquid wicking on fin-shaped patterns

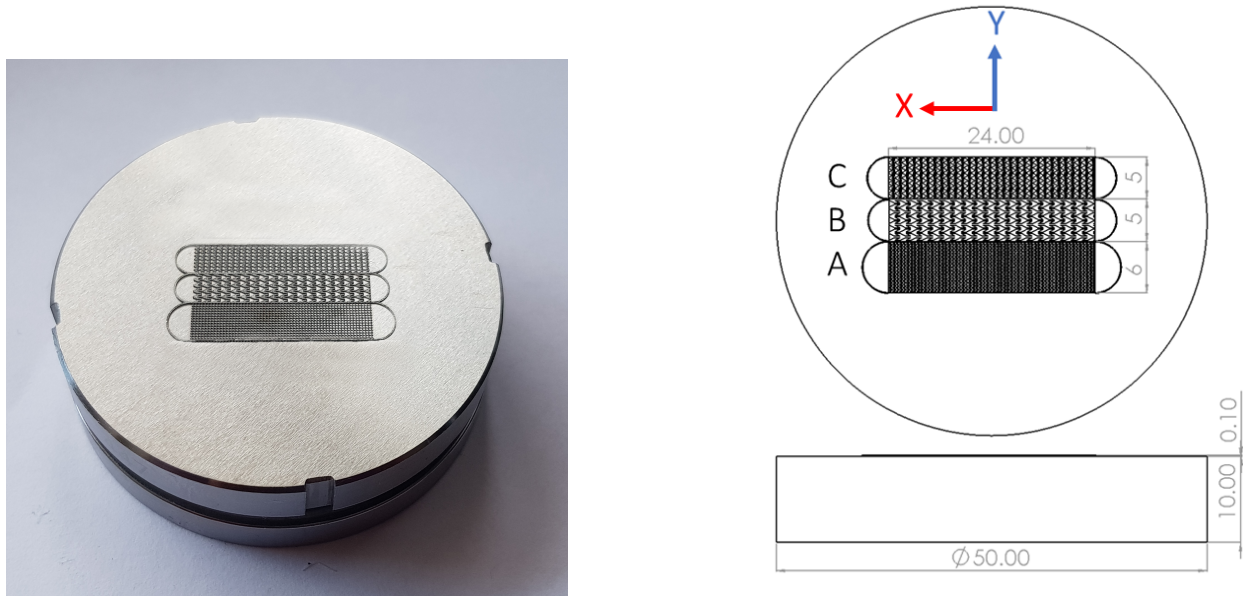


Figure 5.4: Three adjacent structures exhibiting fin shaped channels added to the steel base by SLM. [left] Actual A, B and C structures. [right] CAD design documenting the total length and width of each structure, in millimeters.

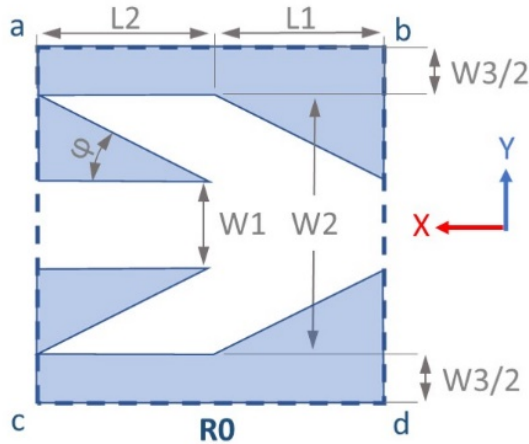
The manufacturing process of adding fin-shaped pattern of various width on steel surface is the first step of our experiment. The next step consists in observing drop evolution on the obtained structure.

### 5.3.1 Substrates manufacturing and physical properties

As in [91] the substrates on which we study drop wicking are flat surfaces with fin patterns forming channels. One of them is shown in Figure 5.2. Platform and patterns are here made of 1.4112 stainless steel, and we build three such structures denoted A, B, C on a single platform. Figure 5.3 shows the final appearance of the modified platform. Each of the three structures A, B, and C is progressively grown on steel platform by an additive process that repeats two successive steps. The first step consists in applying a uniform thin steel powder coating to build the channel walls on a definite subset of the platform. The second step improves the consistency of the resulting ensemble by Selective Laser Melting (SLM). These two steps are repeated until channel wall height reaches the desired value which here is  $100 \mu m$ . However, at the first step of the first repetition the powder coating is set on a subset of the platform. We call this subset R, and define it immediately below: each structure has its own R region which will serve as a basement for its channel walls. R region is an essential element of additive process definition. Two sets of transformations deduce it from the elementary pattern R0 colored in blue inside rectangle 'abcd' which we see on Figure 5.6. The transformations are i) a finite number of translations of amplitude  $(L1+L2)$  in longitudinal axis direction (x) with maximum achieving 24mm total length and ii) adjacent copies periodically added in the transverse horizontal direction y. This forms the basis for the walls of between 5, 8, and 15 adjacent identical channels for structure B, C and A respectively. Each such channel is itself made of a finite number of elementary cells (or voids) that are copies of the white surface inside 'abcd' rectangle (the complement of R0 in this rectangle). The top view of the CAD drawing at the right of Figure 5.4 represents the three sets of channels that constitute structures A, B and C. Total widths of them are 5, 5 and 6 millimeters.

Geometric specification is not enough to determine structure ability to promote directional wicking, since initial surface properties and powder grain size do influence the wettability of each structure. Indeed, slight initial platform roughness is necessary to enhance powder adhesion. However, increasing roughness decreases the wettability. Here, initial platform roughness is 207 RMS. Another influent parameter is surface roughness of laser sintered part. We used steel powder with grain diameter of about  $5 \mu m$ , which is very fine. However, this is not the only factor limiting the resolution of the final product, strongly influenced by laser beam focus. Here the final resolution is  $30 \mu m$ , and we see on Figure 5.3 that the channel walls slightly deviate from the isometric CAD drawing of Figure 5.2 (middle) and exhibit small scale defects. Moreover, one can observe that steel pattern surface (left) is rougher than the resin surfaces (right) of [91].

We thus obtain three manufactured structures A, B and C positioned side by side on the same steel plate. Each structure is wide enough to allow us setting a droplet on it without touching its boundaries. A picture of the resulting device is shown in Figure 5.4, and a drawing.



Variable	A	B	C
$\varphi$	$27^\circ$	$27^\circ$	$27^\circ$
L1=L2 (mm)	0.2	0.64	0.4
W1 (mm)	0.1	0.16	0.1
W2 (mm)	0.3	0.8	0.5
W3 (mm)	0.1	0.16	0.1
depth (mm)	0.1	0.1	0.1

Figure 5.5: The elementary pattern from which we deduce the channel wall basement called R region. The elementary wall basement with a thickness of  $0.1\text{mm}$  ( $R0$  in the text) is in blue. the channel elementary cell is in white. Both are included in the rectangle 'abcd'. Adding copies of this rectangle adjacent to its parallel to  $y$  sides defines one channel and its walls. Then, adding adjacent copies of the ensemble forms the channel walls basement for structure A,B or C.

### 5.3.2 Experiment

The spontaneous drop motion on A, B and C is captured by videos of three liquid drops successively set on these structures. For this purpose, we used Keyence VHX-600 microscope equipped with VH-Z20R and VH-Z100R lens. The steel plate with the structures was horizontal during the experiment and the microscope was positioned above. In addition, photos and videos were captured using Samsung Galaxy Note 8. In all the tests distilled water had contact angle of about 50 degrees.

Figure 5.7 displays four snapshots representing the different steps ( $t_1, t_2, t_3, t_4$ ) of the evolution of single drop set on the middle of structure B. The snapshots have been extracted from a video. Drop motion on other structures only differ by the time instants at which the drop completely wets the structure in  $x$  or  $-x$  directions. On all structures wicking starts as soon as the drop is set on it at initial time  $t_1$ . We quantify the mean velocity in  $x$  or  $-x$  direction by recording  $x_1, x_f$  and  $t_f$  that represent initial drop meniscus position and structure end in the considered direction, and the time at which the fluid reaches structure end. With these notations, the average velocity in each direction is

$$\bar{V} = \frac{x_f - x_1}{t_f - t_1}. \quad (5.1)$$

It is positive in  $+x$  direction, and negative in  $-x$  direction. Figure 5.6 documents absolute values observed in these two directions on the three structures A, B, and C. On each of these three structures the average velocity in the negative direction is nearly half the value observed in the positive direction. Recalling Table in Figure 5.7 that documents channel and wall widths  $W_i$ , we observe larger velocities in both directions  $x$  and  $-x$  on thinner

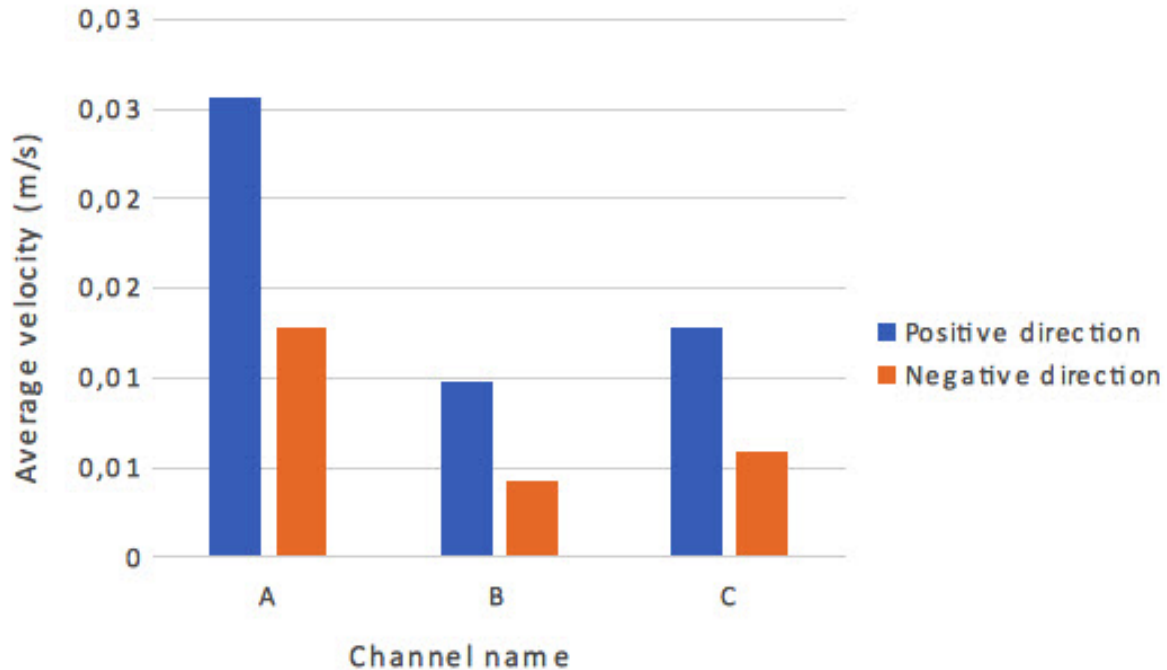


Figure 5.6: Average velocity absolute values of water wicking in  $x$  and  $-x$  directions for the three different channels A, B and C.

structures.

Wicking dynamics is fast but not uniform. Slowing down the videos suggests that front velocities are uneven, intertwining slower and more rapid steps, especially in  $-x$  direction. We discuss this point in Section 5.5, in view of numerical simulation that returns much smaller time resolution. These videos will serve as basis to check a numerical method by seeing whether it mimics the trends observed on the motion of a drop set on our fin shaped channels.

## 5.4 Physical model and Numerical methods

In a single channel representing the fin-shaped geometry of structure A, B or C we simulate two phase flow according to the Volume of Fluid (VOF) method [97]. After having briefly set physical model and numerical VOF method, we describe the initial data which we use to mimic the experiment detailed in Section 5.3.2.

### 5.4.1 Physical model and mathematical formulation

Among diverse interface tracking methods, we choose the Volume of Fluid approach that assumes one (two phase) fluid of velocity  $\vec{u}$  and volume density [98], [99].

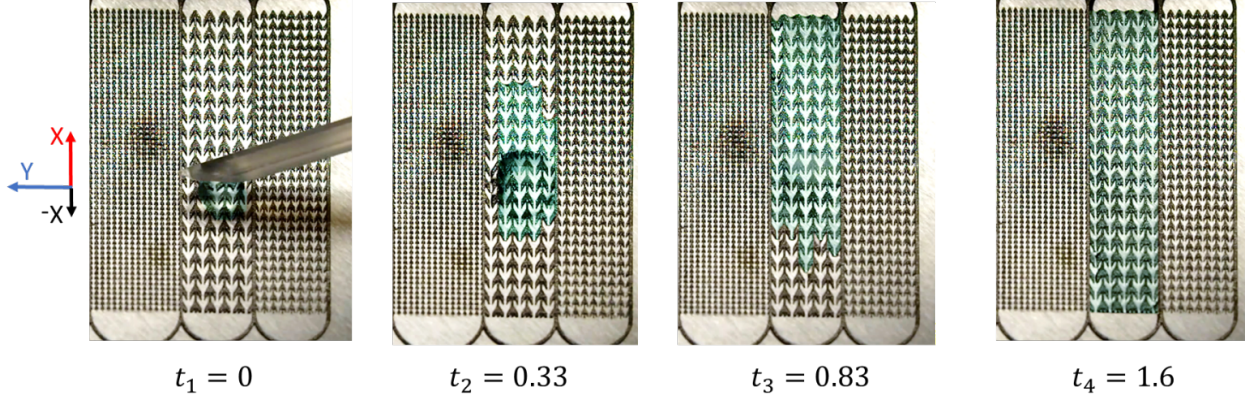


Figure 5.7: Time evolution (time unit in seconds) of directional drop wicking on structure B (middle structure). The bottom of the structure appears as white and the top is dark. Water is colored for better visibility. The first picture shows the pipette that places a water drop on structure B at time  $t_1$ . At time  $t_2$  the drop has already begun to wick through the channels. At time  $t_3$ , the structure has been completely flooded in the positive direction while wicking is slower in the negative direction. Transport in the negative direction is completed at time  $t_4$ .

$$\rho = \alpha \rho_{liq} + (1 - \alpha) \rho_{gas} \quad (5.2)$$

In which  $\alpha$  and  $\rho_{liq}$  are liquid phase volume fraction and volume density, and the volume density of the gaseous phase is  $\rho_{gas}$ . Moreover, the VOF approach assumes two phase fluid viscosity  $\mu$  related to liquid and gaseous phase viscosities  $\mu_{liq}$  and  $\mu_{gas}$  according to

$$\mu = \alpha \mu_{liq} + (1 - \alpha) \mu_{gas}. \quad (5.3)$$

In this model, fluid velocity  $\vec{u}$  and liquid volume fraction  $\alpha$  evolve according to

$$\frac{\partial(\rho \vec{u})}{\partial t} + \nabla \cdot (\rho \vec{u} \otimes \vec{u} - \mu (\nabla \vec{u} + \nabla \vec{u}^T)) = -\nabla p + \vec{f}_\sigma + \rho \vec{g} \quad (5.4)$$

and

$$\frac{\partial \alpha}{\partial t} + \nabla \cdot (\alpha \vec{u}) = 0 \quad (5.5)$$

The momentum equation (5.4) includes the continuum surface force  $\vec{f}_\sigma$  introduced by [98]. In the VOF approach,  $\alpha$  is assumed to continuously vary between 0 and 1 in a neighborhood of the liquid gas interface. There, the continuum surface force is given by

$$\vec{f}_\sigma = \sigma \frac{\rho \kappa \nabla \alpha}{\frac{1}{2}(\rho_{liq} + \rho_{gas})}, \quad (5.6)$$

where  $\kappa$  is a continuous function representing the free surface curvature and is defined in the interface vicinity by

$$\kappa = \nabla \cdot \vec{n} \quad (5.7)$$

In which  $\vec{n}$  is continuous and represents the unit surface normal to the interface. It is also defined in interface vicinity and satisfies

$$\vec{n} = \frac{\nabla\alpha}{\|\nabla\alpha\|}. \quad (5.8)$$

Moreover, solid surface wettability prescribes  $\vec{n}$  at the triple line that is its intersection with the liquid/gas interface.

### 5.4.2 Triple line modeling

At solid boundaries we consider wall adhesion. At the triple air/liquid/solid interface there is the so-called triple line. At equilibrium, the static contact angle  $\theta$  characterizes the wettability. Out of equilibrium, the macroscopic contact angle depends on the front dynamics and it differs from the static contact angle [100]. However, at the mesoscopic scale, it is still relevant to consider the contact angle  $\theta$  [101]. Therefore, following [98] we assume that the normal  $\vec{n}$  at the interface satisfies

$$\vec{n} = \cos\theta \vec{n}_w + \sin\theta \vec{n}_t \quad (5.9)$$

in which  $\theta$  is the equilibrium contact angle. Vector  $\vec{n}_w$  is the unit vector normal to the wall, and  $\vec{n}_t$  is tangent to the wall and normal to the contact line. At the triple line, equations (5.8) and (5.9) imply

$$\cos\theta \vec{n}_w + \sin\theta \vec{n}_t = \frac{\nabla\alpha}{\|\nabla\alpha\|}. \quad (5.10)$$

The latter equation is a boundary condition for  $\alpha$ . From this equation the code deduces  $k$  and  $\vec{f}_\sigma$ .

### 5.4.3 2D and 3D geometry for the Simulation

The numerical simulation is performed within a simplified geometry because of the computational cost. Instead of the several parallel channels in experiment (Figure 5.6), we apply 2D and 3D simulation in a domain that consists in a single channel composed of 5 to 8 elementary cells repeated in  $x$  direction. The 2D simulation is obtained by considering the vertical  $z$  direction as the invariant direction. Most significant results are in 3D, but 2D simulation helps understanding the key role of the different edges exhibited by the fin shaped geometry. In both cases, we assume fixed and constant atmospheric pressure.

The 2D and 3D simulations do not only differ by the third dimension but also inlet conditions are different. In the 2D simulation we inject the liquid at two inlets. They are positioned in the middle of the channel boundary of one elementary cell, itself in the middle of the channel as indicated in Figure 5.8. Moreover, each inlet flow is fed at constant rate  $1.06\text{mm}^3/\text{s}$ . The 3D simulation, differently, is started from an initial condition that resembles more the

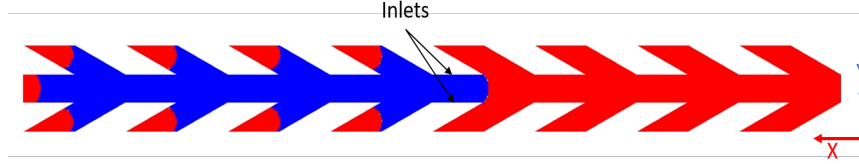


Figure 5.8: VOF two-dimensional simulation with  $\theta = 50^\circ$  and the geometry of the horizontal section of channel A.

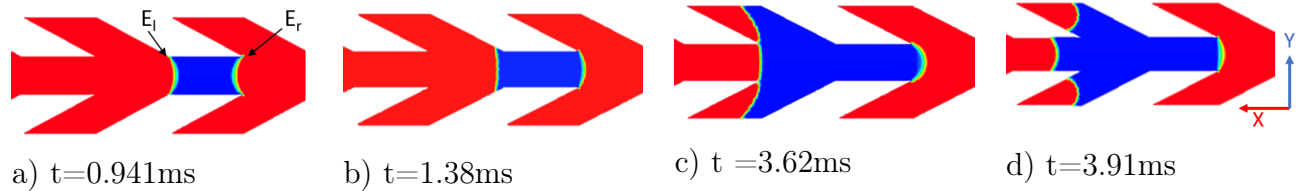


Figure 5.9: Snapshots of the asymmetric transport using the 2D VOF simulation. Parameters are as in Figure 5.8.

experiment: at time instant  $t = 0$  we put on the channel a small cuboid of 0.3 millimeters high and of same  $W_2$  width as the channel. The length is between one and two elementary cells. The volume in the channel below the cuboid is filled up too.

The VOF simulation pursues an ultimate aim: being able of arbitrarily varying fin-shaped channels geometry and surface wettability, in view of optimizing devices that enhance directional transport under some constraints. The next section checks that the numerical tool returns issues appropriate to this aim although the simulation domain is not exactly equivalent to the set of channels of A, B or C structures, even in the third dimension. Nevertheless, we will see that simulations and experiments suggest similar trend.

## 5.5 Water wicking simulation

If we compare it with our experimental conditions, the 2D simulation amplifies the role of the edges of the fin-shaped channel walls and retrieves (in Section 5.5) the selective pinning predicted by Gibbs criterion near obstacles exhibiting edges [102]. In three-dimensional geometry, however, the role of the edges is mitigated by channel bottom and the VOF issues come closer to our experimental observations. This allows us specifying which force dominates liquid flow in the different subsets of fin-shaped channel.

### 5.5.1 2D simulation

The 2D variant of the numerical code described in Section 5.4 represents a three-dimensional two phase flow invariant in  $z$  direction, between infinite walls based on the boundary of the R region defined in Section 5.3. We do not expect that such flow resembles so much our experiment, and especially its initial condition that indeed depends on  $z$ . Instead, we impose a liquid flux ( $10.6 \text{ mm}^2/\text{s}$ ) at inlets located on parts of the both sides of domain boundary, in a region where these sides are parallel, as on Figure 5.8. These conditions are reminiscent of reference [102] that describes a ( $z$  dependent) liquid flooding a flat surface decorated with obstacles that exhibit wedges.

In our simulation we observe that the liquid, driven by the capillary force, begins by completely filling the narrow straight channel that includes the inlet (Figure 5.9a). The left and right fronts are pinned at edges called  $E_r$  and  $E_\ell$ , respectively located at the left and at the right of the inlet. To move again, a driving force is required. In our context, it is the pressure due to the continuous flow at the inlet. Since  $E_r$  is much sharper than  $E_\ell$ , the left front rapidly depins whereas at  $E_r$  the interface bulges gradually while the triple line remains pinned (see Figure 5.9a to c). Right  $E_r$  edges are thus responsible for front pinning while edges at  $E_\ell$  are not, and it is the key of the directional transport in 2D geometry. Note that the acute wedges at the end of the fins do not pin the front moving to the left since they are wetted by water on both sides (Figure 5.9c and d). References [87], [89] already suggested this quasi-static explanation for the directional transport, based on contact angle hysteresis. However, the 2D simulation does not accurately describe the flow in the fins. Indeed, it suggests air trapped in fins and blocking water progression (see Figure 5.9d), a phenomenon that we do not observe neither in the experiment, nor in the 3D simulation.

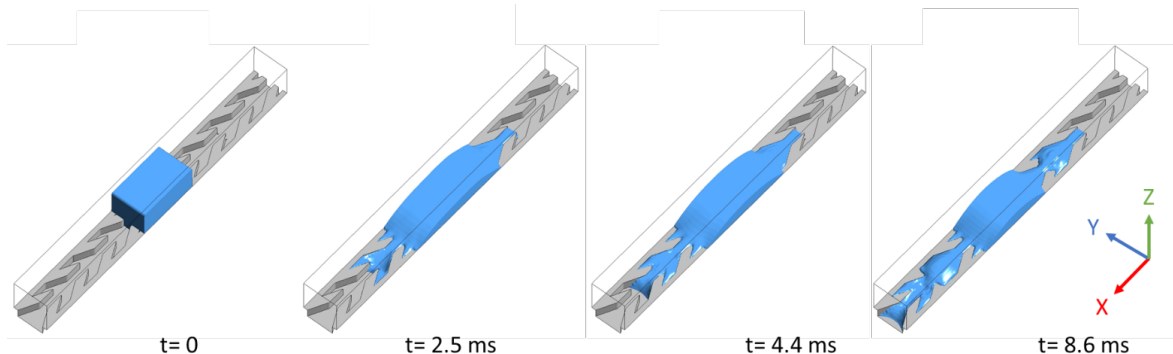


Figure 5.10: 3D simulation of liquid wicking driven by capillary forces on channel A. Blue color represents liquid volume. Contact angle is  $50^\circ$ . The simulation domain is eight elementary cells long. The parallelepiped size is  $\ell_x = 0.7\text{mm}$ ,  $\ell_y = 0.38\text{mm}$ , and  $\ell_z = 0.4\text{mm}$ .

### 5.5.2 3D simulation at $50^\circ$ contact angle

In the 3D simulations the geometry of one cell is identical as in experiment. However, one focuses on a unique series of lined up cells and one imposes periodic boundary conditions in

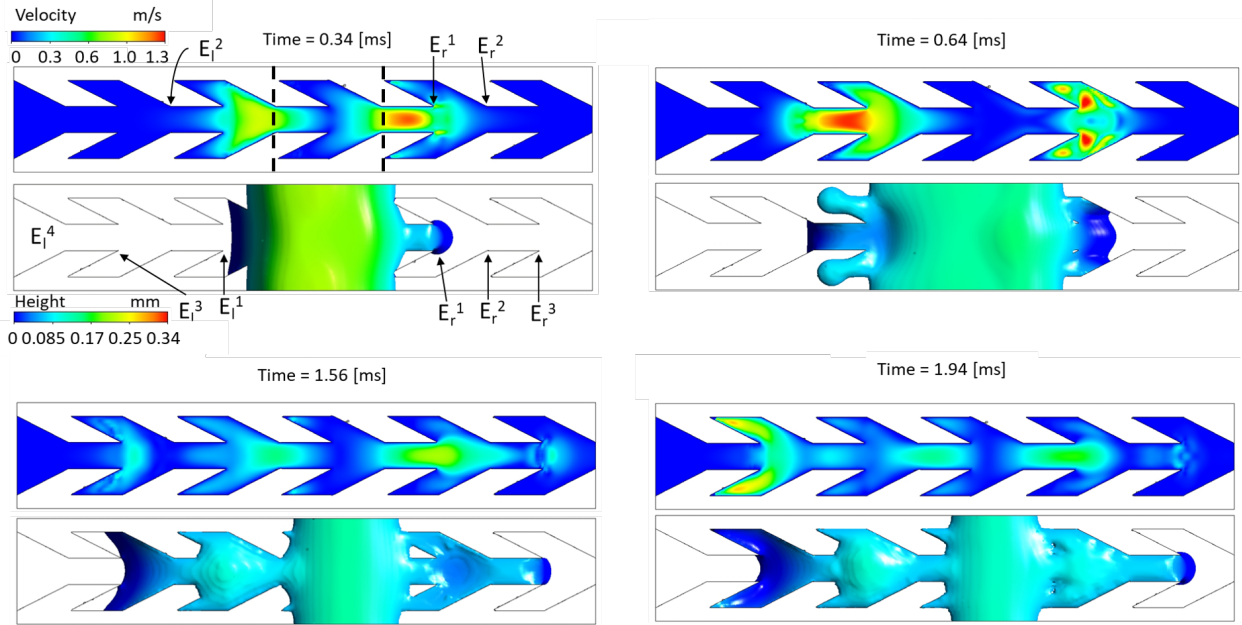


Figure 5.11: Simulated liquid velocity and free surface height during the wicking of a parallelepiped of liquid over a single fin shaped channel. The top of each sub-figure documents the velocity, and at the bottom we see liquid height distribution. Contact angle is  $50^\circ$ . The simulation domain consists of 6 elementary cells. The initial liquid parallelepiped is one elementary cell long.

lateral  $y$  direction. An initial condition similar to the experiment consists of a rectangular 'droplet' placed on the structure (Figure 5.10). The case of water introduced by an inlet at the bottom is studied at the end of Section 5.5.

In these two cases, 3D simulation mimics the intermittent behavior suggested by the videos at the end of Section 5.3, alternating fast and quasi-static steps. Moreover, the smaller resolution of the numerical approach uncovers the details of these different phases which we now describe in the case of  $50^\circ$  contact angle.

Just after having initially been set on the structure (at  $t = 0$ ) the liquid parallelepiped deforms quickly to smoother shape and begins to wick on channel bottom in the two directions  $x$  and  $-x$ . We see it on Figure 5.10 that shows four snapshots of the simulated liquid volume: at time  $t = 2.5ms$  it has flooded one cell to the right of its initial position, and two cells to the left. However, the right front stays pinned until  $t = 4.4ms$  while the left front floods one cell further and proceeds in  $x$  direction. After  $t = 4.4ms$  the right front floods one cell more to the right before stopping. Meanwhile, the left front continues proceeding to the left until it reaches, at  $t = 8.6ms$ , the end of the computational domain.

Figure 5.11 investigates the details of the above described pinning and fin filling processes in  $-x$  and  $x$  directions. Figure 5.11 is issued from a simulation started from an initial parallelepiped shorter than in Figure 5.10, and slightly longer than the elementary cell. The figure is divided into four panels captured at different times. Each panel documents liquid

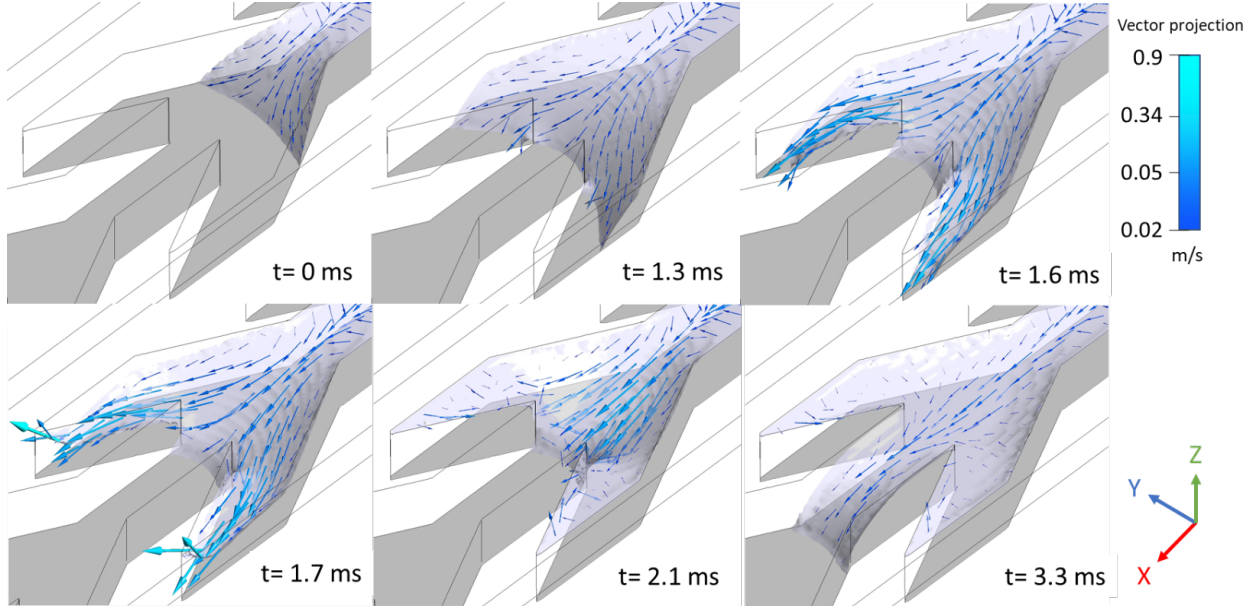


Figure 5.12: VOF simulation detailing fin filling in the  $x$  direction. The continuous color represents the liquid free surface. Arrows display the velocity on the liquid free surface with a color code for the amplitude. However, instead of being started from an initial condition as for Figure 5.10 and Figure 5.11, the simulation is issued from the continuous fluid inlet condition described in Section 5.5.4. The time is set to zero when the liquid enters the fin region.

height below, and the velocity field at  $z = 0.05 \text{ mm}$  above. Since the two-dimensional approach and the discussion of Figure 5.10 pointed the crucial role of convex edges, symbols  $E_r^i$  and  $E_l^i$  ( $i = 1, 2 \dots$ ) mark the channel cross-sections that include such elements at the right and at the left of the initial liquid volume. At  $t = 0.34 \text{ ms}$ , shortly after the initial condition, the first cell is filled and has let water spread to the left and to the right. The view from above of the front evolution (especially the concave left front) is reminiscent of the two-dimensional simulation sketched on Figure 5.9. However, this time the convex front at the right stays pinned at  $E_r^1$  for a finite time after which the liquid spreads out further to the right into the wider part of the channel (Figure 5.11 at  $t = 0.64 \text{ ms}$ ). Two main reasons explain this discrepancy from Section 5.5.1. The first one is that a part of the triple line now lies on channel bottom while contact angle hysteresis only occurs at edges. Advancing by spreading on bottom surface and circumventing edges is easier, and it is what we observe at  $t = 0.64 \text{ ms}$ . The second reason is the velocity field at  $t = 0.34 \text{ ms}$  which suggests not neglecting inertia, differently from the quasi-static approach of [91]. Once the fins between  $E_r^1$  and  $E_r^2$  are filled (shortly after  $t = 0.64 \text{ ms}$ ) the right front continues to advance in the straight narrow channel. At  $t = 1.56 \text{ ms}$  it is at  $E_r^3$ . However, this time the flow velocity is about two times slower. Therefore, the right front spreads a little beyond  $E_r^3$  before immediately receding ( $t = 1.94 \text{ ms}$  in Figure 5.11). Surface tension causes the back flow by decreasing the free surface, and hereafter the front remains pinned. Kinetic energy is now dissipated.

On the opposite side, the left front approaches  $E_l^2$  at  $t = 0.64 \text{ ms}$ . When it touches the acute

wedge  $E_l^3$  at  $t=1.56ms$ , the flow suddenly accelerates. It can be seen between time instants  $t = 1.56ms$  and  $t = 1.94ms$ , because the tapered geometry of the fin increases the ratio of the wet solid surface to the liquid volume in the fin. Moreover, the kinetic energy is only partly dissipated when the liquid completely wets the fin surface. This results into reverse flow in the fins, converging to the middle of the channel between  $E_l^2$  and  $E_l^3$  (Figure 5.11 at  $t = 1.94ms$ ). The volume increase in the center of the channel increases the free surface area. This transforms a fraction of the kinetic energy into surface energy. Relaxation then causes water to spread again, and to flood the straight channel between  $E_l^3$  and  $E_l^4$  which acts as capillary. Same trend is observed on Figure 5.12 that details the fin filling process and represents the free surface and its velocity issued from a simulation in which the water input was different, however. The figure specifies the behavior of the front near a cross section that it reaches at  $t = 1.3ms$ , and plays the role of  $E_l^3$ . Observe the velocity increase that develops in the fins before returning to median region. Meanwhile the front slightly advances in the straight channel before receding during a pause that lasts over  $0.8ms$ . The pause stops when the higher velocity has returned to the median region to help the front flooding the next straight channel to the left. Thus, in  $x$  direction the simulation alternates rapid straight channel flow and much slower fin filling process, very similar to the quite uneven liquid front progression described in Section 5.3.2.

However, the left directional transport is limited by the amount of liquid deposited and our assumption is that the meniscus would stop before reaching channel end in a longer device with the here considered initial condition. Likewise, the simulated meniscus at the right of the fluid volume is pinned at  $E_r^3$  whereas in the experiments it unevenly continues to the right. A possible cause is the initial amount of liquid about  $50mm^3$  in experiment whereas it is only  $0.1mm^3$  in simulation. An attempt to circumvent the problem of initial volume is studied in Section 5.5.4.

The number of cells filled by the water depends also on the static contact angle between liquid and the structure and on pattern size A, B or C. The next section investigates the influence of the contact angle and the pattern size.

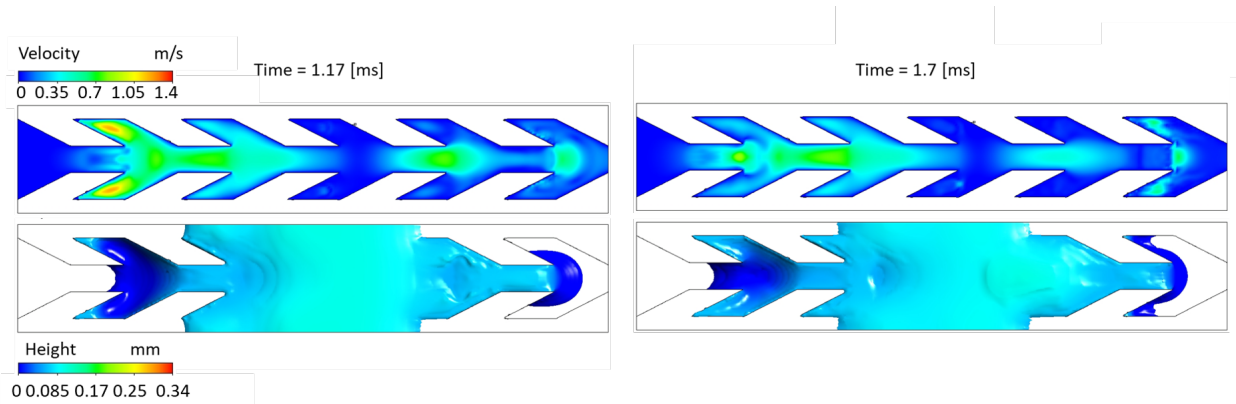


Figure 5.13: Spreading of water beyond the pinning point ( $t = 1.17ms$ ) and backflow ( $t = 1.70ms$ ) for a static contact angle  $\theta = 30^\circ$ . Velocities and liquid height are documented at the top and bottom of each figure, respectively. The initial condition is a two elementary cells long liquid parallelepiped. The channel geometry corresponds to the pattern A.

### 5.5.3 Influence of the contact angle and geometry

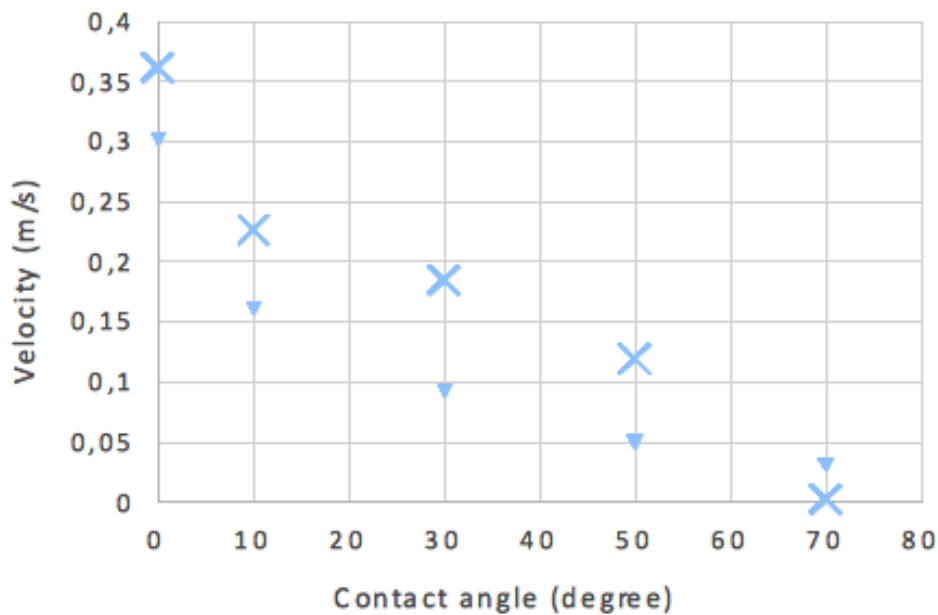


Figure 5.14: Average velocity of the front as a function of the static contact angle  $\theta$ . Blue crosses indicate front velocity in the  $+x$  direction while orange dots indicate the front velocity  $-x$ . Beyond  $\theta \geq 30^\circ$  the front in the  $-x$  direction is pinned and then velocity is not indicated. The geometry corresponds to the smallest pattern A of Figure 5.5.

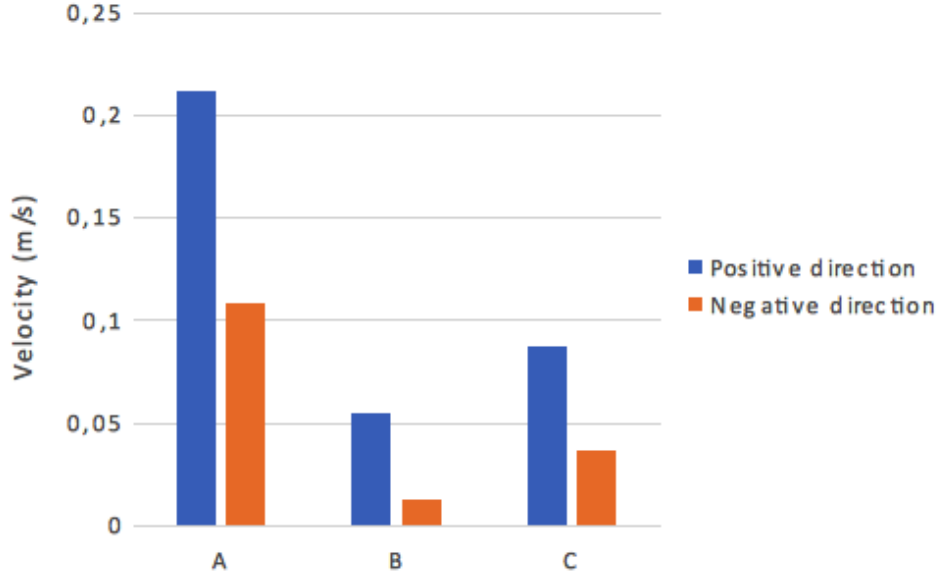


Figure 5.15: Influence of the pattern geometry on the average velocity of the front in the positive  $x$  direction. The contact angle is  $\theta = 30^\circ$ .

In a first part, only the static contact angle  $\theta$  varies but all other parameters remain the same and the pattern size is that of A structure. In other words, we simulate a change of substrate wettability.

Since capillary forces are smaller at larger contact angle slower wicking dynamics is expected also. This is corroborated by the simulation. Indeed, we observe that increasing the static contact angle  $\theta$  decreases the mean front velocity in the positive direction  $x$ . Beyond  $\theta_{lim} \simeq 70^\circ$ , there is no longer water spreading through channels. The volume of water converges rapidly to an equilibrium state which is reminiscent of the steady-ridge of partial wetted liquid on a flat substrate with lateral boundary conditions described in [103].

Conversely, decreasing  $\theta$  from  $50^\circ$  speeds up the wicking front progression in the  $x$  direction (Figure 5.14). However, this affects the front pinning at  $E_r^3$  in the  $-x$  direction. At  $\theta = 30^\circ$ , the fluid spreads over a larger area before retracting and remaining pinned at  $E_r^3$  (Figure 5.13). This dynamics results from a competition between inertia and surface tension. There is a critical value, noted  $\theta_c < 30^\circ$ , below which the front is no longer pinned at  $E_r^3$  and water spreads in both directions. Even in this case the wicking is slower in  $-x$  than in  $x$  direction. Though the front is no longer pinned, the  $E_r^3$  edges constrain the flow to spread out in a thin film beyond  $E_r^3$ . Since the viscous dissipation is high for the spreading of thin films, the kinetic energy is almost totally dissipated passing through  $E_r^3$  in the  $-x$  direction and explains the slower wicking than in  $x$  direction.

To quantitatively study the transport efficiency, we estimated the transport speed averaged on the few cells that were filled in  $x$  direction (Figure 5.14). The mean velocity in both directions decreases as the contact angle increases. The decrease in the  $x$  direction is not linear. Between  $0$  and  $10^\circ$  the velocity is divided by 1.6 while in the larger range  $[10^\circ, 50^\circ]$  it is divided by 2. For  $\theta = 0^\circ$  or  $10^\circ$  the asymmetry of the wicking is weak according to the close values of velocity in  $x$  and  $-x$  directions. Thus, the contact angle  $\theta_c \simeq 30^\circ$  represents

an optimal value of the direction wicking since it is the maximal velocity of the front in the  $x$  direction for which the front is still blocked in  $-x$  direction.

We also simulated the influence of the other geometries B and C of the experiment. The geometry does not qualitatively change the above described scenario. Indeed, the three structures exhibit similar trend for the contact angle dependency of the average velocity, showing in all cases a superior limit  $\theta_{lim}$  for the wicking in the positive direction and a critical value  $\theta_c$  below which the pinning effect vanishes in the negative direction.

The velocity of fluid wicking is influenced by pattern size (Figure 5.15). Especially, between structures A and C, for which the velocity difference is at maximum for  $\theta = 30^\circ$ . This result is qualitatively very similar to the experiment (see Figure 5.6). Indeed the capillary force over inertia ratio is larger in smaller cell: dividing the sizes in  $(x, y)$  plane by  $f$  factor divides the water mass by  $f^2$  whereas the capillary force, proportional to contact line length, is divided by  $f$ .

Despite the qualitative agreement with experiment, the average velocity of the liquid spreading through the channel is about ten times that of the experiment. Surface defects as shown in Figure 5.3 are known to slow down the wetting dynamics [103]. Even considering smooth surface, the low volume of water in simulation comparing to the experiment is another possible reason of this discrepancy. Firstly, the low volume does not allow to average out over a large number of cells implying a large uncertainty. Secondly the Laplace pressure in a small droplet is higher than in a larger one because the Laplace pressure is proportional to curvature. In the next section, we propose a continuous flow to explore the dynamics without the constraint of a limited volume.

### 5.5.4 Continuous flow

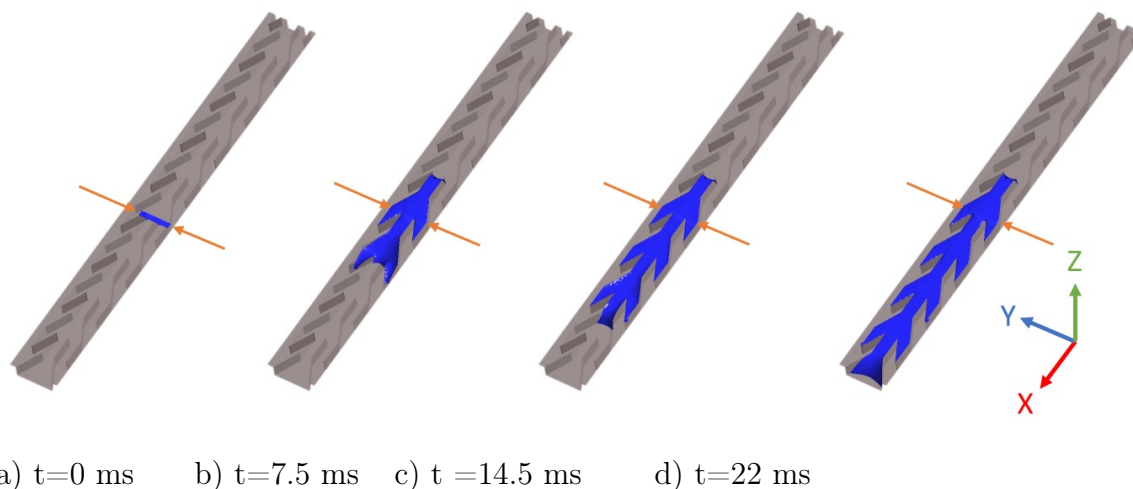


Figure 5.16: 5. VOF simulation with an inlet at the bottom of channel A. Inlet flux is  $1.06\text{mm}^3/\text{s}$  and  $\theta = 50^\circ$ ,

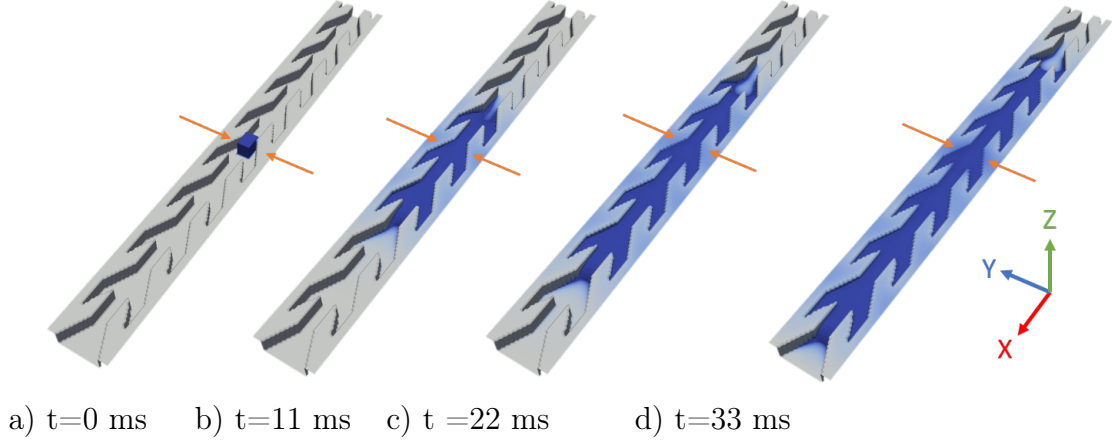


Figure 5.17: LBM simulation with an inlet (red arrows) at the bottom of channel A. Contact angle  $\theta = 50^\circ$ .

To circumvent the problem due to the low volume of liquid in simulation, we impose continuous inlet condition at the bottom of the straight channel in similar way as in the 2D simulation. An interesting feature is that this boundary condition is reminiscent the context of the BPP of a fuel cell as the reaction at the cathode produces a continuous water flow. We simulated the water production by constant flux ( $1.06\text{mm}^3/\text{s}$ ) through a rectangular surface positioned at the bottom of the channel (Figure 5.16).

The simulation reveals a dynamics very similar to what we described in Section 5.5.2. This time, the spread in the positive direction is no longer limited. However, the front is still definitively pinned in  $-x$  direction at the  $E_r^3$  edge. It may be due to front diffusion caused by the interface modeling included in VOF method that excessively increases the transition region at the interface: the resulting underestimation of the capillary force may cause more damage in the direction that involves more severe obstacles (cross sections noted  $E_r^i$ ) and drains less liquid. Indeed, the main drawback of the VOF simulation is amplifying the numerical interface diffusion. Figure 5.18a displays the large diffusion of the interface between water and air by using Compressive Interface Capturing Scheme for Arbitrary Meshes (CICAM). The latter scheme revealed a better choice comparing to Geometric Reconstruction Scheme (GRS) and High Resolution Interface Capturing (HRIC). To reduce diffusion at the interface of water/air local mesh refinement can be used which adds to total computation time by generation mesh for each specified timestep.

The color gradient Lattice Boltzmann Method (LBM) used in [104] provides an alternative to model interfaces dynamics. The interface diffusion is drastically reduced by LBM simulation compared to VOF for similar mesh refinement (Figure 5.18). Using similar inlet condition, the LBM simulation mimics the above described fast/slow alternating steps without definitively pinning the right front: the latter stops at fins entrance but continues its progression after some time. Moreover, the spread is still asymmetric: the water fills up four cells in the positive direction while in the negative direction only two cells are filled.

The steps of the front progression in the negative direction (Figure 5.19) are retrieved in

the LBM simulation. Even if the front is pinned at the sharp corner  $E_r^i$ , a small amount of water in the tip of the fin is present. The volume in this region grows and progressively fills the volume of fins. Then, the water continues to the next channel. Indeed, it is not a depinning but the water bypasses the  $E_r^i$  edges. The LBM simulation suggests a thin film developing on the surface of the structure and opening a path to the fin. According to [105], it is possibly an artifact of the LBM simulation due to instability at the interface between the liquid and gas phases.

However, the similarity with the experiment leads us to infer that such thin liquid films actually exist. An explanation of these thin films could be the presence of surface irregularities at microscale made by SLM manufacturing (Figure 5.3). The interstices between defects act as capillaries into which water may infiltrate and overpass the corner  $E_r^i$ . Therefore, the defects decrease the asymmetry of the water spreading.

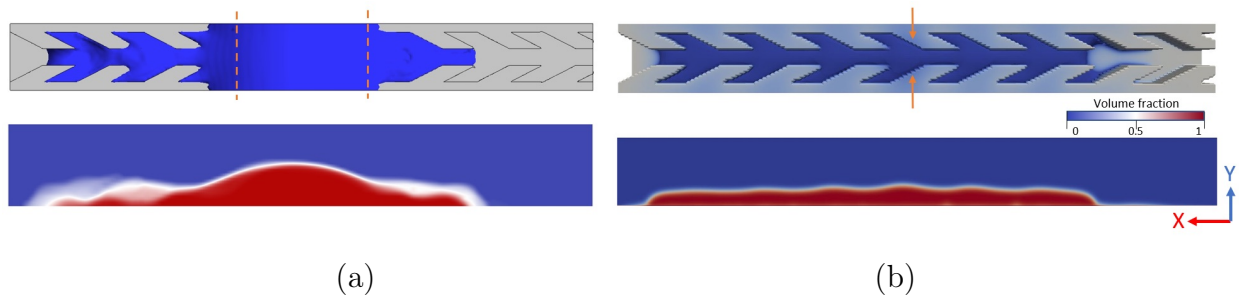


Figure 5.18: (a) Diffusion at the water/air interface in VOF simulation with compressive scheme. Parameters are as in Figure 5.10. (b) LBM simulation performs clear phase separation without excess diffusion at the interface with an equal number of cell elements. Parameters are as in Figure 5.17.

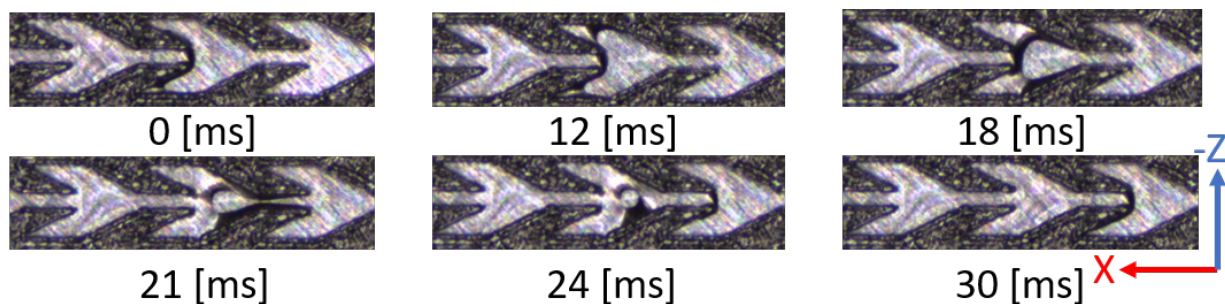


Figure 5.19: Evolution of water transport in channel type  $B$  in the negative direction. Experimental conditions are the same as in Figure 5.7. In the first snapshot ( $t = 0ms$ ) the front is blocked at the  $E_r^i$  edge. At  $t = 12ms$ , the front is still pinned but a small amount of water can be observed in the tip of the fin. The fin volume is progressively filled up till  $t = 24ms$ . At  $t = 30ms$  the water continues into the next cell.

## 5.6 Conclusion

Motivated by the problem of water drainage in the channels of the BPP, our study demonstrated the feasibility of the directional spreading of a water drop on a structured steel substrate. The fin geometry of the micro-channels was based on literature, in particular [91]. However, we employed a conductive substrate in contrast to the non-conductive PDMS polymer of [91] and to organic substrates [75], [77], [78], [80], [96]. Because of the low wettability of water on metal, there was no evidence that the devices in literature could apply in the current framework. Moreover, the manufacturing of channels with complex small-scale geometry was a challenging problem. To our knowledge, it is the first time that this type of structure has been manufactured additively with a resolution down to about  $50\mu m$ . Experiments using three different pattern sizes provide a net directional wicking. Its efficiency is correlated to the structure scale and this highlights the importance of making small structures.

For an in-depth understanding of the mechanisms involved in the liquid wicking we used a three-dimensional numerical simulation of multiphasic Navier-Stokes equations taking into account free surface, contact angle and inertia. This approach contrasts with the quasi-static description in the literature [75], [91]–[93]. We used two complementary methods: Volume of Fluids (VOF) and Lattice Boltzmann Method (LBM) to capture the complex dynamics. The VOF and LBM simulation retrieved the jerky dynamics of the wicking in the desired direction. The jerky dynamics brings into play inertia during burst phases. The fluid inertia has an influence on the onset of depinning and has therefore to be taken into account in the design of the channel shapes. This fact is reminiscent of the imbibition in porous media for which inertial forces may affect fluid front displacement dynamics as revealed by [106].

Numerical simulation provides a limit angle around  $70^\circ$  beyond which the liquid will no longer spread through the micro-channels, whereas the optimal contact angle of the asymmetric spreading is about  $30^\circ$ . This value is significantly below metal/water values which are typically superior to  $50^\circ$ . Consequently, the parameter range for designing efficient microchannels is narrow, pointing out the key role of numerical simulation in the design process.

LBM simulation tracks the gas/liquid interface better than VOF. Nevertheless, the BGK code that we used can be unstable at realistic Reynolds numbers. Other classes of LBM deserve being tried in the future, as proposed in [107], [108] for instance. Taking into account the surface defects in the simulation is a crucial outlook since our study showed that defects impact the directional wicking.

Finally, a path for improving the efficiency of the directional wicking is the surface treatment, e.g. [109], in order to achieve a lower contact angle between steel and water closer to the optimal one.

# Chapter 6

## Conclusion

The author have investigated the fluid flows that carry reactants and products during the operation of a PEMFC. We concentrated our attention on the BPPs with parallel flow field in cathode and anode. Moreover, these channels have a common interface with a porous GDL if the latter exists. If not, they have a common interface with a catalyst layer. Our approach combines numerical simulation and experiments to understand and improve the flow field. Moreover, it successively adopts two complementary viewpoints. The first one is a global approach of fuel cell operation in steady regime assuming purely gaseous flows. The second one separately studies the evolution of two-phase flow that mostly occur in cathode side.

The global description of fuel cell operation in steady regime accounts for an ensemble of physico-chemical phenomena that occur in the diverse fuel cell compartments. They all are coupled together and among them we have fluid flows carrying reactants and water, and the delivered electric current. We solved such complex system at the price of necessary simplifying assumption. Among several possible choices, we followed the principles at the basis of a numerical method that assumes single phase gaseous flows in fuel cell channels. This approach was found to agree with measurements of the electric current delivered by actual fuel cell. In agreement with the experimental validation, we still used the steady gaseous flow simulation to search for innovative channel designs appropriate to anode side. Indeed, the literature suggests that uniform the maximal velocities of the diverse channels improves fuel cell yield. The author combined the gaseous flow simulation with an algorithm that modifies channel widths so as to minimize the variations of the maximal velocity. However, the limiting factor here was the LBM code used. Better results are achievable using a three dimensional LBM simulation capable of parallel processing and multiple relaxation time step (MRT) with the same principle used in the algorithm proposed in this work for geometry optimization.

Two phase flows can interrupt electric production in fuel cells, and they are mostly caused by superfluous liquid water produced at cathode side. Hence, innovative fluid domains that help liquid water to flow out of fuel cell may help us preventing channel flooding risk. In view of exploring new designs, we have set up a LBM gradient color code for two phase

flows. We validated it against measurements and visualizations recorded in a T-junction, a simple device often used in microfluidics, not only in fuel cells. Experiment and simulation observed the scattering of a non-wetting fluid in a wetting one, both being not miscible. Though stability requirements on LBM parameters did not allow us comparing exactly the same flow conditions, the two approaches revealed very similar trends on the different shapes (droplets or films for instance) of the interface between these fluids over similar sequences of flow regimes. The thus validated LBM code also allowed us to simulate water drop spreading on structures exhibiting a set of parallel channels of non-uniform width forming a periodic pattern resembling fins (or arrow heads). Most predictions of the VOF model were corroborated by an alternative simulation using LBM. Experimental results reported in the literature had evidenced drops spreading in a privileged direction on fin shaped structures made of resin. We described a similar experiment performed on structures showing similar geometry, but made out of materials more adapted to fuel cell requirements. Our experiments returned videos of water drop wetting fin shaped patterns, confirming the same privileged direction for water/air interface motion. Simulations retrieve the privileged direction, and in addition the slip-stick dynamics shown by the videos, with almost quiescent steps intermixed with very rapid interface displacement. However, the simulation documents the interface dynamics details at much smaller scale (in time and space). It emphasizes the role of the capillary forces without neglecting inertia.

The author dealt with multiple approaches such as: numerical methods, and AM to create new enhanced product. Each method either numerical or experimental presented limits which the author was not fully aware of them previously. This work presents the capability and limits of various techniques in both numerical and experimental view. All of the limits have the potential to improve. From the numerical perspective, higher computational capacity and parametric study can help to optimize the geometric parameters. Especially, it was mentioned that the LBM code was used here not capable of handling large simulation domains. Moreover, LBM has some disadvantages which limits the stability and accuracy compared to experiment. Improving the accuracy of the LBM model such as decreasing the spurious currents is the task which must be further studied. In specific cases interpreting and calibrating the LBM simulation with experiment became very challenging. When the boundary conditions are not exactly measurable or the problem does not have a analytical solution, determining the boundary conditions for the dimensionless values in LBM become difficult. The author confronted this issue in slip-stick water transport in micro structures. When the problem is unsteady calculating the non-dimensional numbers and interpreting them for comparison with experiment in small scales becomes challenging. Moreover, in LBM initiating the flow requires changing the local densities which influences the conservation of mass. The author did explain these issues of LBM in the application of T-junction. Here there is a potential of implementing boundary conditions which can conserve the mass in the system for both phases while maintaining the stability in the simulation. Here the author introduced a structure which is capable of transporting the water inside the parallel channels directional and passively. A question which needs to be studied further to answer is which direction should the fin typed pattern be placed (counter or parallel flow) in order to increase FC performance. Each of this positioning can have specific advantages and disadvantages which should be understood. Moreover, which contact angle can improve the

performance of the FC while maintaining the manufacturability of the structures. Finally, would it be possible to manufacture these patterns on the surface using another process which is more cost efficient?

Answering the above questions needs more resources and time to study than this PhD but they can improve our understanding of the fuel cells and applying innovative solutions to well-known problems for optimization and development of new PEMFCs.

# Bibliography

- [1] Y. Manoharan, S. E. Hosseini, B. Butler, H. Alzahrani, B. T. F. Senior, T. Ashuri, and J. Krohn, “Hydrogen fuel cell vehicles: Current status and future prospect,” *Applied Sciences*, vol. 9, no. 11, p. 2296, Jun. 2019. DOI: 10.3390/app9112296.
- [2] “Hydrogen and fuel cells: Emerging technologies and applications,” *Choice Reviews Online*, vol. 43, no. 06, pp. 173–204, 401, 301, Feb. 2006. DOI: 10.5860/choice.43-3411.
- [3] N. US Department of Commerce, *ESRL Global Monitoring Division - Global Greenhouse Gas Reference Network*, EN-US.
- [4] C. P. Morice, J. J. Kennedy, N. A. Rayner, and P. D. Jones, “Quantifying uncertainties in global and regional temperature change using an ensemble of observational estimates: The HadCRUT4 data set,” *Journal of Geophysical Research: Atmospheres*, vol. 117, no. D8, n/a–n/a, Apr. 2012. DOI: 10.1029/2011jd017187.
- [5] F. Barbir, “Future of fuel cells and hydrogen,” in *PEM Fuel Cells*, Elsevier, 2013, pp. 93, 25, 13, 9. DOI: 10.1016/b978-0-12-387710-9.00012-6.
- [6] P. Lin, P. Zhou, and C. Wu, “A high efficient assembly technique for large PEMFC stacks,” *Journal of Power Sources*, vol. 194, no. 1, pp. 381–390, Oct. 2009. DOI: 10.1016/j.jpowsour.2009.04.068.
- [7] H. Wang, H. Li, and X.-Z. Yuan, Eds., *PEM Fuel Cell Failure Mode Analysis*. CRC Press, Aug. 2011, pp. 299, 314, 317. DOI: 10.1201/b11112.
- [8] C. Spiegel, “Modeling fuel cell stacks,” in *PEM Fuel Cell Modeling and Simulation Using Matlab*, Elsevier, 2008, pp. 73, 168. DOI: 10.1016/b978-012374259-9.50013-6.
- [9] M. Murthy, *Proton conducting membrane fuel cells IV*. Electrochemical Society, 2006, p. 24.
- [10] B. James, *Mass Production Cost Estimation of Direct H<sub>2</sub> PEM Fuel Cell Systems for Transportation Applications: 2016 Update*. Sep. 1, 2016, pp. 53, 54.
- [11] X. LI and I. SABIR, “Review of bipolar plates in PEM fuel cells: Flow-field designs,” *International Journal of Hydrogen Energy*, vol. 30, no. 4, pp. 359–371, Mar. 2005. DOI: 10.1016/j.ijhydene.2004.09.019.
- [12] J. Wang and H. Wang, “Flow-field designs of bipolar plates in PEM fuel cells: Theory and applications,” *Fuel Cells*, vol. 12, no. 6, pp. 989–1003, Nov. 2012. DOI: 10.1002/fuce.201200074.

- [13] A. Iranzo, C. Arredondo, A. Kannan, and F. Rosa, “Biomimetic flow fields for proton exchange membrane fuel cells: A review of design trends,” *Energy*, vol. 190, p. 116435, Jan. 2020. DOI: 10.1016/j.energy.2019.116435.
- [14] Y. B. Salah, Y. Tabe, and T. Chikahisa, “Gas channel optimisation for PEM fuel cell using the lattice boltzmann method,” *Energy Procedia*, vol. 28, pp. 125–133, 2012. DOI: 10.1016/j.egypro.2012.08.046.
- [15] N. Guo, M. C. Leu, and U. O. Koylu, “Optimization of parallel and serpentine configurations for polymer electrolyte membrane fuel cells,” *Fuel Cells*, vol. 14, no. 6, pp. 876–885, Oct. 2014. DOI: 10.1002/fuce.201400127.
- [16] W. Reitz, “Handbook of fuel cells: Fundamentals, technology, and applications, (volume 2) w. vielstich, a. lamm, and h. a. gasteiger (editors),” *Materials and Manufacturing Processes*, vol. 22, no. 6, pp. 789–789, Jun. 2007. DOI: 10.1080/10426910701416336.
- [17] N. Ahmadi, S. Rezazadeh, A. Dadvand, and I. Mirzaee, “Study of the effect of gas channels geometry on the performance of polymer electrolyte membrane fuel cell,” *Periodica Polytechnica Chemical Engineering*, 2017. DOI: 10.3311/ppch.9369.
- [18] Z. Lu, C. Rath, G. Zhang, and S. G. Kandlikar, “Water management studies in PEM fuel cells, part IV: Effects of channel surface wettability, geometry and orientation on the two-phase flow in parallel gas channels,” *International Journal of Hydrogen Energy*, vol. 36, no. 16, pp. 9864–9875, Aug. 2011. DOI: 10.1016/j.ijhydene.2011.04.226.
- [19] J. Owejan, T. Trabold, J. Gagliardo, D. Jacobson, R. Carter, D. Hussey, and M. Arif, “Voltage instability in a simulated fuel cell stack correlated to cathode water accumulation,” *Journal of Power Sources*, vol. 171, no. 2, pp. 626–633, Sep. 2007. DOI: 10.1016/j.jpowsour.2007.06.174.
- [20] M. Hasheminasab, M. Kermani, S. Nourazar, and M. Khodsiani, “A novel experimental based statistical study for water management in proton exchange membrane fuel cells,” *Applied Energy*, vol. 264, p. 114713, 2020. DOI: <https://doi.org/10.1016/j.apenergy.2020.114713>.
- [21] W. He, G. Lin, and T. V. Nguyen, “Diagnostic tool to detect electrode flooding in proton-exchange-membrane fuel cells,” *AIChE Journal*, vol. 49, no. 12, pp. 3221–3228, Dec. 2003. DOI: 10.1002/aic.690491221.
- [22] J. Roth Dipl. Ing. FH, “Water transport in gas diffusion media for pem fuel cells: Experimental and numerical investigation,” en, PhD thesis, Oct. 2010, p. 15.
- [23] M. M. Mench, Ed., *Fuel Cell Engines*. John Wiley & Sons, Inc., Jan. 2008, pp. 121, 122. DOI: 10.1002/9780470209769.
- [24] R. P. O’Hayre, “Fuel cells for electrochemical energy conversion,” *EPJ Web of Conferences*, vol. 148, p. 00013, 2017. DOI: 10.1051/epjconf/201714800013.
- [25] J.-M. L. Canut, R. M. Abouatallah, and D. A. Harrington, “Detection of membrane drying, fuel cell flooding, and anode catalyst poisoning on PEMFC stacks by electrochemical impedance spectroscopy,” *Journal of The Electrochemical Society*, vol. 153, no. 5, A857, 2006. DOI: 10.1149/1.2179200.

- [26] E. E. Feistauer, J. F. Santos, and S. T. Amancio-Filho, “A review on direct assembly of through-the-thickness reinforced metal–polymer composite hybrid structures,” *Polymer Engineering & Science*, vol. 59, no. 4, pp. 661–674, Dec. 2018. DOI: 10.1002/pen.25022.
- [27] J. E. Mueller, D. Fantauzzi, and T. Jacob, “Multiscale modeling of electrochemical systems,” in *Electrocatalysis*. John Wiley Sons, Ltd, 2014, ch. 1, pp. 1–74, ISBN: 9783527680436. DOI: 10.1002/9783527680436.ch1. eprint: <https://onlinelibrary.wiley.com/doi/pdf/10.1002/9783527680436.ch1>.
- [28] R. B. Ferreira, D. Falcão, V. Oliveira, and A. Pinto, “1d + 3d two-phase flow numerical model of a proton exchange membrane fuel cell,” *Applied Energy*, vol. 203, pp. 474–495, Oct. 2017. DOI: 10.1016/j.apenergy.2017.06.048.
- [29] S. Skoda, E. Robalinho, A. L. R. Paulino, E. F. Cunha, and M. Linardi, “Modeling of liquid water distribution at cathode gas flow channels in proton exchange membrane fuel cell - PEMFC,” p. 6,
- [30] M. A. Rahman, J. M. Mora, and P. A. Chuang, “A computational study of flow sensitivity of a PEM fuel cell with multi-parallel flow channels,” p. 7, 2017.
- [31] A. L. R. Paulino, E. Robalinho, E. F. Cunha, R. R. Passos, and E. I. Santiago, “Current distribution on PEM fuel cells with different flow channel patterns,” p. 5,
- [32] P. T. Nguyen, T. Berning, and N. Djilali, “Computational model of a PEM fuel cell with serpentine gas flow channels,” *Journal of Power Sources*, vol. 130, no. 1-2, pp. 149–157, May 2004. DOI: 10.1016/j.jpowsour.2003.12.027.
- [33] R. Krishna and J. A. Wesselingh, “The maxwell-stefan approach to mass transfer,” *Chemical Engineering Science*, vol. 52, no. 6, pp. 861–911, Mar. 1, 1997, ISSN: 0009-2509. DOI: 10.1016/S0009-2509(96)00458-7.
- [34] S. Leclaire, M. Reggio, and J.-Y. Trépanier, “Progress and investigation on lattice boltzmann modeling of multiple immiscible fluids or components with variable density and viscosity ratios,” *Journal of Computational Physics*, vol. 246, pp. 318–342, Aug. 2013. DOI: 10.1016/j.jcp.2013.03.039.
- [35] —, “Numerical evaluation of two recoloring operators for an immiscible two-phase flow lattice boltzmann model,” *Applied Mathematical Modelling*, vol. 36, no. 5, pp. 2237–2252, May 2012. DOI: 10.1016/j.apm.2011.08.027.
- [36] —, “Isotropic color gradient for simulating very high-density ratios with a two-phase flow lattice boltzmann model,” *Computers & Fluids*, vol. 48, no. 1, pp. 98–112, Sep. 2011. DOI: 10.1016/j.compfluid.2011.04.001.
- [37] D. H. Rothman and J. M. Keller, “Immiscible cellular-automaton fluids,” *Journal of Statistical Physics*, vol. 52, no. 3-4, pp. 1119–1127, Aug. 1988. DOI: 10.1007/bf01019743.
- [38] H. Huang, M. C. Sukop, and X.-Y. Lu, *Multiphase Lattice Boltzmann Methods: Theory and Application*. John Wiley & Sons, Ltd, Jul. 2015, p. 7. DOI: 10.1002/9781118971451.

- [39] T. Danner, S. Eswara, V. P. Schulz, and A. Latz, “Characterization of gas diffusion electrodes for metal-air batteries,” *Journal of Power Sources*, vol. 324, pp. 646–656, Aug. 2016. DOI: 10.1016/j.jpowsour.2016.05.108.
- [40] T. Reis and T. N. Phillips, “Lattice boltzmann model for simulating immiscible two-phase flows,” *Journal of Physics A: Mathematical and Theoretical*, vol. 40, no. 14, pp. 4033–4053, Mar. 2007. DOI: 10.1088/1751-8113/40/14/018.
- [41] M. Latva-Kokko and D. H. Rothman, “Diffusion properties of gradient-based lattice boltzmann models of immiscible fluids,” *Physical Review E*, vol. 71, no. 5, p. 98, May 2005. DOI: 10.1103/physreve.71.056702.
- [42] M. J. Blunt, *Multiphase Flow in Permeable Media*. Cambridge University Press, 2017, p. 16. DOI: 10.1017/9781316145098.
- [43] J. Tölke, “Gitter-boltzmann-verfahren zur simulation von zweiphasenströmungen,” PhD thesis, TU München, 2001.
- [44] S. Bashir, J. M. Rees, and W. B. Zimmerman, “Simulations of microfluidic droplet formation using the two-phase level set method,” *Chemical Engineering Science*, vol. 66, no. 20, pp. 4733–4741, Oct. 2011. DOI: 10.1016/j.ces.2011.06.034.
- [45] X.-B. Li, F.-C. Li, J.-C. Yang, H. Kinoshita, M. Oishi, and M. Oshima, “Study on the mechanism of droplet formation in t-junction microchannel,” *Chemical Engineering Science*, vol. 69, no. 1, pp. 340–351, Feb. 2012. DOI: 10.1016/j.ces.2011.10.048.
- [46] H. Song, D. L. Chen, and R. F. Ismagilov, “Reactions in droplets in microfluidic channels,” *Angewandte Chemie International Edition*, vol. 45, no. 44, pp. 7336–7356, Nov. 2006. DOI: 10.1002/anie.200601554.
- [47] Y. Yan, D. Guo, and S. Wen, “Numerical simulation of junction point pressure during droplet formation in a microfluidic t-junction,” *Chemical Engineering Science*, vol. 84, pp. 591–601, Dec. 2012. DOI: 10.1016/j.ces.2012.08.055.
- [48] F. Kaske, S. Dick, S. A. Pajoochi, and D. W. Agar, “The influence of operating conditions on the mass transfer performance of a micro capillary contactor with liquid–liquid slug flow,” *Chemical Engineering and Processing: Process Intensification*, vol. 108, pp. 10–16, Oct. 2016. DOI: 10.1016/j.cep.2016.06.010.
- [49] M. O’Brien, D. A. Cooper, and J. Dolan, “Continuous flow iodination using an automated computer-vision controlled liquid-liquid extraction system,” *Tetrahedron Letters*, vol. 58, no. 9, pp. 829–834, Mar. 2017. DOI: 10.1016/j.tetlet.2017.01.029.
- [50] M. O’Brien, P. Koos, D. L. Browne, and S. V. Ley, “A prototype continuous-flow liquid–liquid extraction system using open-source technology,” *Organic & Biomolecular Chemistry*, vol. 10, no. 35, p. 7031, 2012. DOI: 10.1039/c2ob25912e.
- [51] B. Gutmann, D. Cantillo, and C. O. Kappe, “Continuous-flow technology—a tool for the safe manufacturing of active pharmaceutical ingredients,” *Angewandte Chemie International Edition*, vol. 54, no. 23, pp. 6688–6728, May 2015. DOI: 10.1002/anie.201409318.

- [52] K. Terao, Y. Nishiyama, and K. Kakiuchi, “Highly efficient asymmetric paternò–büchi reaction in a microcapillary reactor utilizing slug flow,” *Journal of Flow Chemistry*, vol. 4, no. 1, pp. 35–39, Mar. 2015. DOI: 10.1556/jfc-d-13-00035.
- [53] V. Hessel, D. Kralisch, N. Kockmann, T. Noël, and Q. Wang, “Novel process windows for enabling, accelerating, and uplifting flow chemistry,” *ChemSusChem*, vol. 6, no. 5, pp. 746–789, Apr. 2013. DOI: 10.1002/cssc.201200766.
- [54] C. E. Colosqui, M. J. Cheah, I. G. Kevrekidis, and J. B. Benziger, “Droplet and slug formation in polymer electrolyte membrane fuel cell flow channels: The role of interfacial forces,” *Journal of Power Sources*, vol. 196, no. 23, pp. 10 057–10 068, Dec. 2011. DOI: 10.1016/j.jpowsour.2011.08.084.
- [55] S. Borukhova, T. Noël, and V. Hessel, “Hydrogen chloride gas in solvent-free continuous conversion of alcohols to chlorides in microflow,” *Organic Process Research & Development*, vol. 20, no. 2, pp. 568–573, Feb. 2016. DOI: 10.1021/acs.oprd.6b00014.
- [56] T. Baumeister, H. Kitzler, K. Obermaier, S. Zikeli, and T. Röder, “Two-phase flow oxidation of valeraldehyde with o<sub>2</sub> in a microstructured reactor,” *Organic Process Research & Development*, vol. 19, no. 11, pp. 1576–1579, Sep. 2015. DOI: 10.1021/acs.oprd.5b00173.
- [57] H. P. L. Gemoets, Y. Su, M. Shang, V. Hessel, R. Luque, and T. Noël, “Liquid phase oxidation chemistry in continuous-flow microreactors,” *Chemical Society Reviews*, vol. 45, no. 1, pp. 83–117, 2016. DOI: 10.1039/c5cs00447k.
- [58] M. Mendorf, H. Nachtrodt, A. Mescher, A. Ghaini, and D. W. Agar, “Design and control techniques for the numbering-up of capillary microreactors with uniform multiphase flow distribution,” *Industrial & Engineering Chemistry Research*, vol. 49, no. 21, pp. 10 908–10 916, Nov. 2010. DOI: 10.1021/ie100473d.
- [59] H. Gu, M. H. G. Duits, and F. Mugele, “Droplets formation and merging in two-phase flow microfluidics,” *International Journal of Molecular Sciences*, vol. 12, no. 4, pp. 2572–2597, Apr. 2011. DOI: 10.3390/ijms12042572.
- [60] T. Glawdel, C. Elbuken, and C. L. Ren, “Droplet formation in microfluidic t-junction generators operating in the transitional regime. i. experimental observations,” *Physical Review E*, vol. 85, no. 1, Jan. 2012. DOI: 10.1103/physreve.85.016322.
- [61] P. Garstecki, M. J. Fuerstman, H. A. Stone, and G. M. Whitesides, “Formation of droplets and bubbles in a microfluidic t-junction—scaling and mechanism of breakup,” *Lab on a Chip*, vol. 6, no. 3, p. 437, 2006. DOI: 10.1039/b510841a.
- [62] L. Shui, A. van den Berg, and J. C. T. Eijkel, “Capillary instability, squeezing, and shearing in head-on microfluidic devices,” *Journal of Applied Physics*, vol. 106, no. 12, p. 124 305, Dec. 2009. DOI: 10.1063/1.3268364.
- [63] Y. Shi, G. Tang, and H. Xia, “Lattice boltzmann simulation of droplet formation in t-junction and flow focusing devices,” *Computers & Fluids*, vol. 90, pp. 155–163, Feb. 2014. DOI: 10.1016/j.compfluid.2013.11.025.
- [64] H. Liu and Y. Zhang, “Droplet formation in a t-shaped microfluidic junction,” *Journal of Applied Physics*, vol. 106, no. 3, p. 034 906, Aug. 2009. DOI: 10.1063/1.3187831.

- [65] M. D. MENECH, P. GARSTECKI, F. JOUSSE, and H. A. STONE, “Transition from squeezing to dripping in a microfluidic t-shaped junction,” *Journal of Fluid Mechanics*, vol. 595, pp. 141–161, Jan. 2008. DOI: 10.1017/s002211200700910x.
- [66] A. Gupta, S. M. S. Murshed, and R. Kumar, “Droplet formation and stability of flows in a microfluidic t-junction,” *Applied Physics Letters*, vol. 94, no. 16, p. 164107, Apr. 2009. DOI: 10.1063/1.3116089.
- [67] S. van der Graaf, T. Nisisako, C. G. P. H. Schroën, R. G. M. van der Sman, and R. M. Boom, “Lattice boltzmann simulations of droplet formation in a t-shaped microchannel,” *Langmuir*, vol. 22, no. 9, pp. 4144–4152, Apr. 2006. DOI: 10.1021/la052682f.
- [68] M. C. Sukop and D. T. Thorne, *Lattice Boltzmann Modeling*. Springer Berlin Heidelberg, 2006. DOI: 10.1007/978-3-540-27982-2.
- [69] T. Krüger, *Computer Simulation Study of Collective Phenomena in Dense Suspensions of Red Blood Cells under Shear*. ViewegTeubner Verlag, 2012. DOI: 10.1007/978-3-8348-2376-2.
- [70] T. Thorsen, R. W. Roberts, F. H. Arnold, and S. R. Quake, “Dynamic pattern formation in a vesicle-generating microfluidic device,” *Physical Review Letters*, vol. 86, no. 18, pp. 4163–4166, Apr. 2001. DOI: 10.1103/physrevlett.86.4163.
- [71] L. Shui, “Two-phase flow in micro and nanofluidic devices,” PhD thesis, 2009. DOI: 10.3990/1.9789036528368.
- [72] A. K. Pabby, S. S. H. Rizvi, and A. M. S. Requena, *Handbook of Membrane Separations: Chemical, Pharmaceutical, Food, and Biotechnological Applications, Second Edition*, en. CRC Press, Apr. 2015, p. 570, ISBN: 978-1-4665-5558-7.
- [73] D. R. Ballerini, X. Li, and W. Shen, “An inexpensive thread-based system for simple and rapid blood grouping,” *Analytical and Bioanalytical Chemistry*, vol. 399, no. 5, pp. 1869–1875, Jan. 2011. DOI: 10.1007/s00216-010-4588-5.
- [74] A. W. Martinez, S. T. Phillips, Z. Nie, C.-M. Cheng, E. Carrilho, B. J. Wiley, and G. M. Whitesides, “Programmable diagnostic devices made from paper and tape,” *Lab on a Chip*, vol. 10, no. 19, p. 2499, 2010. DOI: 10.1039/c0lc00021c.
- [75] A. R. Parker and C. R. Lawrence, “Water capture by a desert beetle,” *Nature*, vol. 414, no. 6859, pp. 33–34, Nov. 2001. DOI: 10.1038/35102108.
- [76] J. Guadarrama-Cetina, A. Mongruel, M. .-G. Medici, E. Baquero, A. R. Parker, I. Milimouk-Melnychuk, W. González-Viñas, and D. Beysens, “Dew condensation on desert beetle skin,” *The European Physical Journal E*, vol. 37, no. 11, Nov. 2014. DOI: 10.1140/epje/i2014-14109-y.
- [77] M. Gürsoy, M. Harris, A. Carletto, A. Yaprak, M. Karaman, and J. Badyal, “Bioinspired asymmetric-anisotropic (directional) fog harvesting based on the arid climate plant *eremopyrum orientale*,” *Colloids and Surfaces A: Physicochemical and Engineering Aspects*, vol. 529, pp. 959–965, Sep. 2017. DOI: 10.1016/j.colsurfa.2017.06.065.
- [78] M. Aliabadi, A. Zarkesh, and M. Mahdavinejad, “Bioware fog collectors: The texas horned lizard as a model for a biomimetic fog-harvesting,” *Materials Research Express*, vol. 5, no. 11, p. 115502, Sep. 2018. DOI: 10.1088/2053-1591/aadab4.

- [79] K. Muto, S. Ito, and D. Ishii, “Liquid transport in bio-inspired capillary-driven open-air channels,” *MRS Advances*, vol. 2, no. 19-20, pp. 1111–1116, 2017. DOI: 10.1557/adv.2017.77.
- [80] P. S. Brown and B. Bhushan, “Bioinspired materials for water supply and management: Water collection, water purification and separation of water from oil,” *Philosophical Transactions of the Royal Society A: Mathematical, Physical and Engineering Sciences*, vol. 374, no. 2073, p. 20160135, Aug. 2016. DOI: 10.1098/rsta.2016.0135.
- [81] X. Yao, Y. Song, and L. Jiang, “Applications of bio-inspired special wettable surfaces,” *Advanced Materials*, vol. 23, no. 6, pp. 719–734, Dec. 2010. DOI: 10.1002/adma.201002689.
- [82] J. Li and Z. Guo, “Spontaneous directional transportations of water droplets on surfaces driven by gradient structures,” *Nanoscale*, vol. 10, no. 29, pp. 13814–13831, 2018. DOI: 10.1039/c8nr04354j.
- [83] S. Mettu and M. K. Chaudhury, “Motion of drops on a surface induced by thermal gradient and vibration,” *Langmuir*, vol. 24, no. 19, pp. 10833–10837, Oct. 2008. DOI: 10.1021/la801380s.
- [84] Q. Liu and B. Xu, “A unified mechanics model of wettability gradient-driven motion of water droplet on solid surfaces,” *Extreme Mechanics Letters*, vol. 9, pp. 304–309, Dec. 2016. DOI: 10.1016/j.eml.2016.09.004.
- [85] J.-J. Huang, H. Huang, and X. Wang, “Numerical study of drop motion on a surface with stepwise wettability gradient and contact angle hysteresis,” *Physics of Fluids*, vol. 26, no. 6, p. 062101, Jun. 2014. DOI: 10.1063/1.4880656.
- [86] I. U. Chowdhury, P. S. Mahapatra, and A. K. Sen, “Self-driven droplet transport: Effect of wettability gradient and confinement,” *Physics of Fluids*, vol. 31, no. 4, p. 042111, Apr. 2019. DOI: 10.1063/1.5088562.
- [87] M. Ahmadlouydarab and J. Feng, “Motion and coalescence of sessile drops driven by substrate wetting gradient and external flow,” *Journal of Fluid Mechanics*, vol. 746, pp. 214–235, Apr. 2014. DOI: 10.1017/jfm.2014.133.
- [88] N. Moumen, R. S. Subramanian, and J. B. McLaughlin, “Experiments on the motion of drops on a horizontal solid surface due to a wettability gradient,” *Langmuir*, vol. 22, no. 6, pp. 2682–2690, Mar. 2006. DOI: 10.1021/la053060x.
- [89] M. K. Chaudhury, A. Chakrabarti, and S. Daniel, “Generation of motion of drops with interfacial contact,” *Langmuir*, vol. 31, no. 34, pp. 9266–9281, Feb. 2015. DOI: 10.1021/la504925u.
- [90] M. K. Chaudhury and G. M. Whitesides, “How to make water run uphill,” *Science*, vol. 256, no. 5063, pp. 1539–1541, Jun. 1992. DOI: 10.1126/science.256.5063.1539.
- [91] J. Feng and J. P. Rothstein, “One-way wicking in open micro-channels controlled by channel topography,” *Journal of Colloid and Interface Science*, vol. 404, pp. 169–178, Aug. 2013. DOI: 10.1016/j.jcis.2013.02.052.

- [92] G. Buchberger, F. Hischen, P. Comanns, R. Baumgartner, A. Kogler, A. Buchsbaum, S. Bauer, and W. Baumgartner, “Bio-inspired microfluidic devices for passive, directional liquid transport: Model-based adaption for different materials,” *Procedia Engineering*, vol. 120, pp. 106–111, 2015. DOI: 10.1016/j.proeng.2015.08.576.
- [93] K. Muto and D. Ishii, “Effects of anisotropic liquid spreading on liquid transport in arrow-like micropillar arrays,” *Colloids and Surfaces A: Physicochemical and Engineering Aspects*, vol. 544, pp. 86–90, May 2018. DOI: 10.1016/j.colsurfa.2018.02.023.
- [94] D. Modroukas, V. Modi, and L. G. Fr echette, “Micromachined silicon structures for free-convection PEM fuel cells,” *Journal of Micromechanics and Microengineering*, vol. 15, no. 9, S193–S201, Aug. 2005. DOI: 10.1088/0960-1317/15/9/s04.
- [95] O. Bliznyuk, H. P. Jansen, E. S. Kooij, H. J. W. Zandvliet, and B. Poelsema, “Smart design of stripe-patterned gradient surfaces to control droplet motion,” *Langmuir*, vol. 27, no. 17, pp. 11 238–11 245, Sep. 2011. DOI: 10.1021/la201671w.
- [96] P. Comanns, G. Buchberger, A. Buchsbaum, R. Baumgartner, A. Kogler, S. Bauer, and W. Baumgartner, “Directional, passive liquid transport: The texas horned lizard as a model for a biomimetic ‘liquid diode’,” *Journal of The Royal Society Interface*, vol. 12, no. 109, p. 20 150 415, Aug. 2015. DOI: 10.1098/rsif.2015.0415.
- [97] C. Hirt and B. Nichols, “Volume of fluid (vof) method for the dynamics of free boundaries,” *Journal of Computational Physics*, vol. 39, pp. 201–225, 1981.
- [98] J. Brackbill, D. Kothe, and C. Zemach, “A continuum method for modeling surface tension,” *Journal of Computational Physics*, vol. 100, no. 2, pp. 335–354, Jun. 1992. DOI: 10.1016/0021-9991(92)90240-y.
- [99] I. Malgarinos, N. Nikolopoulos, M. Marengo, C. Antonini, and M. Gavaises, “VOF simulations of the contact angle dynamics during the drop spreading: Standard models and a new wetting force model,” *Advances in Colloid and Interface Science*, vol. 212, pp. 1–20, Oct. 2014. DOI: 10.1016/j.cis.2014.07.004.
- [100] D. Bonn, J. Eggers, J. Indekeu, J. Meunier, and E. Rolley, “Wetting and spreading,” *Reviews of Modern Physics*, vol. 81, no. 2, pp. 739–805, May 2009. DOI: 10.1103/revmodphys.81.739.
- [101] R. G. Cox, “The dynamics of the spreading of liquids on a solid surface. part 1. viscous flow,” *Journal of Fluid Mechanics*, vol. 168, no. -1, p. 169, Jul. 1986. DOI: 10.1017/s0022112086000332.
- [102] M. L. Blow and J. M. Yeomans, “Anisotropic imbibition on surfaces patterned with polygonal posts,” *Philosophical Transactions of the Royal Society A: Mathematical, Physical and Engineering Sciences*, vol. 369, no. 1945, pp. 2519–2527, Jun. 2011. DOI: 10.1098/rsta.2011.0030.
- [103] P. Beltrame, E. Knobloch, P. H anggi, and U. Thiele, “Rayleigh and depinning instabilities of forced liquid ridges on heterogeneous substrates,” *Physical Review E*, vol. 83, no. 1, Jan. 2011. DOI: 10.1103/physreve.83.016305.

- [104] V. P. Schulz, N. Abbaspour, T. Baumeister, and T. Röder, “Lattice-boltzmann simulation and experimental validation of a microfluidic t-junction for slug flow generation,” *ChemEngineering*, vol. 3, no. 2, p. 48, May 2019. DOI: 10.3390/chemengineering3020048.
- [105] K. Connington and T. Lee, “A review of spurious currents in the lattice boltzmann method for multiphase flows,” *Journal of Mechanical Science and Technology*, vol. 26, no. 12, pp. 3857–3863, Dec. 2012. DOI: 10.1007/s12206-012-1011-5.
- [106] F. Moebius and D. Or, “Inertial forces affect fluid front displacement dynamics in a pore-throat network model,” *Phys. Rev. E*, vol. 90, p. 023 019, 2 Aug. 2014. DOI: 10.1103/PhysRevE.90.023019.
- [107] P. Lallemand, L.-S. Luo, and Y. Peng, “A lattice boltzmann front-tracking method for interface dynamics with surface tension in two dimensions,” *Journal of Computational Physics*, vol. 226, pp. 1367–1484, 2007. DOI: 10.1016/j.jcp.2007.05.021.
- [108] A. Fakhari, D. Bolster, and L.-S. Luo, “A weighted multi-relaxation time lattice boltzmann method for multiphase flows and its applications to partial coalescence cascades,” *Journal of Computational Physics*, vol. 341, pp. 22–43, 2017. DOI: 10.1016/j.jcp.2017.03.062.
- [109] J.-S. Cho, K.-H. Kim, S. Han, Y.-W. Beag, and S.-K. Koh, “Hydrophilic surface formation on polymers by ion-assisted reaction,” *Progress in Organic Coatings*, vol. 48, no. 2-4, pp. 251–258, Dec. 2003. DOI: 10.1016/s0300-9440(03)00098-5.



# Nima Abbaspour

**Nationality:** Iranian/German

**Age:** 33

**Gender:** Male

✉ **Email address:** [eng.abbaspour@gmail.com](mailto:eng.abbaspour@gmail.com)

📍 **Address :** Salem (Germany)

## ABOUT ME

---

I am a mechanical engineer passionate about innovation and numerical simulation. My goal is to improve the life quality for everyone by engineering. I enjoy working on my new ideas and reading the research results of other scientists.

## WORK EXPERIENCE

---

### Innovation and Development Engineer

**J. Wagner GmbH** [ 09/01/2018 – Current ]

**City:** Markdorf

**Country:** Germany

- Modeling, simulation and optimization of paint spray system.
- Support the design and development department with CFD, FEM, CHT simulation.
- CAD design, prototyping and performing necessary tests.
- Research and development for innovation management

### University research associate

**Baden-Württemberg Cooperative State University (DHBW)** [ 07/01/2015 – 06/30/2018 ]

**City:** Mannheim

**Country:** Germany

- I have have worked actively on "Optimization of Proton Exchange Membrane (PEM) fuel cells using additive manufactured gas diffusion layer and flow channels (Central Innovation Program for SMEs)" project.
- Participated in research projects in the field of Multiphase flows simulation.
- Lecturer of computational fluid mechanic and simulation technique courses.
- Supervising the students for projects and their bachelor thesis.
- Publishing and participating in scientific conferences and seminars.

### Student Assistant

**German Aerospace Center (DLR)** [ 08/01/2012 – 07/31/2014 ]

**City:** Braunschweig

**Country:** Germany

- Aerodynamic optimization of molds for CFRP parts to improve their thermal behavior.
- Data analysis from CAD data with python scripts.
- Prepare a handbook for DLR aeroacoustic solver DISKO

## EDUCATION AND TRAINING

---

Bachelor in Mechanical Engineering

Islamic Azad University, Takestan, Iran

**Address:** Takestan (Iran)

**Field(s) of study:** Specializing in Fluid Mechanics

**Thesis :** Jarandaq site data study for wind energy development.

## LANGUAGE SKILLS

---

Mother tongue(s):

**Persian**

**German**

LISTENING: C1 READING: C1 UNDERSTANDING: C1

SPOKEN PRODUCTION: C1

SPOKEN INTERACTION: C1

**English**

LISTENING: C2 READING: C2 UNDERSTANDING: C2

SPOKEN PRODUCTION: C2

SPOKEN INTERACTION: C2

## DIGITAL SKILLS

---

CAE / CFD / FEM / Simulation / Research / Development / ANSYS Fluent / OpenFOAM / Creo Parametric / SolidWorks / COMSOL / LaTeX / MS Office / Windows / Linux / CATIA / CC++ / Java / PYTHON / Innovate

## PUBLICATIONS

---

Lattice-Boltzmann Simulation and Experimental Validation of a Microfluidic T-Junction for Slug Flow

[2019]

<https://doi.org/10.3390/chemengineering3020048>

Directional water wicking on metal surface patterned by microchannels

[2020]

under consideration in the European Physical Journal Applied Physics (EPJ AP)

## PATENTS

---

Smart control of spray system (US Patent)

[ 07/2019 ]

Gesture control of a spray system (US patent)

[ 09/2019 ]

## CONFERENCES AND SEMINARS

---

Optimization of transport in the PEM-Fuel cells using 3D micro print method.

[ New Orleans, US, 05/2018 ]

The International Society for Porous Media (InterPore)

**Lattice-Boltzmann simulation and experimental validation of different Microfluidic T-Junctions.**

[ Erlangen, DE, 07/2017 ]

26th International Conference on Discrete Simulation of Fluid Dynamics (DSFD)

**Optimization of the PEM-Fuel Cells Using 3D Micro Print Method.**

[ Bad Honnef, DE, 07/2017 ]

WE-Heraeus-Seminar

**Multiphase Simulation of Transport Processes in PEM Fuel Cells with The Lattice Boltzmann Method.**

[ Nuremberg, DE, 10/2015 ]

PhD-Seminar on PEM Fuel Cells

**Simulation of Unsteady Flow Field Around a Savonius Wind Turbine.**

[ Bremen, DE, 10/2010 ]

German Wind Energy Conference (DEWEK)

## **HONOURS AND AWARDS**

---

**Manufacturing the largest paper aircraft that can fly.**

Guinness Word Record

<https://www.guinnessworldrecords.com/world-records/largest-paper-aircraft>